

**APPLIED
COMPUTATIONAL
ELECTROMAGNETICS
SOCIETY
JOURNAL**

September 2014
Vol. 29 No. 9
ISSN 1054-4887

The ACES Journal is abstracted in INSPEC, in Engineering Index, DTIC, Science Citation Index Expanded, the Research Alert, and to Current Contents/Engineering, Computing & Technology.

The illustrations on the front cover have been obtained from the research groups at the Department of Electrical Engineering, The University of Mississippi.

THE APPLIED COMPUTATIONAL ELECTROMAGNETICS SOCIETY

<http://www.aces-society.org>

EDITOR-IN-CHIEF

Atef Elsherbeni

Colorado School of Mines, EECS Dept.
Golden, CO 80401, USA

ASSOCIATE EDITORS-IN-CHIEF

Sami Barmada

University of Pisa, EE Dept.
Pisa, Italy, 56126

Mohammed Hadi

Kuwait University, EE Dept.
Safat, Kuwait

Paolo Mezzanotte

University of Perugia
I-06125 Perugia, Italy

Yasushi Kanai

Niigata Inst. of Technology
Kashiwazaki, Japan

Alistair Duffy

De Montfort University
Leicester, UK

Antonio Musolino

University of Pisa
56126 Pisa, Italy

Ozlem Kilic

Catholic University of America
Washington DC, 20064, USA

Mohamed Bakr

McMaster University, ECE Dept.
Hamilton, ON, L8S 4K1, Canada

Marco Arjona López

La Laguna Institute of Technology
Coahuila 27266, Mexico

Fan Yang

Tsinghua University, EE Dept.
Beijing 100084, China

Abdul Arkadan

Rafik Hariri University
Chouf 2010, Lebanon

EDITORIAL ASSISTANTS

Matthew J. Inman

University of Mississippi, EE Dept.
University, MS 38677, USA

Shanell Lopez

Colorado School of Mines, EECS Dept.
Golden, CO 80401, USA

EMERITUS EDITORS-IN-CHIEF

Duncan C. Baker

EE Dept. U. of Pretoria
0002 Pretoria, South Africa

Ahmed Kishk

University of Mississippi, EE Dept.
University, MS 38677, USA

Allen Glisson

University of Mississippi, EE Dept.
University, MS 38677, USA

Robert M. Bevensee

Box 812
Alamo, CA 94507-0516, USA

David E. Stein

USAF Scientific Advisory Board
Washington, DC 20330, USA

EMERITUS ASSOCIATE EDITORS-IN-CHIEF

Mohamed Abouzahra

MIT Lincoln Laboratory
Lexington, MA, USA

Erdem Topsakal

Mississippi State University, EE Dept.
Mississippi State, MS 39762, USA

Levent Gurel

Bilkent University
Ankara, Turkey

Alexander Yakovlev

University of Mississippi, EE Dept.
University, MS 38677, USA

EMERITUS EDITORIAL ASSISTANTS

Khaled ElMaghoub

University of Mississippi, EE Dept.
University, MS 38677, USA

Christina Bonnington

University of Mississippi, EE Dept.
University, MS 38677, USA

Anne Graham

University of Mississippi, EE Dept.
University, MS 38677, USA

Mohamed Al Sharkawy

Arab Academy for Science and Technology, ECE Dept.
Alexandria, Egypt

SEPTEMBER 2014 REVIEWERS

Gulam Alsath

Rodolfo Araneo

Rezaul Azim

Mohamed Bakr

Mustafa Bilgic

Qiang Cheng

Alistar Duffy

Ali Farahbakhsh

Arkom Kaewrawang

Darko Kajfez

Slawomir Koziel

George Kyriacou

Mingyu Lu

Sohrab Majidifar

Rashid Mirzavand

Marco Mussetta

Christian Pichot

Chris Railton

Abdaloussein Rezai

Abhishek Sharma

Yury Shestopalov

Christopher Trueman

THE APPLIED COMPUTATIONAL ELECTROMAGNETICS SOCIETY
JOURNAL

Vol. 29 No. 9

September 2014

TABLE OF CONTENTS

“Electromagnetic Device Optimization: The Forking of Already Parallelized Threads on Graphics Processing Units”
S. Ratnajeevan H. Hoole, Sivamayam Sivasuthan, Victor U. Karthik,
Arunasalam Rahunanthan, Ravi S. Thyagarajan, and Paramsothy Jayakumar677

“An UWB Microstrip-Fed Slot Antenna with Enhanced Bandwidth and WLAN Band-Notched Characteristics”
Yasser Ojaroudi, Sajjad Ojaroudi, and Nasser Ojaroudi685

“A Novel Multi-Way Power Divider Design with Enhanced Spurious Suppression”
Jiuchao Li, Yuanan Liu, Shulan Li, Cuiping Yu, and Yongle Wu692

“On the Attenuation of the Perfectly Matched Layer in Electromagnetic Scattering Problems with the Spectral Element Method”
I. Mahariq, M. Kuzuoglu, and I. H. Tarman701

“A Compact 2-18 GHz Halved Vivaldi Antenna”
Ping Wang, Guangjun Wen, Yongjun Huang, and Haobin Zhang711

“Multi-Resonance Monopole Antenna with Inverted Y-Shaped Slit and Conductor-Backed Plane”
S. Ojaroudi, Y. Ojaroudi, and N. Ojaroudi720

“Analytical Estimation of Radar Cross Section of Arbitrary Compact Dipole Array”
H. L. Sneha, Hema Singh, and R. M. Jha726

“A Novel Dual-Mode Wideband Band Pass Filter”
A. Ahmadi, S. V. Makki, A. Lalbakhsh, and S. Majidifar735

“Design of a Broadband Microstrip-to-Microstrip Vertical Transition”
Ziwen Tao, Jianpeng Wang, and Yan Dou743

“CPW-Fed Fractal Monopole Antenna for UWB Communication Applications”
Y. Zehforoosh and M. Naser-Moghadasi.748

Electromagnetic Device Optimization: The Forking of Already Parallelized Threads on Graphics Processing Units

S. Ratnajeevan H. Hoole¹, Sivamayam Sivasuthan¹, Victor U. Karthik¹,
Arunasalam Rahunathan², Ravi S. Thyagarajan³, and Paramsothy Jayakumar³

¹Department of Electrical and Computer Engineering
Michigan State University, East Lansing, MI 48824, USA
srhhoole@gmail.com, sivasuth@msu.edu, uthayaku@msu.edu

²Department of Mathematics and Computer Science
Edinboro University, Edinboro, PA 16444, USA.
rahananthana@gmail.com

³U.S. Army Tank Automotive Research, Development & Engineering Center, Warren, MI 48397, USA
ravi.s.thyagarajan.civ@mail.mil, paramsothy.jayakumar.civ@mail.mil

Abstract — In light of the new capability to fork an already parallelized kernel on a GPU, this paper shows how the use of the parallelization capabilities of a PC's Graphics Processing Unit (GPU) makes the finite element design of coupled problems (such as the electroheat shape optimization problems we work with) realistic and practicable in terms of computational time.

Index Terms - Finite elements, GPU computing, inverse problems, parallelization.

I. INTRODUCTION: INVERSE PROBLEMS

In contrast to the forward problem (Fig. 1) that we normally solve, inverse problems are more realistic in device design going from the bottom to the top of that figure, in such design tasks as, say, compute the size and other descriptions of a motor that can produce so much torque. Figure 2 shows the design cycle for an inverse problem as a repeating cycle of forward problems. In the first step, the design parameter set \bar{h} is randomly selected (or estimated by a subject expert), and thereupon we generate the parameter based mesh, get the finite element solution, measure the object

value (often conveniently defined as a least square difference between design objects desired and those computed) and check whether it is minimum or not. If this is minimum, we terminate the loop; otherwise we change the design parameters and do the same procedure again.

This procedure repeats until the object value goes to its minimum. This solution process however, is computationally intensive. To address this problem, parallelization on GPU threads has been proposed [1-2]. Each finite element solution in its matrix solution part is computationally intensive [3,4] and GPU parallelization significantly reduces solution time. But in genetic algorithm optimization [5,6], several copies of the matrix are held on the GPU and the corresponding solutions attempted. This runs into the memory limits of GPUs, newly at 12 GB from around the time of the initial submission of this paper [7].

In this paper therefore, we look more deeply at using the GPU to do the optimization in parallel. We examine memory limits and use the recently revived element-by-element finite element method for speedy finite element matrix solutions on the GPU [8,9] to address memory concerns and exploit such matrix solution speedups to obtain a speedup

UNCLASSIFIED: Distribution Statement A. Approved for public release.

of 28 for genetic algorithm based coupled field optimization. Where we are allowed to fork only one computational kernel and not allowed to fork that kernel into further parallelizable processes on a GPU, we delve into important considerations for choosing which one kernel to fork.

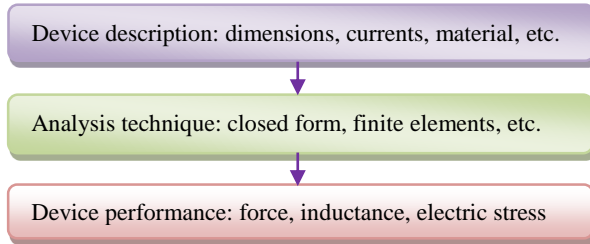


Fig. 1. The typical forward problem.

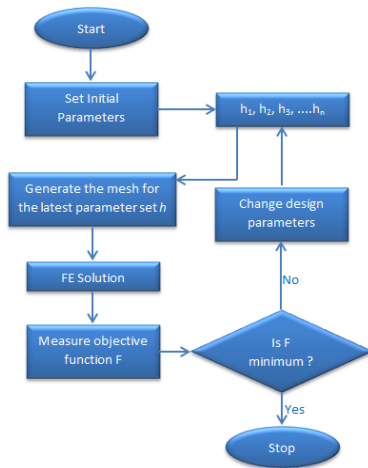


Fig. 2. The design cycle for inverse problem.

II. GPU COMPUTATION: MEMORY STUDY

In the CUDA programming model (see Fig. 3), a kernel is executed by a grid of thread blocks. A thread block is a batch of threads that can cooperate sharing data through shared memory and synchronizing their execution. Threads from different blocks operate independently.

Figure 4 shows the anatomy of the CUDA C/C++ program. Serial code executes on a CPU thread. Parallel code executes in many concurrent GPU threads across multiple parallel processing elements. The main limit with GPU computing is memory [7]. We worked with the 4 GB NVIDIA system, the best available till recently. Despite this limit, we have shown that for a single matrix equation, sizes up to 32768 x 37268 can be

broached (for the first order triangular finite element magnetostatic and temperature field devices we were working with [10]) without running into the limit [1]. This is quite a large problem and that is why seminal papers on GPU computation for finite elements do not mention this limit [2]-simply because they did not run into the limit. In parallelized genetic algorithm based optimization in inverse problems however [5,6], several finite element solutions have to be performed simultaneously. Memory limits therefore are critical. In the following sections we examine these limits with a view to establishing the practicality of parallelizing finite element optimization on the GPU for coupled field problems where the memory load is doubled by the two-stage finite element problem and exploded when several two-stage kernels are launched on parallel GPU threads in genetic algorithm optimization, because gradient methods of optimization run into problems of mesh discontinuity and programming complexities in keeping track of shape changes [10].

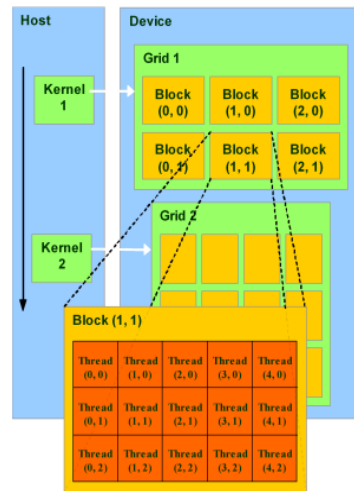


Fig. 3. The CUDA programming model.

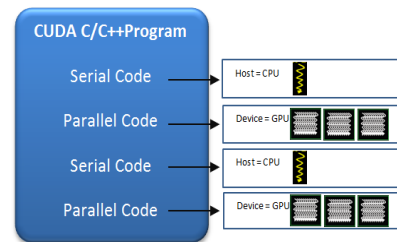


Fig. 4. Anatomy of the CUDA C/C++ program.

The test problem we finally take up is that of reshaping an originally square conductor which is heated by eddy currents (Fig. 5). The object is to have a constant temperature along a straight line. This paper being on parallelizing already forked kernels, the actual description of the geometry and analysis by first order triangular finite elements for the first stage problem from eddy current magnetics and the second stage by thermal analysis of the Poissonian temperature system (also with first order triangles), is left to references [10, 11]. In [11], the shape is optimized by gradient techniques, and [10] elaborates on the details of genetic algorithm optimization which are not taken up here but rather are left to [10].

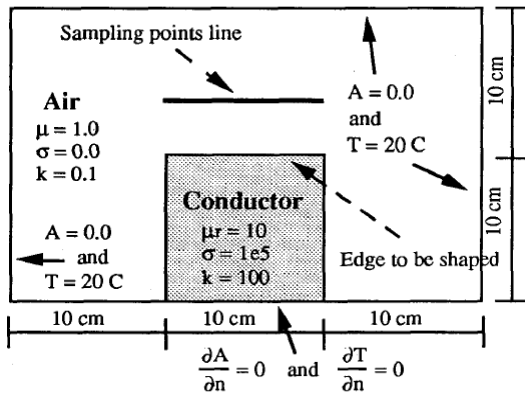


Fig. 5. The electro-thermal shape optimization by two-stage finite element analysis.

In this section, we investigate the standard sparse and profile matrix storage methods [3,4], in order to reduce the matrix storage requirement and to use those storage scheme representations to get the solution.

We began this study looking at the largest single precision matrix sizes we can store on a single GPU. Besides full matrix storage and even symmetric matrix storage, which we do not consider because of the memory need running into order n^2 for an $n \times n$ matrix, we looked particularly at profile storage and sparse storage [3,4]. Our findings are shown in Table 1. Clearly, neither sparse storage nor profile storage runs even close to the 4 GB memory limit (superseded today by the 12 GB limit [7]) at the practically large matrix size of 10,000. However, they could if we were launching several threads, each with a matrix solution, as required with the GPU implementation of the

genetic algorithm [5,6,8,10]. Therefore, we will confine ourselves to the sparse storage scheme, the better of the storage schemes as seen from Table 1.

Table 1: Storage demand with matrix size for different storage schemes

| Matrix Size | Storage (MB) | | |
|-------------|--------------|---------|--------|
| | Regular | Profile | Sparse |
| 100 | 0.0400 | 0.0044 | 0.0065 |
| 400 | 0.0686 | 0.0413 | 0.0169 |
| 900 | 3.1070 | 0.1271 | 0.0363 |
| 1,600 | 9.7961 | 0.2870 | 0.0703 |
| 2,500 | 23.8895 | 0.5438 | 0.1137 |
| 6,000 | 137.4435 | 1.5428 | 0.2734 |
| 8,000 | 244.2932 | 2.6614 | 0.3594 |
| 10,000 | 381.66046 | 4.0821 | 0.4502 |

A further study was done to compare the performance of different methods with sparse storage. As seen from Table 1 for sparse storage, the memory requirement is approximately 0.45 MB, even for the unlikely large matrix size of 10,000 x 10,000. For the two-stage problem therefore, we still need only 0.45 MB since the eddy current and thermal problems are solved in sequence, because the thermal solution needs the thermal Specific Absorption Rate (SAR) from the eddy current solution. With 4 GB available, 8000+parallel threads are allowed, corresponding to a genetic algorithm population of 8000+. Now that 8 GB is available to us [7], memory we conclude is not an issue, except for very large problems or when full storage is used.

III. ELEMENT-BY-ELEMENT FINITE ELEMENTS

In the mid-1980s, the then new IBM PC 286 had a memory limit of 612 KB, which could not hold even a trivial matrix in memory. To overcome this, researchers used the Jacobi method of matrix solution (also known as Gauss-Seidel by power systems engineers) in a modified form [3,4]. Practically, the Element-by-Element Finite Element Method (EbefEM) does not need a large amount of memory because it never stores or forms the global matrix except the diagonal. Generally, iterative algorithms such as the Jaccobi method, Conjugate Gradient method, etc., are used to get the solution of the problem [3]. During the 1980s, researchers could not represent big problems in

very limited memory so they used the EbEFEM method with an iterative method to represent very large problems [12]. Mahinthakumar and Hoole [13] used parallel implementation of the Jacobi conjugate gradients algorithm for field problems. In order to reduce the cost of memory, they used EbEFEM with the Jacobi Conjugate Gradients algorithm (JEBECG), which is very fast [13].

Figure 6 shows the sequential execution time against matrix size under for Incomplete Cholesky Conjugate Gradients (ICCG), Jacobi Conjugate Gradients (JCG) and Jacobi EbECG (JEBECG) on a SEQUENT SYMMETRY parallel computer for matrices from magnetic product design using first order triangles. Until matrix size 750, the ICCG method dominates; between 750 and 2500, JCG dominates rather than the other two methods; and for matrix size greater than 2500, JEBECG dominates.

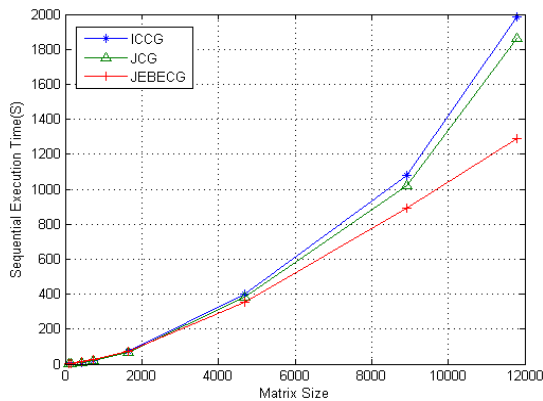


Fig. 6. Sequential execution times for ICCG, JCG, and JEBECG methods for matrix sizes.

Figure 7 for parallel implementation on the same shared memory machine using all its 4 processors shows similar findings. One processor does book-keeping, and with the 3 remaining processors working in parallel, the speedup is 2 or less (and not 3 because of communication bottlenecks). It is critical to note that more processors are not available for faster computation; nor to parallelize the genetic algorithm, and in one such genetic algorithm thread to parallelize matrix solution.

For matrix size under 500, ICCG dominates; for matrix size between 500 and 1800, JCG dominates; and for matrix size greater than 1800, JEBECG dominates. For simple problems,

conjugate gradient schemes with sparsity computation or renumbering are suitable. It is not widely recognized that although renumbering: a) is necessary only for reducing storage in ICCG and Cholesky schemes of solution, and b) speeds up Cholesky by reducing fill-in, we are able to show that in ICCG it also unintentionally speeds up computations because the approximate Cholesky preconditioner gets to be more accurate [3]. For large problems, the element-by-element scheme is very profitable because it does not need matrix formation computation and storage capacity for the global matrix.

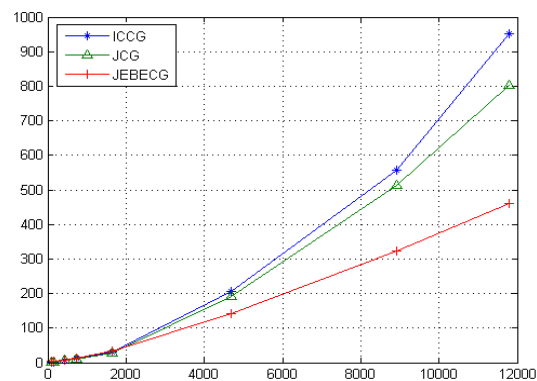


Fig. 7. Parallel execution times for ICCG, JCG, and JEBECG methods for matrix sizes.

IV. ELEMENT-BY-ELEMENT GAUSS-SEIDEL METHOD ON THE GPU

First, we will describe the element-by-element scheme [8-13] which we are going to exploit for parallelizing already parallelized kernels. In solving the finite element matrix equation:

$$[P]\{\phi\} = \{Q\}, \quad (1)$$

far more powerful methods exist like the Incomplete Cholesky-preconditioned Conjugate Gradients algorithm (ICCG) than the older Gauss-Seidel iterations. The Gauss-Seidel iterations, commonly used by power engineers, are an improvement on the even older Gauss iterations. In Gauss-Seidel in each iteration $m+1$ we use the latest available values of the unknowns ϕ , using equation i of (1) to compute ϕ_i , treating only ϕ_i as the unknown and all the other variables as known and given by their latest values, some from the present iteration $m+1$ and the rest from the previous iteration m :

$$\phi_i^{m+1} = \frac{1}{P_{ii}} \left(Q_i - \sum_{k=1}^{i-1} P_{ik} \phi_k^{m+1} - \sum_{k=i+1}^n P_{ik} \phi_k^m \right), \quad (2)$$

with obvious modifications for $i=1$ and $i=n$. In this algorithm, ϕ_{i-1} must be computed before ϕ_i . Here at iteration $m+1$, computing ϕ_i in the order $i=1$ to n , ϕ is at values of iteration $m+1$ up to the $(i-1)$ th component of $\{\phi\}$ and at the value of the previous iteration m for values after i . The original Gauss iterations (improved by Gauss-Seidel) uses the old iteration m 's values for computing all ϕ_i in iteration $m+1$ according to:

$$\phi_i^{m+1} = \frac{1}{P_{ii}} (Q_i - \sum_{k=1}^{i-1} P_{ik} \phi_k^m - \sum_{k=i+1}^n P_{ik} \phi_k^m). \quad (3)$$

This is inefficient in the context of sequential computations. But in this case of parallelization, if we can resort to this conventionally inefficient method, we need not form the matrix $[P]$. If $[D]$ is the matrix $[P]$ with all off diagonal elements eliminated, then the Gauss iterations in this modified form gives:

$$[D]\{\phi\}^{m+1} = Q - [P - D]\{\phi\}^m. \quad (4)$$

Thus, without forming $[P]$, the operations of the right hand side of (3) can be effected by taking each first order triangular finite element in turn, computing its local 3×3 Dirichlet matrix $[P]^L$ and using that because,

$$[P] = \sum_{elements} [P]^L. \quad (5)$$

So as each $[P]^L$ is formed, the three values of $\{\phi\}^m$ may be taken and subtracted as in the right hand side of (3) or (4) as justified by (5). Only the diagonal elements of $[P]$ are stored so as to be able to divide by $P_{ii} = D_i$ as required in (3) and (4) quickly. Figure 8 shows the speedup of the element-by-element Gauss iterations. The speedup keeps increasing, seemingly endlessly, as matrix size goes up.

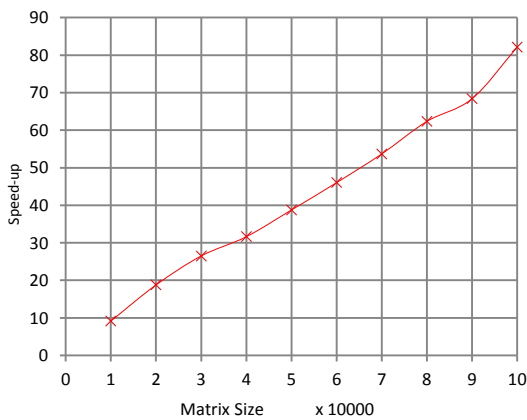


Fig. 8. Speedup for element-by-element Gauss iterations with matrix size.

For comparison we also parallelized on the GPU the ICCG algorithm with matrix storage-Incomplete Cholesky preconditioning requires $[P]$. From the results (Fig. 9), it is seen that the speedup is much lower than by element-by-element Gauss iterations, and saturates with matrix size because of the increased communications in forming and dealing with the matrix that is stored. But these figures are much faster than the speedup from 6 to 90-something reported by Kiss, *et al.* [7], presumably because of programming efficiency.

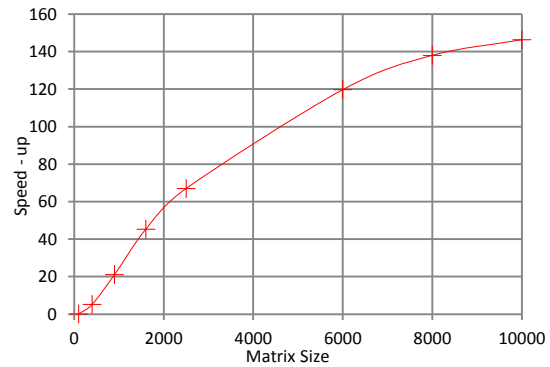


Fig. 9. Incomplete Cholesky conjugate gradients algorithm: matrix size vs. CPU time/GPU time.

V. NEW DEVELOPMENT IN CUDA

Thus far, parallelization in CUDA has not allowed parallelism within parallelism. Although it is allowed in multiprocessor machines, it was not very useful in finite element analysis, because shared memory machines with 4, 8, 16 or rarely 32 processors did not have spare processors to devote to parallel threads branching off from an already parallelized thread. (Supercomputers with more processors are not considered in this discussion because they are not readily available).

But CUDA 5.0 recently introduced support for forking into branches an already parallelized stream. This feature is a major breakthrough of the CUDA programming paradigm because CUDA allows many threads to be supported. This in turn allows a kernel to be launched and synchronized with new grids directly from the GPU using CUDA's standard `<<< >>>` syntax. A broad subset of the CUDA runtime API is now available on the device, allowing launch, synchronization, streams, events, and more. CUDA Dynamic Parallelism is available only on SM 3.5 architecture GPUs [14].

Since SM3.5 still has not come to PCs, we merely stick here to the single forking approach in determining what part of a kernel on a forked thread is to be further forked. In our work, we use the genetic algorithm where the object function corresponding to every member \bar{h} of a population has to be computed many times to find the minimum. The many members \bar{h} form the genetic search space. Since \bar{h} consists of dimensions and materials of a particular design being examined for its goodness [15], for those dimensions a mesh is constructed, the finite element problem solved and the object function evaluated. The object function itself is computed from a finite element solution involving a matrix equation. Thus, we may treat the object function computation as a kernel and launch it on multiple threads, each for a different member of the population. Then, within that thread, as things are now on a PC, we can parallelize the matrix equation solution at a speedup of 147 and more by ICCG (Fig. 9) and even more by Gauss (Fig. 8). Alternatively, we may do the object function evaluation for each member of the population in sequence and in that process parallelize the matrix computations. Let the population number be n . Say the object function evaluation for each member of the population takes $t_0 + t_m$ in time where t_m is the time for the matrix solution and t_0 the time for other operations. Therefore, if we parallelize the operations for different members of the population, evaluating time for all object functions corresponding to the entire population would still be, neglecting coordination time,

$$t = t_0 + t_m, \quad (6)$$

since these are done simultaneously. Here, we assume that the work for each member of the population being done in parallel, the time for combining results and other communications is negligible.

On the other hand, if we parallelized the matrix computation, the evaluation of the object function has to be in sequence since we cannot have forking from a parallelized kernel. The total time would then be the number of members in the population multiplied by the time for computing the object function for each member of the population:

$$t = n \left(t_0 + \frac{t_m}{147} \right). \quad (7)$$

Here, we have assumed that the speedup of 147 we have obtained for matrix solution by ICCG (Fig.

9) for matrix size upward of 10,000 would be achievable. A decision on which of the processes is to be parallelized would depend on considerations like this. However, we have not seen such considerations in the literature. On this basis, we found it better with a population size of 512 we were dealing with [10] to parallelize the population evaluation. The results are in Fig. 10, where the speedup saturates around 28 because of communication issues as the population rises.

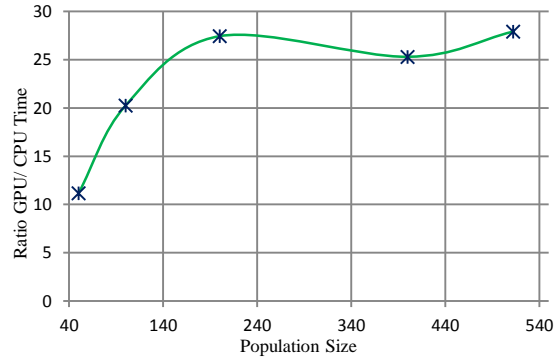


Fig. 10. Speedup: GA optimization GPU time/CPU time with population size.

VI. CONCLUSIONS

GPU parallelization is far superior to using multiprocessor machines because unlimited threads can launch computational kernels in parallel. While multiprocessor machines can fork a thread already running in parallel, they lack the processors that can be allocated. Although GPU cards till now did not allow a forked process to be further parallelized, this is being addressed by new architectures, such as the SM 3.5 architecture GPU [14]. For the vast majority of PCs with a GPU card but with dynamic parallelism not available, we have presented the methodology for deciding which one of the processes should be implemented in parallel to obtain the best speedup.

In GPU computing, the memory of the NVIDIA GPU is limited and this affects optimization work rather than the direct problem, because of the need to keep several copies of the matrix of coefficients in each genetic algorithm thread. The sparse storage scheme is the most efficient way to represent the matrix for finite element optimization. With it, only very large problems will find memory an obstacle, and for that class of problems, the element-by-element method

can be used.

If we use element-by-element FEM, practically unlimited size of problems can be solved without storing any matrix. GPU computation for finite element optimization by the genetic algorithm affords significant speedup. Element-by-element GPU matrix solution has even better speedup without saturating.

ACKNOWLEDGEMENTS

This work was funded in part by the US Army's Tank, Automotive Research, Development and Engineering Center (TARDEC), under contract number W911NF-11-D-0001. This paper has been approved by the US Army's Tank, Automotive Research, Development and Engineering Center (TARDEC) with the statement: "UNCLASSIFIED: Distribution Statement A. Approved for public release."

REFERENCES

- [1] S. Sivasuthan, V. U. Karthik, and S. R. H. Hoole, "CUDA memory limitation in finite element optimization to reconstruct cracks," pp. 1967-1974 in D. E. Chimenti, L. J. Bond, and D. O. Thompson (eds.), *40th Annual Review of Progress in Quantitative Nondestructive Evaluation, AIP Conference Proceedings 1581, American Institute of Physics, Melville, NY, 2014.*
- [2] C. Cecka, A. J. Lew, and E. Darve, "Assembly of finite element methods on graphics processors," *IJNME*, vol. 85, no. 5, pp. 640-669, 2011.
- [3] S. R. H. Hoole, "Computer aided analysis and design of electromagnetic devices," Elsevier, NY, 1989.
- [4] D. R. Kincaid, J. R. Respass, D. M. Young, and R. G. Grimes, "Algorithm 586: ITPACK 2C: a FORTRAN package for solving large sparse linear systems by adaptive accelerated iterative methods," *ACM Trans. Math. Software*, vol. 8, no. 3, pp. 302-322, 1982.
- [5] M. L. Wong and T. T. Wong, "Implementation of parallel genetic algorithms on graphics processing units," pp. 197-216 in M. Gen, D. Green, O. Katai, B. McKay, A. Namatame, R. A. Sarkar, and B. T. Zhang (eds.), *Intelligent and Evolutionary Systems, Book Series: Studies in Computational Intelligence*, vol. 187, Springer, 2009.
- [6] D. Robilliard, V. Marion-Poty, and C. Fonlupt, "Genetic programming on graphics processing units," *Genetic Programming and Evolvable Machines*, vol. 10, no. 4, pp. 447-471, 2009.
- [7] <http://www.newegg.com/Product/Product.aspx?Item=N82E16814133494>, Downloaded July 1, 2014.
- [8] S. Sivasuthan, V. U. Karthik, A. Rahunathan, P. Jayakumar, R. Thyagarajan, L. Udpa, and S. R. H. Hoole, "GPU computation: why element by element conjugate gradients?," *Sixteenth Biennial IEEE Conference on Electromagnetic Field Computation, Annecy France, May 25-28, 2014.*
- [9] I. Kiss, S. Gyimothy, Z. Badics, and J. Pavo, "Parallel realization of element-by-element FEM technique by CUDA," *IEEE Trans. Magnetics*, vol. 48, no. 2, pp. 507-510, 2012.
- [10] V. U. Karthik, S. Sivasuthan, A. Rahunathan, R. S. Thyagarajan, P. Jeyakumar, L. Udpa, and S. R. H. Hoole, "Faster, more accurate parallelized inversion for shape optimization in electroheat problems on a graphics processing unit (GPU) with the real-coded genetic algorithm," *ECE Dept., Michigan State University, available from authors*, (also COMPEL-Paper under advanced stage of review).
- [11] T. Pham, S. Ratnajeewan, and H. Hoole, "Unconstrained optimization of coupled magneto-thermal problems," *IEEE Trans. Magnetics*, vol. 31, no. 3, pp. 1988-1991, 1994.
- [12] J. T. Hughes, I. Levit, and J. Winget, "An element-by-element solution algorithm for problems of structural and solid mechanics," *Comp. Meth. in App. Mech. & Eng.*, vol. 36, no. 2, pp. 241-254, 1983.
- [13] G. Mahinthakumar and S. R. H. Hoole, "A parallelized element by element jacobi conjugate gradients algorithm for field problems and a comparison with other schemes," *Int. J. App. Electromag. in Matl.*, vol. 1, no. 1, pp. 15-28, 1990.
- [14] <http://docs.nvidia.com/cuda/cuda-toolkit-release-notes/index.html>.
- [15] E. R. Laithwaite, "The goodness of a machine," *Electron. & Power*, vol. 11, no. 3, pp. 101-103, 1965.



S. Ratnajeewan H. Hoole is a Professor of Electrical and Computer Engineering at Michigan State University. He has previously served as Member of the University Grants Commission of Sri Lanka where with six others he regulated the administration of all 15 Universities in that country. He also briefly was Vice Chancellor, University of Jaffna. A Fellow of the IEEE, he holds a Ph.D. degree from Carnegie Mellon University and a higher doctorate, the D.Sc. (Eng.) degree, from London. Besides Engineering, he has contributed much to the learned literature in the humanities and social sciences.



Sivamayam Sivasuthan was born in Sri Lanka, and received his B.Sc. degree First Class Hons. in Computer Science from the University of Jaffna. He has been reading for a doctoral degree in Electrical and Computer Engineering at Michigan State University since January 2012. His thesis focuses on exploiting graphics processing units to parallelize finite element optimization.



Victor U. Karthik was born in Sri Lanka, and received his B.Sc. Hons in Electrical and Electronics Engineering from the University of Peradeniya, Sri Lanka. He has been reading for a doctoral degree in Electrical and Computer Engineering at Michigan State University since January 2012. His thesis focuses on the genetic algorithm to optimize electro-heat problems for application in machine design and hyperthermia.



Arunasalam Rahunathan has a Ph.D. degree in Mathematics from the University of Wyoming and a B.Sc. Engineering degree from the University of Peradeniya in Sri Lanka. He is currently an Instructor in the Department of Mathematics and Computer Science at the Edinboro University of Pennsylvania. His research interests include numerical methods for ODEs and PDEs, mathematical modeling of multiphase flows in multiscale porous media using Graphics Processing Units (GPUs) and Bayesian inference for quantifying uncertainty in problems related to subsurface flows.



Ravi Thyagarajan currently serves as Deputy Chief Scientist at the U.S. Army Tank Automotive Research, Development and Engineering Center (TARDEC), and was selected to the Researcher Review Board as a Senior Technical Specialist in June 2012.

His research pursuits are in the areas of underbody blast modeling and design, occupant protection and fast-running modeling methodologies. He received his Ph. D. degree in Applied Mechanics from Caltech, and has over 15 years of prior experience in the automotive industry at Ford and Visteon, where he was involved in all aspects of product development of automotive interiors. His

automotive experience includes leadership roles in concept-to-launch product design, human factors/ergonomics development, as well as in the standardized application of CAE tools during the overall design engineering process, for which he won several awards, including the President's level Customer-Driven Quality award.

He is a past recipient of the Forest R McFarland Award from SAE, holds two patents and has co-authored over 40 technical papers. He received the Army Materiel Command (AMC) Systems Analysis awards in 2010 and 2012, for pioneering application of modeling and simulation methodologies in underbody blasts. He is also a Member of the Army Acquisition Corps, and is a Certified Acquisition Professional in Systems Engineering (SE), Program Management (PM) and Science & Technology (S&T) Management.



Paramsothy Jayakumar is a Senior Research Scientist, SAE Fellow, and a member of the Analytics Team at the U.S. Army Tank Automotive Research, Development, & Engineering Center (TARDEC) in Warren, Michigan. Prior to joining U.S. Army TARDEC, he worked for BAE Systems, Ford Motor Company, Altair Engineering, and Engineering Mechanics Research Corporation in the areas of multibody dynamics software development, vehicle dynamics modeling & simulation consulting, simulation technology development, durability load simulation, vehicle instrumentation & loads measurement, and road load engineering.

Jayakumar has written more than 100 journal and conference papers. His research in terramechanics and multibody dynamics won the best paper awards at the NDIA's Ground Vehicle Systems Engineering and Technology Symposium in 2011 and 2012. He holds a U.S. patent for a system for virtual prediction of road loads and tire modeling. He was also instrumental in developing seven SAE standards for tire testing for the purpose of tire modeling for which he received the SAE 2014 James M. Crawford Technical Standards Board Outstanding Achievement Award.

Jayakumar is a member of the U.S. Army Acquisition Corps, an Honorary Fellow of the Department of Mechanical Engineering at the University of Wisconsin-Madison, and an Associate Editor for the ASME Journal of Computational and Nonlinear Dynamics. He received his M.S. and Ph.D. degrees in Structural Dynamics from Caltech, and B.Sc. Eng. (Hons, First Class) from the University of Peradeniya, Sri Lanka.

An UWB Microstrip-Fed Slot Antenna with Enhanced Bandwidth and WLAN Band-Notched Characteristics

Yasser Ojaroudi ¹, Sajjad Ojaroudi ¹, and Nasser Ojaroudi ²

¹ Young Researchers and Elite Club, Germe Branch
Islamic Azad University, Germe, Iran

² Young Researchers and Elite Club, Ardabil Branch,
Islamic Azad University, Ardabil, Iran
n.ojaroudi@yahoo.com

Abstract — In this paper, a compact Ultra-Wideband (UWB) slot antenna with band-notched performance is presented. In order to increase the impedance bandwidth of an ordinary slot antenna, we use a pair of S-shaped slots in the ground plane that with this structure, a new resonance at the higher frequencies can be achieved and a wide usable fractional bandwidth of more than 130% is provided. Additionally, by using a protruded E-shaped strip inside the square-ring radiating patch, a frequency band-notched function has been obtained. The designed antenna has a small size of 20×20 mm² while showing the radiation performance in the frequency band of 3.13 to over 14.3 GHz, with a band rejection performance in the frequency band of 5 to 6 GHz. Simulated and experimental results obtained for this antenna show that it exhibits good radiation behavior within the UWB frequency range.

Index Terms — Band-notched function, microstrip-fed slot antenna, UWB systems.

I. INTRODUCTION

In UWB communication systems, one of key issues is the design of an antenna while providing wideband characteristic over the whole operating band. Consequently, a number of microstrip antennas with different geometries have been experimentally characterized [1-2]. Moreover, other strategies to improve the impedance bandwidth have been investigated [3-5].

The frequency range for UWB systems between 3.1-10.6 GHz will cause interference to the existing wireless communication systems, for

example the Wireless Local Area Network (WLAN) for IEEE 802.11a operating in 5.15-5.35 GHz and 5.725-5.825 GHz bands, so the UWB antenna with band-notched function is required [6-9].

In this paper, a compact microstrip-fed slot antenna with band-notched characteristic for UWB applications has been designed and manufactured. In the proposed design, by cutting a pair of S-shaped slots in the ground plane, an additional resonance at middle frequencies was excited. By obtaining this resonance, the usable upper frequency of the antenna is extended from 9.3 GHz to 14.3 GHz. To generate a frequency band-notched function, we use a square-ring stub with rotated E-shaped strip protruded inside the square ring [6]. The designed antenna has a small size of $20 \times 20 \times 0.8$ mm³, and the impedance bandwidth of the designed slot antenna is higher than the UWB antennas reported recently [1-3].

II. ANTENNA DESIGN

The proposed slot antenna fed by a 50- Ω microstrip line is shown in Fig. 1, which is printed on an FR4 substrate of thickness 0.8 mm and permittivity of 4.4. The width of the microstrip feed line is fixed at 1.5 mm. The basic antenna structure consists of square radiating stub, feed line, and slotted ground plane.

In the proposed antenna, the square-ring stub with a protruded E-shaped strip inside the ring is connected to a feed line, as shown in Fig. 1. On the other side of the substrate, a conducting ground plane with a pair of S-shaped slots is placed. The proposed antenna is connected to a

50- Ω SMA connector for signal transmission. Final dimensions of the designed antenna are shown in Table 1.

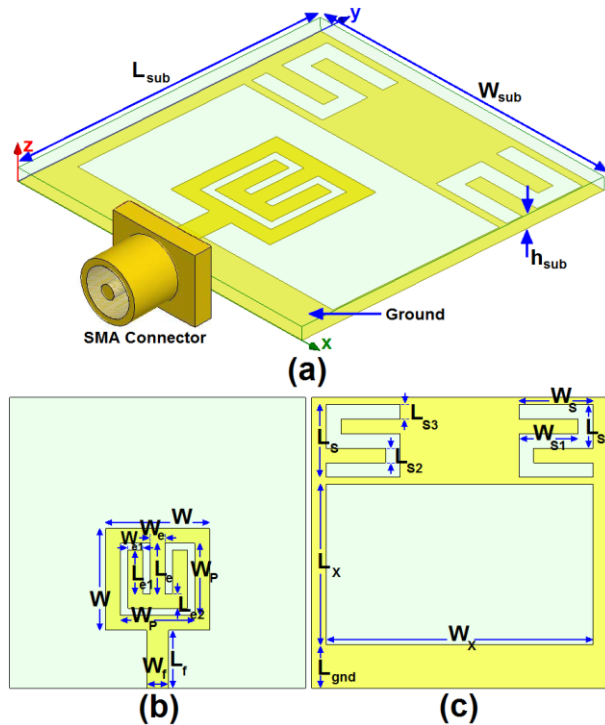


Fig. 1. Geometry of the proposed microstrip-fed slot antenna: (a) side view, (b) top layer, and (c) bottom layer.

Table 1: The final dimensions of the antenna

| Param. | mm | Param. | mm | Param. | mm |
|-----------|-----|-----------|------|-----------|------|
| W_{sub} | 20 | L_{sub} | 20 | W | 7 |
| W_S | 5 | W_P | 4.5 | W_X | 18 |
| L_X | 11 | W_f | 1.5 | L_f | 4 |
| W_{S1} | 4 | L_{S1} | 3.25 | W_{S2} | 1 |
| L_{S2} | 0.5 | L_{S3} | 1.25 | L_{S4} | 0.5 |
| W_e | 1 | L_e | 3 | W_{e1} | 0.75 |
| L_{e1} | 2.5 | L_{e2} | 0.75 | L_{gnd} | 3 |

In this work, we start by choosing the aperture length L_S . We have a lot of flexibility in choosing this parameter. The length of the aperture mostly affects the antenna bandwidth. As L_S decreases, so does the antenna BW and vice versa. In the next step, we have to determine the aperture width W_S . The aperture width is approximate, whereas the slot wavelength, that depends on a number of parameters such as the slot width as well as the thickness and dielectric constant of the substrate

on which the slot is fabricated. The following step in the design is to choose the width of the radiating patch W . This parameter is approximate, whereas the guided wavelength is the microstrip line [3]. The last and final step in the design is to choose the length of the resonator and the band-stop filter elements. In this design, the optimized length $L_{resonance}$ is set to resonate at $0.25\lambda_{resonance}$, where $L_{resonance}=L_{S1}+L_{S2}+L_{S2}+0.5 W_{S1}$. Also, the optimized length L_{notch} is set to band-stop resonate at $0.5\lambda_{notch}$, where $L_{notch}=L_e+0.5(W_{e1}+L_{e1})+W_P-W_e$. λ_{notch} corresponds to band-notched frequency (5.5 GHz).

In this study, to design a novel antenna, the modified S-shaped Defected Ground Structures (DGSs) is placed inside the ground plane. Regarding ECT, by inserting these structures in the substrate backside, additional coupling is introduced between the radiating stub and the ground plane, and the antenna impedance bandwidth is improved without any cost of size or expense. Moreover, these structures change the inductance and capacitance of the input impedance, which in turn leads to change the bandwidth [4-6]. In addition, to create a desired frequency band-stop characteristic, an inverted E-shaped strip which protruded inside square-ring radiating stub is used. At the notched frequencies, the current flows are more dominant around the E-shaped structure, and they are oppositely directed between the embedded structure and the radiating stub. As a result, the desired high attenuation near the notched frequency can be produced [10-11].

III. RESULTS AND DISCUSSIONS

The proposed microstrip-fed slot antenna with various design parameters was constructed, and the numerical and experimental results of the input impedance and radiation characteristics are presented and discussed. The Ansoft simulation software High-Frequency Structure Simulator (HFSS) [12] is used to optimize the design.

The configuration of the presented slot antenna is shown in Fig. 1. Configuration of the ordinary slot antenna [Fig. 2 (a)], the antenna with a pair of S-shaped slots in the ground plane [Fig. 2 (b)], and the proposed antenna [Fig. 2 (c)] are shown in Fig. 2. Return loss characteristics for the structures shown in Fig. 2 are compared in Fig. 3. As illustrated, it is observed that the upper frequency bandwidth is affected by using the pair

of S-shaped slots in the ground plane, and the notched frequency bandwidth is sensitive to the rotated E-shaped strip inside the square-ring radiating stub.

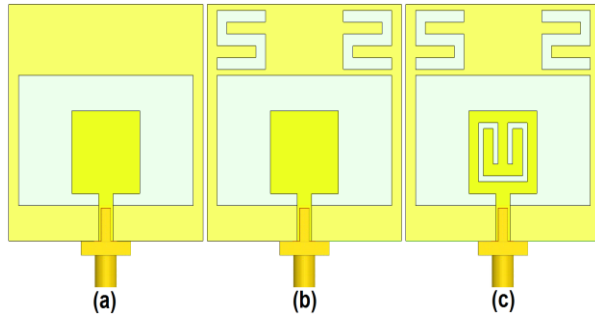


Fig. 2. (a) Ordinary slot antenna, (b) antenna with a pair of S-shaped slots in the ground plane, and (c) the proposed slot antenna.

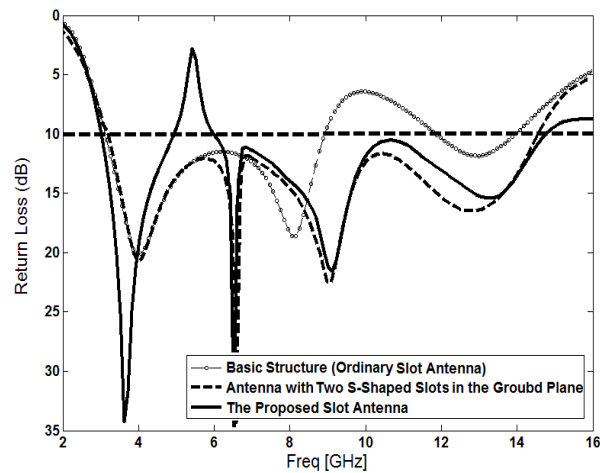


Fig. 3. Simulated return loss characteristics for the various antennas shown in Fig. 2.

To understand the phenomenon behind the additional resonance performance, the simulated current distributions in the ground plane for the proposed antenna at 6.7 GHz is presented in Fig. 4 (a). It is found that by using the S-shaped slots, a new resonance at 6.7 GHz can be achieved. Another important design parameter of this structure is the rotated E-shaped strip inside the square ring stub. Figure 4 (b) presents the simulated current distributions on the radiating stub at the notched frequency (5.5 GHz). As seen, at the notched frequency, the current flows are more dominant around of the rotated E-shaped

strip [13-15]. Simulated input impedance results of the proposed antenna on a Smith Chart is shown in Fig. 5.

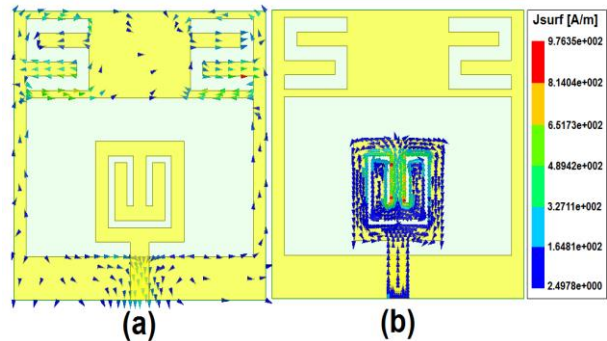


Fig. 4. Simulated surface current distributions for the proposed antenna: (a) in the ground plane at 6.7 GHz, and (b) on the radiating stub at 5.5 GHz.

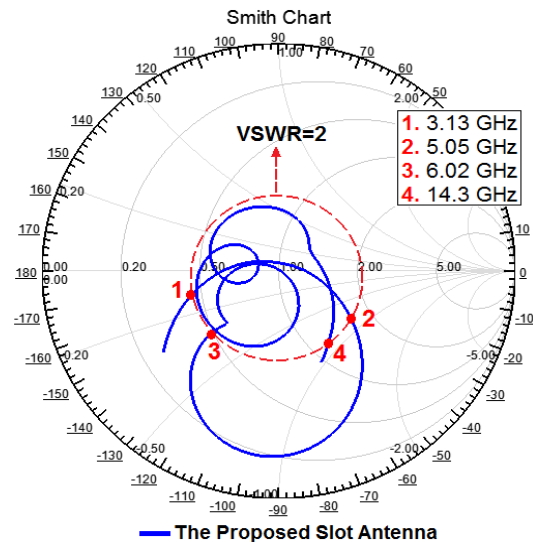


Fig. 5. Simulated Smith Chart results of proposed slot antenna.

In this study, a rotated E-shaped strip protruded inside the square ring stub with variable dimensions is used to generate the frequency band-stop performance [16-18]. The simulated VSWR curves with different values of L_e are plotted in Fig. 5. As shown in Fig. 6, when the length of the rotated E-shaped strip increases from 0.75 to 2 mm, the center of notched frequency is decreased from 7.2 to 5.1 GHz. From this result, we can conclude that the notched frequency is controllable by changing the length of L_e .

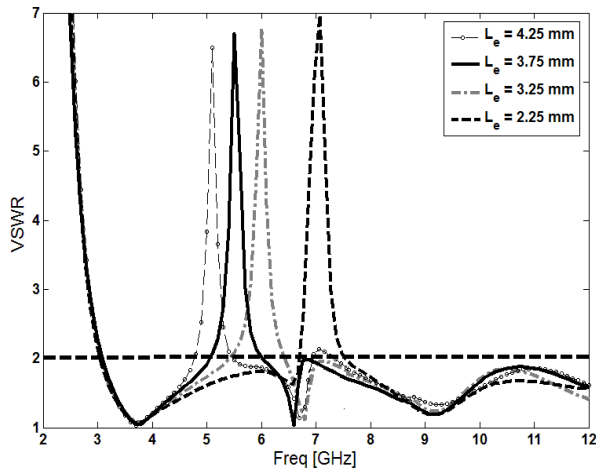


Fig. 6. Simulated VSWR characteristics for the proposed antenna with different values of L_e .

Another main effect of the rotated E-shaped strip occurs on the filter bandwidth. In the presented structure, the width of W_{e1} is the critical parameter to control the filter bandwidth. Figure 7 illustrates the simulated VSWRs with different values of W_{e1} . As the exterior width of the W_{e1} increases from 0.25 to 1 mm, the notched frequency bandwidth is varied from 0.73 to 1.5 GHz. Therefore, the bandwidth of notched frequency is controllable by changing the width of W_{e1} .

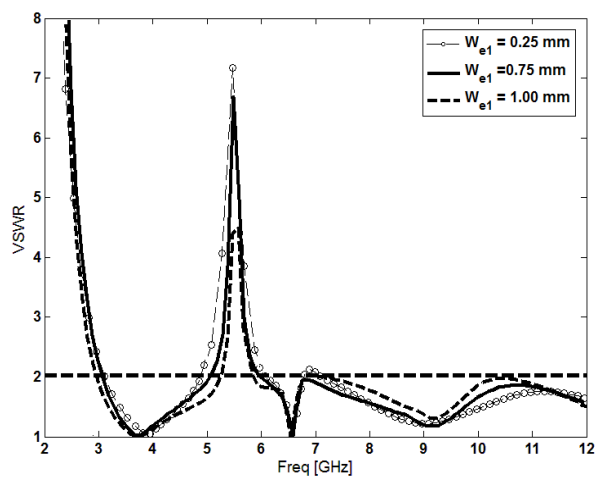


Fig. 7. Simulated VSWR characteristics for the proposed antenna with different values of W_{e1} .

The proposed antenna with final design as shown in Fig. 8, was built and tested. The VSWR characteristic of the antenna was measured using

the HP 8720ES network analyzer.

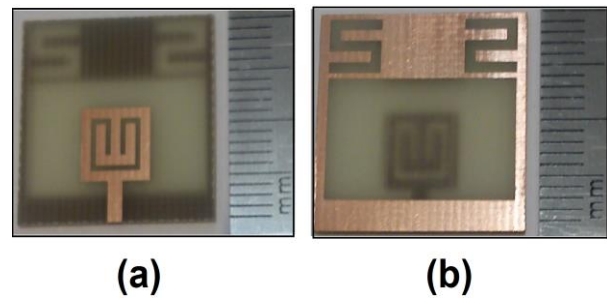


Fig. 8. Fabricated antenna: (a) top view, and (b) bottom view.

The radiation patterns have been measured inside an anechoic chamber using a double-ridged horn antenna as a reference antenna placed at a distance of 2 m. Also, two-antenna technique using an Agilent E4440A spectrum analyzer and a double-ridged horn antenna as a reference antenna placed at a distance of 2 m, is used to measure the radiation gain in the z axis direction (x - z plane). Measurement set-up of the proposed antenna for the VSWR, antenna gain and radiation pattern characteristics are shown in Fig. 9.

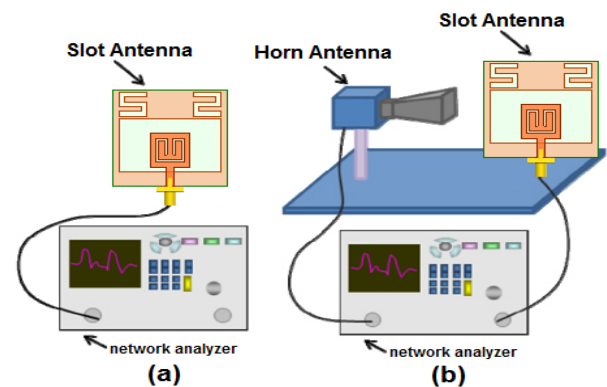


Fig. 9. Measurement set-up of the proposed antenna: (a) VSWR, and (b) antenna gain and radiation patterns.

The measured and simulated VSWR characteristic of the proposed antenna was shown in Fig. 10. The fabricated antenna has the frequency band of 3.13 to over 14.31 GHz with a rejection band around 5 to 6 GHz. However, as seen, there exists a discrepancy between the measured data and simulated results. This discrepancy is mostly due to a number of

parameters, such as the fabricated antenna dimensions as well as the thickness and dielectric constant of the substrate on which the antenna is fabricated, and the wide range of simulation frequencies. In a physical network analyzer measurement, the feeding mechanism of the proposed antenna is composed of a SMA connector and a microstrip line (the microstrip feed-line is excited by a SMA connector), whereas the simulated results are obtained using the Ansoft simulation software (HFSS); that in HFSS by default, the antenna is excited by a wave port that it is renormalized to a 50-Ohm full port impedance at all frequencies. In order to confirm the accurate return loss characteristics for the designed antenna, it is recommended that the manufacturing and measurement processes need to be performed carefully. Moreover, SMA soldering accuracy and FR4 substrate quality need to be taken into consideration.

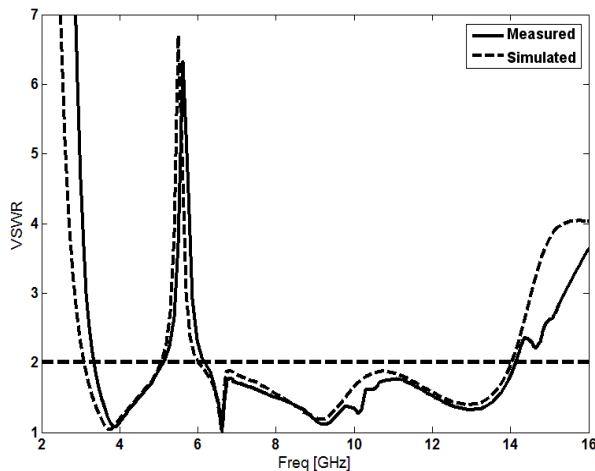


Fig. 10. Measured and simulated VSWR characteristics of the proposed antenna.

Figure 11 depicts the measured and simulated radiation patterns of the proposed antenna, including the co-polarization and cross-polarization in the H-plane (x-z plane) and E-plane (y-z plane). It can be seen that quasi-omnidirectional radiation pattern can be observed on x-z plane over the whole UWB frequency range, especially at the low frequencies.

The radiation pattern on the y-z plane displays a typical figure-of-eight, similar to that of a conventional dipole antenna. It should be noticed that the radiation patterns in E-plane become

imbalanced as frequency increases because of the increasing effects of the cross-polarization. The patterns indicate at higher frequencies; more ripples can be observed in both E- and H-planes owing to the generation of higher-order modes [19-20].

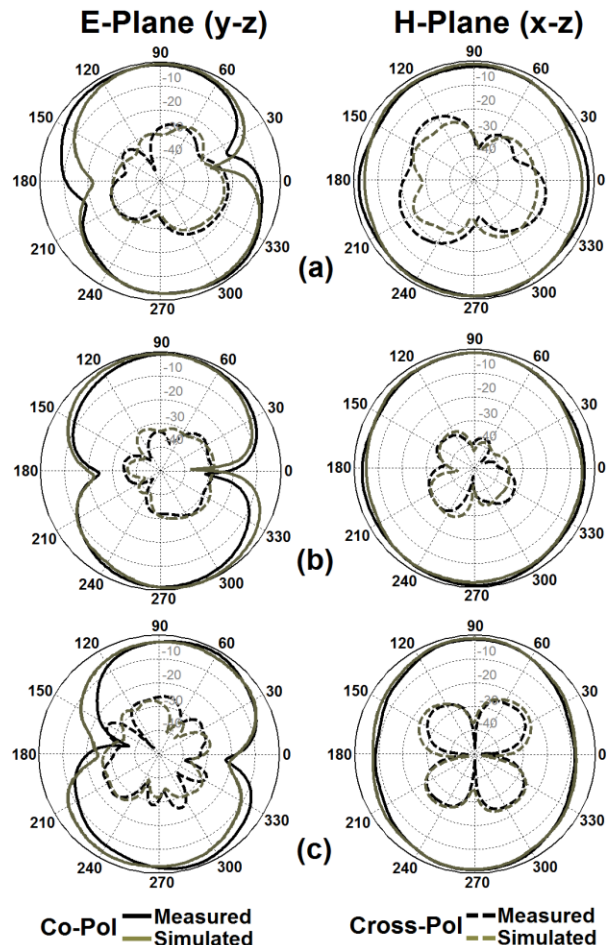


Fig. 11. Measured and simulated radiation patterns of the proposed antenna: (a) 3.5 GHz, (b) 7 GHz, and (c) 10 GHz.

Measured and simulated maximum gains of the proposed antenna w/o band-notched function were shown in Fig. 12. As illustrated, a sharp decrease of measured maximum gain in the notched frequency band at 5.5 GHz is shown in Fig. 9. For other frequencies outside the notched frequency band, the antenna gain with the filter (measured) is similar to this without it (simulated). As seen, the proposed antenna has sufficient and acceptable gain levels in the operation bands [21-22].

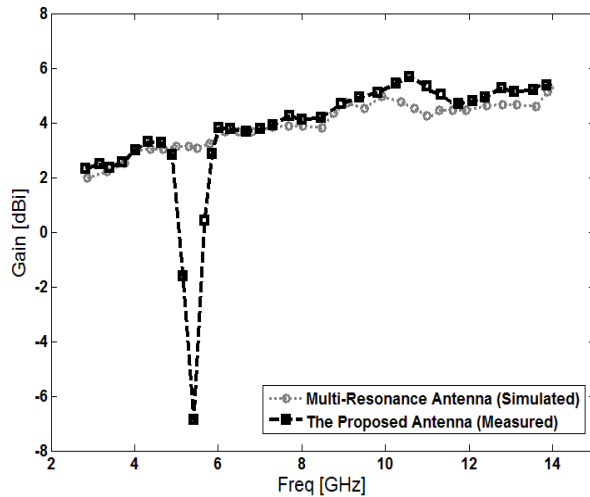


Fig. 12. Measured and simulated maximum gains for the proposed antenna.

Table 2 summarizes the previous UWB microstrip slot designs and the proposed antenna [23-30]. As seen, the proposed antenna has a compact size with very wide bandwidth, compared with the previous works. In addition, in comparison with previous band-notched antennas, the proposed antenna displays a good omnidirectional radiation pattern, even at lower and higher frequencies. Also, the proposed microstrip-fed slot antenna has sufficient and acceptable antenna gain, co- and cross-polarization levels in the operation bands.

Table 2: Comparison of previous UWB microstrip slot antennas with the proposed design

| Ref. | Size (mm ²) | Bandwidth (VSWR<2) | Gain (dBi) |
|------------------|-------------------------|--------------------|--------------|
| [23] | 22×8.5 | 3.1-10.6 GHz | 1.5~3.5 |
| [24] | 45×50 | 2.9-10.8 GHz | 4-7 |
| [25] | 100×100 | 3.1-12.0 GHz | 2-8 |
| [26] | 60×60 | 1.5-11.1 GHz | 3-8 |
| [27] | 24×24 | 2.8-12.0 GHz | 2.5-6.5 |
| [28] | 32×24 | 2.9-12.5 GHz | 2~6 |
| [29] | 30×30 | 1.8-12.4 GHz | 2.5-5.5 |
| [30] | 25×25 | 2.6-13.0 GHz | not reported |
| <i>This work</i> | 20×20 | 3.1-14.3 GHz | 2.2~5.7 |

IV. CONCLUSION

In this paper, a novel design of ultra-wideband slot antenna with variable band-notched function is proposed. The presented slot antenna can

operate from 3.13 to over 14.31 GHz with VSWR < 2, and with a rejection band around 5 to 6 GHz. By using a pair of S-shaped slots in the ground plane, additional resonance at the higher frequencies is excited and much wider impedance bandwidth can be produced. In order to generate a frequency band-stop performance, we use the square ring radiating stub with a rotated E-shaped strip inside the stub. The measured results show good agreement with the simulated and measured results. Experimental results show that the presented slot antenna could be a good candidate for UWB applications.

ACKNOWLEDGMENT

The authors are thankful to MWT Company staff for their help (www.microwave-technology.com).

REFERENCES

- [1] J. Y. Sze and K. L. Wong, "Bandwidth enhancement of a microstrip line-fed printed wide-slot antenna," *IEEE Trans. Antennas Propag.*, vol. 49, pp. 1020-1024, 2001.
- [2] Y. W. Jang, "Experimental study of large bandwidth three-offset microstrip line-fed slot antenna," *IEEE Microw. Wireless Comp. Lett.*, vol. 11, pp. 425-426, 2001.
- [3] N. Ojaroudi, "Design of ultra-wideband monopole antenna with enhanced bandwidth," *21st Telecommunications Forum, TELFOR 2013*, Belgrade, Serbia, pp. 1043-1046, November 27-28, 2013.
- [4] N. Ojaroudi, "A new design of koch fractal slot antenna for ultra-wideband applications," *21st Telecommunications Forum, TELFOR 2013*, Belgrade, Serbia, pp. 1051-1054, November 27-28, 2013.
- [5] N. Ojaroudi, "Compact UWB monopole antenna with enhanced bandwidth using rotated L-shaped slots and parasitic structures," *Microw. Opt. Technol. Lett.*, vol. 56, pp. 175-178, 2014.
- [6] J. Zhang, H. Yang, and H. Liang, "Band-notched split-ring resonators loaded monopole antenna for ultra-wideband applications," *Applied Computational Electromagnetics Society (ACES) Journal*, vol. 28, pp. 137-142, 2013.
- [7] N. Ojaroudi, "Design of small reconfigurable microstrip antenna for UWB-CR applications," *19th International Symposium on Antenna and Propagation, ISAP2014*, Kaohsiung, Taiwan, December 2-5, 2012.
- [8] N. Ojaroudi, "Application of protruded strip resonators to design an UWB slot antenna with

- WLAN band-notched characteristic,” *Progress in Electromagnetics Research C*, vol. 47, pp. 111-117, 2014.
- [9] N. Ojaroudi, “Small microstrip-fed slot antenna with frequency band-stop function,” *21st Telecommunications Forum, TELFOR 2013*, Belgrade, Serbia, pp. 1047-1050, November 27-28, 2013.
- [10] N. Ojaroudi, “Microstrip monopole antenna with dual band-stop function for UWB applications,” *Microw. Opt. Technol. Lett.*, vol. 56, pp. 818-822, 2014.
- [11] N. Ojaroudi, “Circular microstrip antenna with dual band-stop performance for ultra-wideband systems,” *Microw. Opt. Technol. Lett.*, vol. 56, pp. 2095-2098, 2014.
- [12] “Ansoft high frequency structure simulator (HFSS),” ver. 13, *Ansoft Corporation*, 2010.
- [13] N. Ojaroudi, H. Ojaroudi, and N. Ghadimi, “Quad-band planar inverted-F antenna (pifa) for wireless communication systems,” *Progress In Electromagnetics Research Letters*, vol. 45, 51-56, 2014.
- [14] N. Ojaroudi, “Reconfigurable microstrip-fed monopole antenna for multimode application,” *In Proceedings of the Loughborough Antennas and Propagation Conference (LAPC '14)*, Loughborough, UK, November 10-11, 2014.
- [15] N. Ojaroudi, “Design of microstrip antenna for 2.4/5.8 GHz RFID applications,” *German Microwave Conference, GeMic 2014*, RWTH Aachen University, Germany, March 10-12, 2014.
- [16] N. Ojaroudi, S. Amiri, and F. Geran, “A novel design of reconfigurable monopole antenna for UWB applications,” *Applied Computational Electromagnetics Society (ACES) Journal*, vol. 28, no. 6, pp. 633-639, July 2013.
- [17] N. Ojaroudi, H. Ojaroudi, and Y. Ojaroudi, “Very low profile ultra-wideband microstrip band-stop filter,” *Microw. Opt. Technol. Lett.*, vol. 56, pp. 709-711, 2014.
- [18] N. Ojaroudi, “Design of UWB monopole antenna with dual band-stop characteristic,” *In Proceedings of the Loughborough Antennas and Propagation Conference (LAPC '14)*, Loughborough, UK, November 10-11, 2014.
- [19] N. Ojaroudi, S. Amiri, and F. Geran, “Reconfigurable monopole antenna with controllable band-notched performance for UWB communications,” *20th Telecommunications Forum, TELFOR 2012*, Belgrade, Serbia, pp. 1176-1178, November 20-22, 2012.
- [20] N. Ojaroudi, “An UWB microstrip antenna with dual band-stop performance using a meander-line resonator,” *In Proceedings of the 22nd International Conference on Software, Telecommunications and Computer Networks (SoftCOM)*, Split, Croatia, September 17-19, 2014.
- [21] N. Ojaroudi and N. Ghadimi, “Design of CPW-fed slot antenna for MIMO system applications,” *Microw. Opt. Technol. Lett.*, vol. 56, pp. 1278-1281, 2014.
- [22] N. Ojaroudi and N. Ghadimi, “Dual-band CPW-fed slot antenna for LTE and WiBro applications,” *Microw. Opt. Technol. Lett.*, vol. 56, pp. 1013-1015, 2014.
- [23] Q. X. Chu, C. X. Mao, and H. Zhu, “A compact notched band UWB slot antenna with sharp selectivity and controllable bandwidth,” *IEEE Trans. Antennas Propag.*, vol. 61, 3961-3966, 2013.
- [24] R. Fallahi and A. A. Kalteh, “A novel UWB elliptical slot antenna with band-notched characteristics,” *Progress In Electromagnetics Research, PIER*, vol. 82, pp. 127-136, 2008.
- [25] D. S. Javan, M. A. Salari, and O. H. Ghoochani, “Cross-slot antenna with U-shaped tuning stub for ultra-wideband applications,” *International Journal of Antennas and Propagation*, vol. 2008, doi:10.1155/2008/262981, 2008.
- [26] A. M. Abbosh, “Miniaturized microstrip-fed tapered-slot antenna with ultra-wideband performance,” *IEEE Antennas Wireless Propag. Lett.*, vol. 8, 690-692, 2009.
- [27] X. L. Ma, W. Shao, and G. Q. He, “A novel dual narrow band-notched CPW-fed UWB slot antenna with parasitic strips,” *Applied Computational Electromagnetics Society (ACES) Journal*, vol. 27, pp. 581-586, 2012.
- [28] Y. Li, W. Li, and Q. Ye, “A reconfigurable wide slot antenna integrated with SIRs for UWB/multiband communication applications,” *Microwave Opt. Technol. Lett.*, vol. 55, pp. 52-55, 2013.
- [29] A. Kamalvand, C. Ghobadi, J. Nourina, M. Ojaroudi, and N. Ojaroudi, “Omni-directional/multi-resonance CPW-fed small slot antenna for UWB applications,” *Applied Computational Electromagnetics Society (ACES) Journal*, vol. 28, no. 9, pp. 829-835, 2013.
- [30] A. K. Gautam, S. Yadav, and B. K. Kanaujia, “A CPW-fed compact UWB microstrip antenna,” *IEEE Antennas Wireless Propag. Lett.*, vol. 12, pp. 151-154, 2013.

A Novel Multi-Way Power Divider Design with Enhanced Spurious Suppression

Jiuchao Li, Yuanan Liu, Shulan Li, Cuiping Yu, and Yongle Wu

School of Electronic Engineering
Beijing University of Posts and Telecommunications, Beijing, 100876, China
lijuchao@gmail.com, yuliu@bupt.edu.cn, lishulan@bupt.edu.cn
yucui ping@bupt.edu.cn, wuyongle138@gmail.com

Abstract — In this article, a multi-way Bagley Polygon power divider using a novel technique for enhanced harmonic suppression is presented. In this technique, a T-shaped transmission line with open stub is designed to replace each quarter-wavelength transmission line of the conventional Bagley Polygon power divider. The proposed power divider characterizes arbitrary multi-harmonic suppression in theory, and not only exempt from backside etching or lumped reactive components, but also offering a high level of attenuation over a wide stop band bandwidth. The closed form design equations of the proposed Bagley Polygon power divider have been obtained by rigorous derivation. For verification, a 5-way Bagley Polygon power divider is fabricated and measured. The bandwidth for the suppression of the single third harmonic above 20 dB approximates 37% and enhanced the second-, third-, and fourth-harmonic above 30 dB over 3 GHz at operation frequency of 1.0 GHz.

Index Terms — Bagley Polygon power divider, enhanced spurious suppression, multi-way, T-shaped transmission line.

I. INTRODUCTION

Power dividers are very important for microwave and millimeter-wave systems [1-4], which can be widely used in balanced power amplifier, radar system, feeding networks for antenna arrays, measurement systems, mixers and phase shifters, etc. Bagley Polygon Power Divider (BPPD), using no-lumped elements, such as resistors, can be easily extended to any number of output ports in recent researches [5-7]. In [5], a

general design of compact multi-way power divider similar to BPPD with simple design theory was introduced. In [6], a compact dual-frequency 3-way BPPD using Composite Right/Left Handed (CRLH) transmission lines with shunt connections of open and short stubs for comparison was implemented. A novel design method for a compact BPPD with dual transmission lines is proposed in [7]. Moreover, a loop-type compact 5-way BPPD for dual-band, wide-band operation and easy fabrication was presented in [8]. The main drawback of the conventional BPPD is the presence of spurious response due to the adoption of quarter-wavelength transmission lines as conventional Wilkinson Power Divider (WPD).

Many efforts have been made to overcome spurious response, such as studies on Electromagnetic Band Gap (EBG) cells [9], Defected Ground Structure (DGS) [10], extended line [11], coupled line with DGS and capacitor [12], stubs with inductor [13], and series inductors [14]. However, all of the above-mentioned approaches usually require either backside etching or suppress only single harmonic frequency. Furthermore, other techniques have been used for enhanced harmonic suppression, such as applying anti-coupled line [15], embedded resonators [16], artificial transmission lines and short-circuited LC tank [17], non-uniform transmission transformers [18], and stubs with extended line [19-22]. Recently, a new circuit topology [23] was proposed with harmonic suppression from the 2nd to the 6th by using band-stop filter and extended line. Another design approach is given in [24], capable of harmonic suppression from the 2nd to the 12th harmonic by using low-pass filter and

open stubs. Unfortunately, except for [18], most of these methods were used to suppress harmonic of equal/unequal WPDs, 3-way modified WPD and dual-band WPD.

In this article, a novel circuit topology for enhanced harmonic rejection to the multi-way BPPD is introduced. T-shaped transmission lines are designed to achieve harmonic suppression. For demonstration, the simulated and measured performance of an experimental BPPD operating at a center frequency of 1.0 GHz is shown.

II. STRUCTURES AND THEORY

A. Conventional multi-way BPPD

Conventional multi-way BPPD is illustrated in Fig. 1 (a) [5]. Signals fed on port 1 are equally divided into $2n+1$ part, and the lengths of $\theta_1, \theta_2 \dots \theta_n$ are chosen arbitrarily, which control the phase difference of output ports, here, $n=1, 2, \dots$. Decomposing the symmetry structure, the equivalent circuit can be obtained as depicted in Fig. 1 (b).

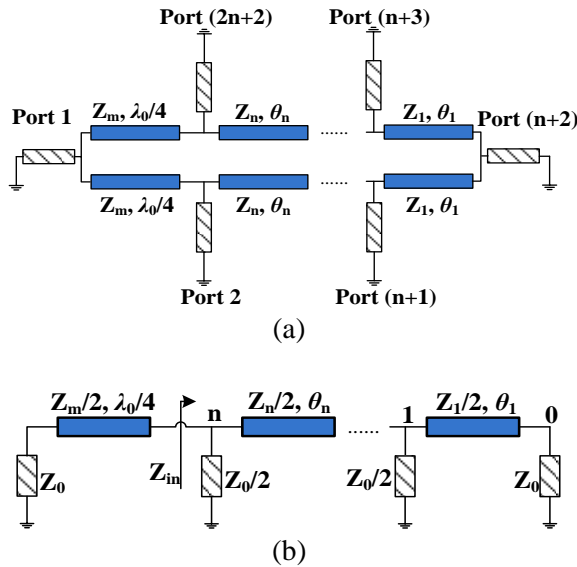


Fig. 1. (a) Conventional $2n+1$ -way BPPD, and (b) equivalent circuit.

To reach the matching goal at the input port, there should be an impedance matching network between Z_n and Z_0 , and $\lambda/4$ transformers are used in the multi-way BPPD. The impedance of ports, Z_0 is usually considered as 50Ω . Obviously, the following relations (1a)-(1c) are obtained from Fig. 1 (b):

$$Z_n = \frac{2Z_0}{2n-1}, \quad (1a)$$

$$Z_{in} = \frac{Z_0}{2n+1}, \quad (1b)$$

$$Z_m = \frac{2Z_0}{\sqrt{2n+1}}. \quad (1c)$$

B. T-shaped transmission line

Figure 2 shows the configuration of the T-shaped transmission line, which consists of two series transmission lines with characteristic impedance of Z_{T1} and one shunt open stub located in the center of the two series transmission lines with characteristic impedance of Z_{T2} ; these three lines have two electrical lengths of θ_1 and θ_2 [25].

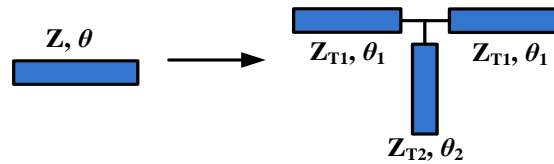


Fig. 2. Configuration of the T-shaped transmission line.

In order to study the T-shaped transmission line model which is equivalent to the conventional transmission line, the $ABCD$ matrix is utilized. The $ABCD$ matrix of the transmission line model is:

$$M = \begin{bmatrix} \cos \theta & jZ \sin \theta \\ j \frac{\sin \theta}{Z} & \cos \theta \end{bmatrix}. \quad (2)$$

The $ABCD$ matrix of the T-shaped transmission line model is

$$M_T = M_{T1} \cdot M_{T2} \cdot M_{T1}, \quad (3)$$

where

$$M_{T1} = \begin{bmatrix} \cos \theta_1 & jZ_{T1} \sin \theta_1 \\ j \frac{\sin \theta_1}{Z_{T1}} & \cos \theta_1 \end{bmatrix}, \quad (4)$$

and

$$M_{T2} = \begin{bmatrix} 1 & 0 \\ j \frac{\tan \theta_2}{Z_{T2}} & 1 \end{bmatrix}. \quad (5)$$

Since the T-shaped transmission line is used to replace the quarter-wavelength connecting line, θ

is assigned to be 90° . Therefore, the **ABCD** matrix of the transmission line becomes (6) and has the following relation (7):

$$M = \begin{bmatrix} 0 & jZ \\ j\frac{1}{Z} & 0 \end{bmatrix}, \quad (6)$$

$$M = M_T. \quad (7)$$

To further simplify the equations (3)-(7), we can easily find the relations as below:

$$Z_{T1} = Z \tan \theta_1, \quad (8)$$

$$Z_{T2} = Z \frac{\cos^2 \theta_1 \cdot \tan \theta_2}{1 - 2 \sin^2 \theta_1}. \quad (9)$$

C. Multi-way enhanced harmonic suppressed BPPD

To suppress the harmonics, the T-shaped transmission line is used to match between Z_0 and Z_{in} , and impedances Z_i ($i=1,2,3\dots n$) can be achieved by the cascade of T-shaped transmission lines. Accordingly, the geometry of the proposed $2n+1$ -way BPPD is drawn in Fig. 3, in which the characteristic impedances and electrical lengths are also defined; the following relationships (10) of the parameters are obtained based on (1a)-(1c), (8) and (9). We need to indicate that once the θ_{Tp} is obtained, the Z_{Tp} will be determined like as (10), here, $p=1,2,3\dots$:

$$Z_{Tm1} = \frac{2Z_0}{\sqrt{2n+1}} \cot \theta_{m1}, \quad (10a)$$

$$Z_{Tm2} = \frac{2Z_0}{\sqrt{2n+1}} \cdot \frac{\cos^2 \theta_{m1} \cdot \tan \theta_{m2}}{1 - 2 \sin^2 \theta_{m1}}, \quad (10b)$$

$$Z_{T3} = \frac{2Z_0}{2n-1} \cot \theta_{T3}, \quad (10c)$$

$$Z_{T4} = \frac{2Z_0}{2n-1} \cdot \frac{\cos^2 \theta_{T3} \cdot \tan \theta_{T4}}{1 - 2 \sin^2 \theta_{T3}}, \quad (10d)$$

$$Z_{T1} = \frac{2Z_0}{2n-1} \cot \theta_{T1}, \quad (10e)$$

$$Z_{T2} = \frac{2Z_0}{2n-1} \cdot \frac{\cos^2 \theta_{T1} \cdot \tan \theta_{T2}}{1 - 2 \sin^2 \theta_{T1}}. \quad (10f)$$

Therefore, the procedure to design the multi-way enhanced harmonic suppression BPPD is briefly summarized as follows:

- (1) According to the practical requirements, the n and p are determined, due to the arbitrary electrical lengths of Z_i , the arbitrary enhanced

- harmonic suppression can be achieved by multiple different T-shaped transmission lines;
- (2) Determine requisite characteristic impedances from (1a)-(1c) and (10a)-(10f);
- (3) According to suppression of the harmonic frequencies, chose θ_{m1} , θ_{m2} , θ_1 , θ_{T1} , $\theta_{T2}\dots$ carefully to make engineering tradeoff between easy fabrication and compact circuit.

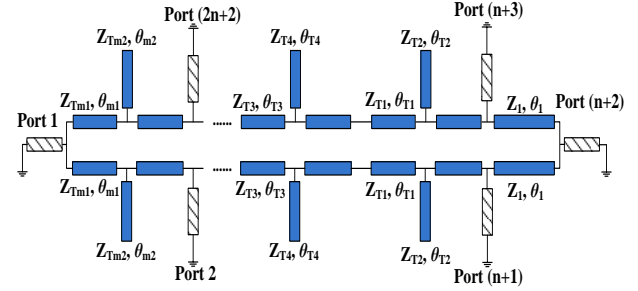


Fig. 3. Configurations of the proposed harmonic suppressed BPPD.

III. SIMULATION AND EXPERIMENT

To certify this proposed structure, we take the 5-way BPPD as an example ($n=2$). In order to achieve a compact T-shaped transmission line in Fig. 2, θ_1 should be less than 45° , the electrical length of the stub segment can be fixed to $\theta_2 = \pi/(2q)$ by the desired q th harmonic suppression ($q=1,2\dots$). For example, an electrical length θ_2 of 45° , 30° or 22.5° correspond to the second-, third-, or fourth-harmonic suppression, respectively. Assuming $Z_0=50 \Omega$, Fig. 4 (a) plots the values of Z_{Tm1} , Z_{Tm2} versus θ_{m1} ($5^\circ \leq \theta_{m1} < 45^\circ$) with θ_{m2} of 45° , 30° or 22.5° , and Fig. 4 (b) plots the values of Z_{T1} , Z_{T2} versus θ_{T1} ($5^\circ \leq \theta_{T1} < 45^\circ$) with θ_{T2} of 45° , 30° or 22.5° , respectively.

The design for the T-shaped transmission line with open stub is essential for a compact BPPD with desired harmonic suppression. For appropriate characteristic impedances and easy fabrication in engineering, we choose $\theta_{m1} = \theta_{T1} = \theta_{T3} = 30^\circ$, the impedances Z_{Tm1} , Z_{Tm2} , Z_{T1} , Z_{T2} , Z_{T3} , Z_{T4} and Z_1 between 20Ω and 100Ω can be easily determined according to the Fig. 4 or analytical design equations (1a)-(1c) and (10a)-(10f). Since θ_i can freely control the phase difference from output ports, θ_1 is chosen as 30° manually, the detailed design parameters are listed in Table 1 based on third-harmonic suppression as an example.

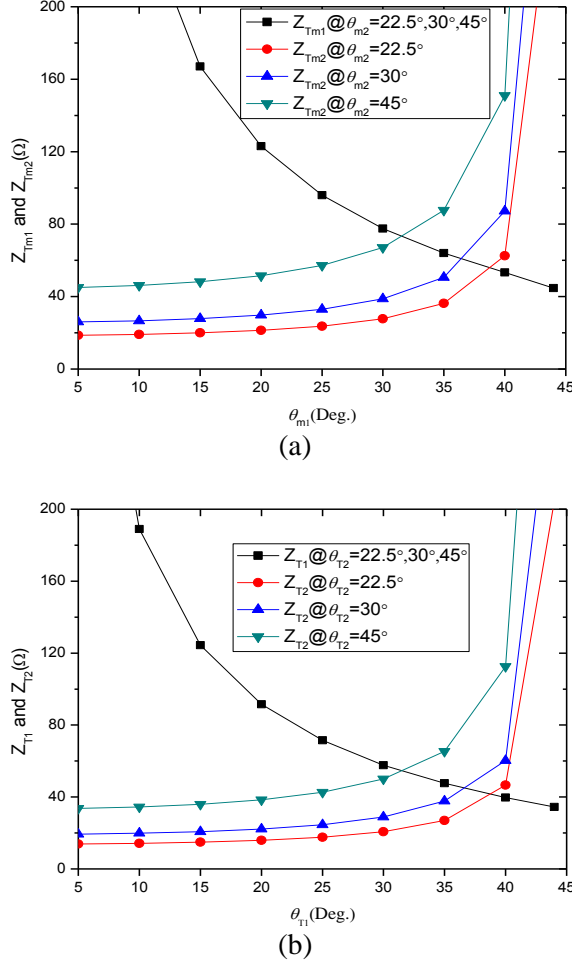


Fig. 4. Design curves for: (a) Z_{Tm1} , Z_{Tm2} versus θ_{m1} , and (b) Z_{T1} , Z_{T2} versus θ_{T1} .

Table 1: Design parameters of the 5-way third harmonic suppression BPPD

| $f_0=1.0$ GHz, $Z_0=50$ Ω , $\theta_{m1}=\theta_{T1}=\theta_{T3}=\theta_1=30^\circ$ | | | |
|--|---------------------------------------|-------------------------|-------------------|
| Case | $\theta_{T2}=\theta_{T4}=\theta_{m2}$ | $Z_{Tm1}(\Omega)$ | $Z_{Tm2}(\Omega)$ |
| | 1 | 30° | 77.5 |
| | $Z_{T1}=Z_{T3}(\Omega)$ | $Z_{T2}=Z_{T4}(\Omega)$ | $Z_1(\Omega)$ |
| | 57.7 | 29 | 100 |

According to these design parameters, the 5-way BPPD third-harmonic suppression is designed and simulated (Case 1), the amplitude responses of S -parameters are shown in Fig. 5. Obviously, ideal return loss of input port and insertion loss are attained, and the BPPD suppression of the third harmonic frequency with a minimum attenuation of 40 dB with S_{21} and S_{61} . The minimum attenuation over 50 dB with 1 GHz bandwidth of

S_{31} , S_{41} and S_{51} . Note that ideal lossless transmission lines are used in simulation.

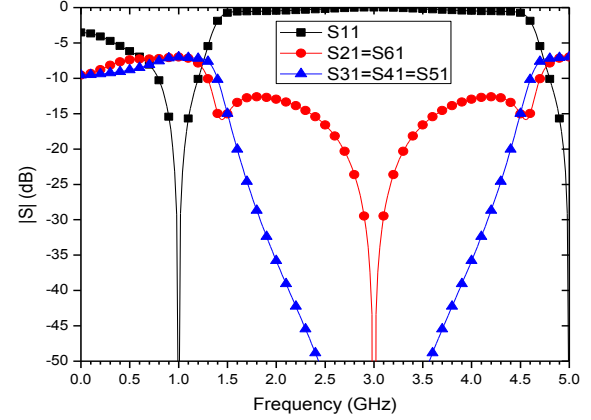


Fig. 5. The amplitude responses S -parameters of 5-way third harmonic suppression BPPD.

To achieve enhanced spurious suppression, we can take the $\theta_g=\pi/(2r)$ as different values ($g=m2$ and $T2, T4\dots$; $r=2,3,4\dots$). Here, θ_1 is chosen as 30° manually, θ_{m2} , θ_{T2} and θ_{T4} is chosen as 45° , 22.5° and 30° , and suppression of the second-, fourth-, and third-harmonic frequency, respectively (Case 2). In order to further validate the proposed BPPD, we utilize three T-shaped transmission lines between the port 2 (6) and port 3 (5), impedances and electrical lengths are named as Z_{T5} , Z_{T6} , θ_{T5} and θ_{T6} , respectively, and suppression of the second-, third-, fourth-, and fifth-harmonic (Case 3). The $Z_{T1}=Z_{T3}=Z_{T5}=57.7$ Ω , and the Z_{Tm1} , Z_{Tm2} , Z_{T2} , Z_{T4} , Z_{T6} and Z_1 can be easily determined according to the analytical above design equations, and the detailed design parameters are listed in Table 2.

According to these design parameters, the 5-way BPPDs (Case 2 and Case 3) with enhanced harmonic suppression are designed and simulated, the amplitude responses of S -parameters are shown in Fig. 6. Obviously, ideal return loss of input port and insertion loss are attained. Figure 6 (a) shows the power divider suppression of the second-harmonic frequency with S_{21} and S_{61} , and suppression of the second-, third- and fourth-harmonic frequencies with S_{31} , S_{41} and S_{51} , simultaneously. Figure 6 (b) shows the power divider suppression of the third harmonic frequency with S_{21} and S_{61} , and suppression of the second-, third-, fourth- and fifth-harmonic

frequencies with S_{31} , S_{41} and S_{51} , simultaneously. So, increase the number of T-shaped transmission lines, the multi-harmonic suppression will be easy to get.

Table 2: Design parameters of the 5-way enhanced harmonic suppression BPPDs.

| $f_0=1$ GHz, $Z_0=50$ Ω , $\theta_{m1}=\theta_{T1}=\theta_{T3}=\theta_{T5}=\theta_1=30^\circ$ | | | | | |
|--|-------------------|---------------|------------------|------------------|-------------------|
| Case 2 | θ_{T2} | θ_{T4} | θ_{T6} | θ_{m2} | $Z_{Tm1}(\Omega)$ |
| | 22.5° | 30° | \ | 45° | 77.5 |
| | $Z_{Tm2}(\Omega)$ | $Z_1(\Omega)$ | $Z_{T2}(\Omega)$ | $Z_{T4}(\Omega)$ | $Z_{T6}(\Omega)$ |
| | 67 | 100 | 20.7 | 29 | \ |
| Case 3 | θ_{T2} | θ_{T4} | θ_{T6} | θ_{m2} | $Z_{Tm1}(\Omega)$ |
| | 22.5° | 45° | 18° | 30° | 77.5 |
| | $Z_{Tm2}(\Omega)$ | $Z_1(\Omega)$ | $Z_{T2}(\Omega)$ | $Z_{T4}(\Omega)$ | $Z_{T6}(\Omega)$ |
| | 38.8 | 100 | 20.7 | 50 | 18.7 |

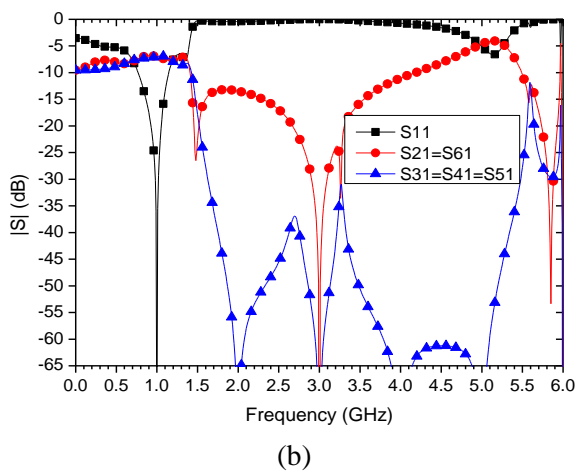
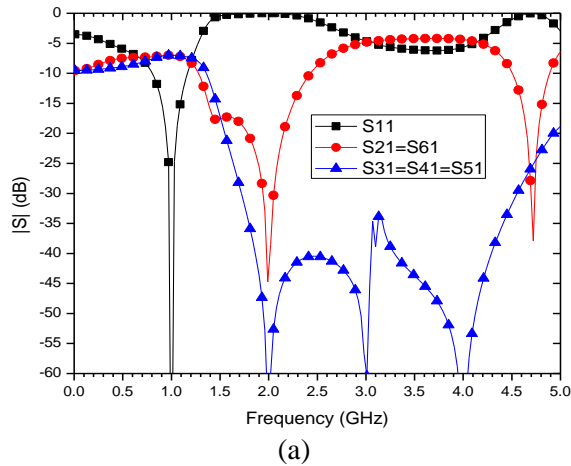


Fig. 6. The amplitude responses S -parameters of 5-way enhanced harmonic suppression BPPDs: (a) Case 2, and (b) Case 3.

For experimental verification, a BPPD designed to operate at 1.0 GHz was prototyped and characterized. This circuit was fabricated on Rogers substrate with a dielectric constant of 3.48 and thickness of 20 mil. Figure 7 shows the top view of the physical layout and the physical dimensions of the circuit whose circuit parameters are obtained from Table 3. All the measured results are shown in Fig. 8, collected from the Agilent N5230C network analyzer over the frequency range from 10 MHz to 5.0 GHz.

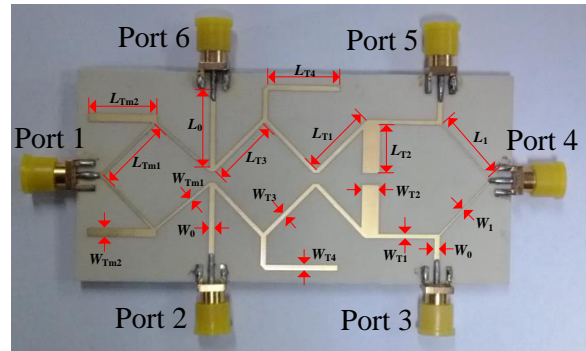


Fig. 7. Photograph of the fabricated proposed BPPD.

Table 3: Physical dimensions of the proposed 5-way BPPD (unit: mil)

| | | | |
|-----------|-----------|-----------|-----------|
| W_{Tm1} | L_{Tm1} | W_{Tm2} | L_{Tm2} |
| 19 | 620 | 65 | 590 |
| W_{T4} | L_{T4} | W_{T3} | L_{T3} |
| 44 | 900 | 35 | 605 |
| W_{T2} | L_{T2} | W_{T1} | L_{T1} |
| 150 | 425 | 35 | 605 |
| W_1 | L_1 | W_0 | L_0 |
| 10 | 633 | 44 | 850 |

The measured S -parameters of the 5-way BPPD show an excellent performance with the return loss of input port, insertion loss, and the suppression of the third harmonic frequency by $S_{21}=S_{61}$, and suppression of the second-, third- and fourth-harmonic frequencies by S_{31} , S_{51} and S_{41} , simultaneously. In particular, Fig. 8 (a) indicates that an octave stop-band bandwidth over 37% (2.62-3.36 GHz) is achieved with a minimum attenuation of 20 dB. The suppression levels, evaluated at the third harmonic frequency (3 GHz), are better than 35 dB. Figure 8 (b) indicates that an octave stop-band bandwidth over 3 GHz

(1.7-4.7 GHz) is achieved with a minimum attenuation of 30 dB. The suppression levels, evaluated at the second-, third-, and fourth-harmonic frequencies (2, 3, and 4 GHz), are better than 50 dB. It is believed that the small

discrepancies between the simulated and measured results were mainly caused by the fabrication tolerances. For comparative purposes, Table 4 gives a brief summary of some previously reported divider topologies.

Table 4: Brief summary of reported power divider designs

| Ref. | Approach | Suppression | Type of Power Divider |
|-----------|--|---|-------------------------------------|
| [9] | Electromagnetic Bandgap (EBG) | $3f_0, 5f_0$ only -32.5 dB @ $3.0f_0$ -12 dB @ $5.0f_0$ | Wilkinson Power Divider (WPD) |
| [10] | Defected Ground Structure (DGS) | $2f_0, 3f_0$ only -26 dB @ $2.0f_0$ -25 dB @ $3.0f_0$ | WPD |
| [11] | Extended line | $3f_0$ only -37 dB @ $3f_0$ | WPD |
| [12] | Coupled line+DGS+capacitor | $3f_0$ only -35 dB @ $3.0f_0$ | WPD |
| [13] | Stubs+inductor | $3f_0$ only -44 dB @ $3f_0$ | WPD |
| [14] | Series inductors | $2f_0, 3f_0, 4f_0$ -28 dB @ $2f_0$ -32 dB @ $3f_0$ -20 dB @ $4f_0$ | Arbitrary power division WPD |
| [15] | Anti-coupled line | $2f_0 \rightarrow 3f_0$ -20 dB @ $2.5f_0$ | WPD |
| [16] | Embedded resonators | $3f_0 \rightarrow 5f_0$ -30 dB @ $4f_0$ | WPD |
| [17] | Artificial transmission lines +Short-circuited LC tank | Broadband harmonic suppression | Dual-band WPD |
| [18] | Non-uniform transmission line transformers | Odd harmonics only | Bagley Polygon Power Divider (BPPD) |
| [19] | Single stub+extended line | $2f_0 \rightarrow 3f_0$ -30 dB @ $2.5f_0$ | WPD |
| [20] | Stubs+extended line | $2f_0 \rightarrow 4f_0$ -25 dB @ $2.5f_0$ -30 dB @ $3.5f_0$ | WPD |
| [21] | Single stub+extended line | $2f_0, 3f_0$ only -35 dB @ $2.0f_0$ -40 dB @ $3.0f_0$ | Unequal WPD |
| [22] | Stubs+extended line | $2f_0 \rightarrow 4f_0$ -25 dB @ $2.5f_0$ -27 dB @ $3.5f_0$ | 3-way modified WPD |
| [23] | Bandstop filter+extended line | Broadband harmonic suppression $2f_0 \rightarrow 6f_0$ | WPD |
| [24] | Low-pass filter+stubs | $2f_0 \rightarrow 12f_0$ | WPD |
| This work | T-shaped transmission line | Arbitrarily enhanced harmonic suppression | Multi-way BPPD |

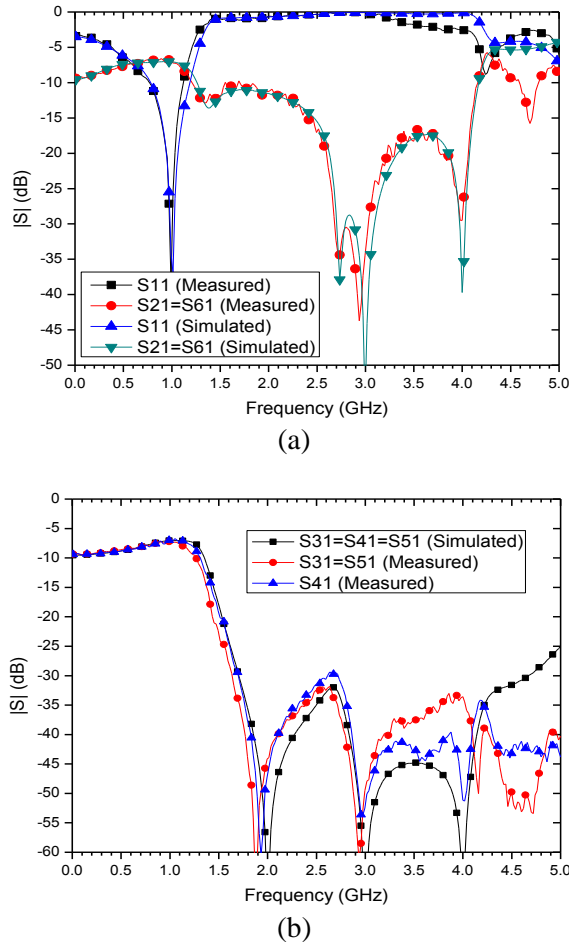


Fig. 8. Measured and simulated: (a) Port 2 and Port 6 have third harmonic suppression, and (b) Port 3, Port 4 and Port 5 have second, third and fourth enhanced harmonic suppression simultaneously.

IV. CONCLUSION

The design and implementation of a novel multi-way BPPD with enhanced harmonic suppression using T-shaped transmission lines has been described. The proposed power divider not only has the advantage of no backside etching or lumped reactive components, but also offers a high level of attenuation over a wide stop band bandwidth. Furthermore, the symmetric output ports with the same phase, by adjusting electrical length between the output ports, can arbitrarily adjust the phase difference asymmetric output ports. Finally, the design concept is validated through simulation and experiment. A fabricated 5-way BPPD shows an excellent performance with the return loss of input port, insertion loss,

and suppression of enhanced the second-, third-, and fourth-harmonic. Actually, this proposed power divider can be easily realized on the planar PCB procedure and MMIC, and very suitable for microstrip circuit implementation in balanced power amplifier, Doherty power amplifier and feeding network for antenna array etc.

ACKNOWLEDGMENT

This work was supported in part by National Natural Science Foundation of China (No. 61001060, No. 61201025 and No. 61201027), BUPT Excellent Ph.D. Students Foundation (No. CX201214), and Fundamental Research Funds for Central Universities (No. 2012RC0301).

REFERENCES

- [1] E. Wilkinson, "An N-way hybrid power divider," *IRE Trans. Microwave Theory Techn.*, vol. 8, no. 1, pp. 116-118, 1960.
- [2] M. Hayati, S. Roshani, and S. Roshani, "Miniaturized wilkinson power divider with nth harmonic suppression using front coupled tapered CMRC," *Applied Computational Electromagnetics Society (ACES) Journal*, vol. 28, no. 3, pp. 221-227, 2013.
- [3] D. Hawatmeh, K. A. Shamaileh, and N. Dib, "Design and analysis of multi-frequency unequal split wilkinson power divider using non-uniform transmission lines," *Applied Computational Electromagnetics Society (ACES) Journal*, vol. 27, no. 3, pp. 248-255, 2012.
- [4] K. A. Shamaileh, A. Qaroot, N. Dib, and A. Sheta, "Design of miniaturized unequal split wilkinson power divider with harmonics suppression using non-uniform transmission lines," *Applied Computational Electromagnetics Society (ACES) Journal*, vol. 26, no. 6, pp. 530-538, 2011.
- [5] I. Sakagami, T. Wuren, M. Fujii, and Tahara M, "Compact multi-way power dividers similar to the bagley polygon," *IEEE MTT-S Int. Microw. Symp. Dig.*, Boston, pp. 419-422, June 2007.
- [6] D. Elles and Y. K. Yoon, "Compact dual band three way bagley polygon power divider using composite right/left handed (CRLH) transmission lines," *IEEE MTT-S Int. Microw. Symp. Dig.*, Boston, pp. 485-488, June 2009.
- [7] J. Li, Y. Liu, S. Li, C. Yu, and Y. Wu, "Miniaturization of microstrip planar bagley polygon power divider with dual transmission lines," *Electron. Lett.*, vol. 49, no. 16, pp. 1015-1016, August 2013.
- [8] I. Sakagami and T. Wuren, "Compact multi-way power dividers for dual-band, wide-band and easy

- fabrication,” *IEEE MTT-S Int. Microw. Symp. Dig.*, Boston, pp. 489-492, June 2009.
- [9] C. Lin, H. Su, J. Chiu, and Y. Wang, “Wilkinson power divider using microstrip EBG cells for the suppression of harmonics,” *IEEE Microw. Wireless Compon. Lett.*, vol. 17, no. 10, pp. 700-702, 2007.
- [10] D. Woo and T. Lee, “Suppression of harmonics in wilkinson power divider using dual-band rejection by asymmetric DGS,” *IEEE Trans. Microwave Theory Tech.*, vol. 53, no. 6, pp. 2139-2144, 2005.
- [11] J. Kim, M. Park, and K. Kong, “Modified design of wilkinson power divider for harmonic suppression,” *Electron. Lett.*, vol. 45, no. 23, pp. 1174-1175, 2009.
- [12] J. Yang, C. Gu, and W. Wu, “Design of novel compact coupled microstrip power divider with harmonic suppression,” *IEEE Microw. Wireless Compon. Lett.*, vol. 18, no. 9, pp. 572-574, 2008.
- [13] K. Yi and B. Kang, “Modified wilkinson power divider for n th harmonic suppression,” *IEEE Microw. Wireless Compon. Lett.*, vol. 13, no. 5, pp. 178-180, 2003.
- [14] R. Mirzavand, M. M. Honari, A. Abdipour, and G. Moradi, “Compact microstrip wilkinson power dividers with harmonic suppression and arbitrary power division ratios,” *IEEE Trans. Microwave Theory Tech.*, vol. 61, no. 1, pp. 61-68, 2013.
- [15] J. Zhang, L. Li, J. Gu, and X. Sun, “Compact and harmonic suppression wilkinson power divider with short circuit anti-coupled line,” *IEEE Microw. Wireless Compon. Lett.*, vol. 17, no. 9, pp. 661-663, 2007.
- [16] J. Wang, J. Ni, Y. Guo, and D. Fang, “Miniaturized microstrip wilkinson power divider with harmonic suppression,” *IEEE Microw. Wireless Compon. Lett.*, vol. 19, no. 7, pp. 440-442, 2009.
- [17] W. Huang, C. Liu, L. Yan, and K. Huang, “A miniaturized dual-band power divider with harmonic suppression for GSM applications,” *J. Electromag. Waves Appl.*, vol. 24, no. 1, pp. 81-91, 2010.
- [18] K. Shamaileh, A. Qaroot, and N. Dib, “Non-uniform transmission line transformers and their application in the design of compact multi-band bagley power dividers with harmonics suppression,” *Prog. Electromagn. Res.*, vol. 113, pp. 269-284, 2011.
- [19] W. Ip and K. K. M. Cheng, “A novel power divider design with enhanced harmonic suppression and simple layout,” *IEEE MTT-S Int. Microw. Symp. Dig.*, Anaheim, CA, pp. 125-128, May 2010.
- [20] K. K. M. Cheng and W. Ip, “A novel power divider design with enhanced spurious suppression and simple structure,” *IEEE Trans. Microwave Theory Tech.*, vol. 58, no. 12, pp. 3903-3908, 2010.
- [21] W. Ip and K. K. M. Cheng, “A novel unequal power divider design with dual-harmonic rejection and simple structure,” *IEEE Microw. Wireless Compon. Lett.*, vol. 21, no. 4, pp. 182-184, 2011.
- [22] W. Ip and K. K. M. Cheng, “A novel 3-way power divider design with multi-harmonic suppression,” *IEEE MTT-S Int. Microw. Symp. Dig.*, Anaheim, CA, pp. 1-4, June 2010.
- [23] N. Yang, B. Li, and X. Wu, “Closed-form design of wilkinson power divider with broadband harmonic suppression and size reduction,” *J. Electromag. Waves Appl.*, vol. 26, no. 2-3, pp. 307-318, 2012.
- [24] M. Hayati, S. Roshani, S. Roshani, and F. Shama, “A novel miniaturized wilkinson power divider with n th harmonic suppression,” *J. Electromag. Waves Appl.*, vol. 27, no. 6, pp. 726-735, 2013.
- [25] W. Tu and K. Chang, “Compact second harmonic-suppressed bandstop and bandpass filters using open stubs,” *IEEE Trans. Microwave Theory Tech.*, vol. 54, no. 6, pp. 2497-2502, 2006.



Jiuchao Li was born in Henan, China, in 1985. He received his M. Eng. degree in Communication and Information System from Liaoning Technical University, Huludao, China, in 2011, and is currently working towards his Ph.D. degree at the Beijing University of Posts and Telecommunications. He was the recipient of the Best Master's Thesis Award of Liaoning Province in 2011. His research interests include microwave systems, antenna design, and dual-band components design.



Yuanan Liu received his B. E., M. Eng., and Ph.D. degrees in Electrical Engineering from the University of Electronic Science and Technology of China, Chengdu, China, in 1984, 1989 and 1992, respectively. In 1984, he joined the 26th Institute of Electronic Ministry of China to develop the Inertia Navigating System. From July 1997, as a Professor, he is with Wireless Communication Center of College of Telecommunication Engineering, BUPT, Beijing, China, where he is involved in the development of next-generation cellular system, wireless LAN, Bluetooth application for data transmission, EMC

design strategies for high speed digital system, and EMI and EMS measuring sites with low cost and high performance. He is interested in smart antenna for high capacity mobile, signal processing techniques in fading environments, EMC for high speed digital system, ISI suppression, OFDM and multicarrier system design. He is a senior member of Electronic Institute of China and a member of IEEE.



Shulan Li was born in Sichuan, China, in 1976. She received her Ph.D. degree at Beijing University of Posts and Telecommunications, Beijing, China, in 2005. She is currently an Associate Professor at the School of Electronic Engineering in BUPT. Her research interests include EMC, antenna design, and dual-band components design.



Cuiping Yu was born in Liaoning, China, in 1983. She received her Ph.D. degree at Beijing University of Posts and Telecommunications, Beijing, China, in 2010. In 2010, she joined the BUPT and became a Lecturer in the School of Electronic Engineering in BUPT.

Her research interests include nonlinear modeling, linearization of wideband transmitters/power amplifiers, high efficiency power amplifiers design, and dual-band components design.



Yongle Wu was born in Hunan, China, in 1983. He received his Ph.D. degree at Beijing University of Posts and Telecommunications, Beijing, China, in 2011. During April to October in 2010, he was a Research Assistant with the City University of Hong Kong, Kowloon, Hong Kong. In 2011, he joined the BUPT and became a Lecturer in the School of Electronic Engineering in BUPT. His research interests include generalized Smith charts, generalized transmission lines, microstrip antenna design, and dual-frequency components design.

On the Attenuation of the Perfectly Matched Layer in Electromagnetic Scattering Problems with the Spectral Element Method

I. Mahariq^{1,3}, M. Kuzuoğlu², and I. H. Tarman³

¹Department of Electrical and Electronics Engineering
TOBB University of Economics and Technology, Ankara 06560, Turkey
ibmahariq@gmail.com

²Department of Electrical and Electronics Engineering

³Department of Engineering Sciences
Middle East Technical University, Ankara 06531, Turkey
kuzuoglu@metu.edu.tr, tarman@metu.edu.tr

Abstract — Although Spectral Element Method (SEM) has been applied in the modeling of boundary value problems of electromagnetics, its usage is not as common as the Finite Element or Finite Difference approaches in this area. It is well-known that the Perfectly Matched Layer (PML) approach is a mesh/grid truncation method in scattering or radiation applications where the spatial domain is unbounded. In this paper, the PML approach in the SEM context is investigated in two-dimensional, frequency-domain scattering problems. The main aim of this paper is to provide the PML parameters for obtaining an optimum amount of attenuation in the scattered field per wavelength in the PML region for Legendre-Gauss-Lobatto grids. This approach is extended to the analysis of SEM accuracy in scattering by electrically large objects by taking the free space Green's function as the building block of the scattered field. Numerical results presented in this work demonstrate the ability of achieving a high degree of accuracy of SEM as compared to other finite methods, as well as the successful applicability of the PML in electromagnetic scattering problems in terms of the optimum attenuation factors provided in this work.

Index Terms — Attenuation, electromagnetic scattering, Green's function, Legendre polynomials, perfectly matched layer, spectral

element method.

I. INTRODUCTION

The well-known Perfectly Matched Layer (PML) approach, (with its possible realizations; the split-field formulation [1], the anisotropic realization [2], and the bianisotropic realization [3]), showed superiority over Absorbing Boundary Conditions (ABCs) when imposed to truncate computational domains in the numerical modeling of electromagnetic radiation and/or scattering problems [4]. The most commonly used numerical methods, namely Finite Element Method (FEM) and Finite Difference Method (FDM), have been extensively applied and investigated in electromagnetic scattering problems where PML is utilized for mesh truncation. Spectral Element Method (SEM) on the other hand, has not been used in this field as much as finite element or finite difference methods.

SEM can be considered as a generalization of FEM with special choice of nodal points and quadrature integration points. It is the high degree of accuracy, the lower CPU time and memory requirement, when compared with other numerical methods, that makes it worthy to use SEM in electromagnetic scattering [5,6,7,8]. These attractive features of SEM are the outcomes of introducing higher degree basis functions that results in having the minimal number of

unknowns; and consequently, the computational cost is much reduced at the same accuracy.

The main goal of this paper is the investigation of the optimal choice of the PML attenuation factor in two-dimensional scattering problems governed by Helmholtz equation. This formulation yields a mathematical model for electromagnetic (transverse electric or magnetic) and acoustic scattering problems. In FEM or FDM approaches, the PML may include several elements/grid points. In this case, the choice of the attenuation factor depends on the thickness of the PML, as well as the density of the nodes/grid points in the layer. Numerical experiments have demonstrated that the PML thickness must be about one wavelength, and the number of nodes/grid points in the longitudinal direction must be 15 to 20 to represent the exponential decay adequately. In the context of SEM, no such analysis has been carried out in the literature. The interest for such an analysis arises from two facts; first, the distribution of grid points in SEM is standard (consider Legendre-Gauss-Lobatto grids), while in FEM or FDM is not. The regularity in the elements corresponding to PML region is another important point. In this paper, the PML region is constructed as a single layer of SEM elements with dimensions equal to a wavelength. Under this restriction, the optimal choice of the attenuation factor is carried out via numerical experiments. Next, the chosen values of the attenuation factor are used to study the accuracy of SEM when applied in scattering problems by large objects.

The paper is arranged as follows: in Section II, the formulation of PML approach in 2D frequency domain scattering problems is presented. In Section III, the approximation of Helmholtz equation by SEM with PML, is given. Section IV demonstrates the numerical results, and finally some conclusions are presented in Section V.

II. PML FORMULATION IN 2D SCATTERING PROBLEMS

In the following, y axis (i.e.: $x=0$) is taken as the interface between Ω and Ω_{PML} , which stand for free space and PML regions, respectively, as depicted in Fig. 1. $\Omega=\{(x,y)/x<0\}$, $\Omega_{PML}=\{(x,y)/x>0\}$. A plane wave (with suppressed time dependence $\exp(j\omega t)$) incident to the interface can be expressed as:

$$u(x, y) = e^{-jk(\cos\theta x + \sin\theta y)}, \quad (1)$$

in which $u(x,y)$ is the scalar field at the point (x,y) , θ is the incident angle (angle between the direction of propagation of the plane wave and x -axis), and k is defined as:

$$k = \frac{2\pi}{\lambda}, \quad (2)$$

which is called the wave number, with λ being the wavelength. As pointed out in [4], in order to provide the attenuation required in domain truncation, one needs to multiply the wave in the PML region by a function $f(x)$ satisfying two properties: $f(0)=1$, and $f(x)$ decreases monotonically for $x>0$. For instance, $f(x)$ can be chosen as:

$$f(x) = e^{-\alpha \cos\theta x}. \quad (3)$$

The scalar field in Ω_{PML} then takes the form:

$$u(x, y) = e^{-jk(a\cos\theta x + \sin\theta y)}, \quad (4)$$

where

$$a = 1 + \frac{\alpha}{jk}, \quad (5)$$

and α is a positive real constant (called the attenuation factor). By direct differentiation, we obtain the following partial differential equation satisfied by the field:

$$\frac{1}{a^2} \frac{\partial^2 u}{\partial x^2} + \frac{\partial^2 u}{\partial y^2} + k^2 u = 0. \quad (6)$$

It is obvious that from the first property of $f(x)$, the continuity condition at the interface holds:

$$u|_{-0} = u|_{+0}. \quad (7)$$

The second condition can be directly derived from (1) and (4) as:

$$\left. \frac{\partial u}{\partial x} \right|_{-0} = \frac{1}{a} \left. \frac{\partial u}{\partial x} \right|_{+0}. \quad (8)$$

While applying integration by parts, the second condition is automatically satisfied if Helmholtz equation in PML region is rewritten as:

$$\frac{1}{a} \frac{\partial^2 u}{\partial x^2} + a \frac{\partial^2 u}{\partial y^2} + a k^2 u = 0. \quad (9)$$

It can easily be shown that for a horizontal interface (i.e.: $y=0$) the following equation is obtained (while keeping PML thickness the same; i.e., the same attenuation factor, α):

$$\frac{\partial^2 u}{\partial x^2} + \frac{1}{a^2} \frac{\partial^2 u}{\partial y^2} + k^2 u = 0. \quad (10)$$

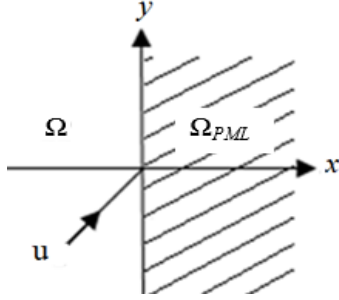


Fig. 1. The interface between Ω and Ω_{PML} .

And finally for a corner region, which is the intersection of vertical and horizontal PML regions, the attenuation is applied in both directions [4], and the following partial differential equation is obtained (see Fig. 2):

$$\frac{1}{a^2} \frac{\partial^2 \mathbf{u}}{\partial x^2} + \frac{1}{a^2} \frac{\partial^2 \mathbf{u}}{\partial y^2} + k^2 \mathbf{u} = 0, \quad (11)$$

or:

$$\frac{\partial^2 \mathbf{u}}{\partial x^2} + \frac{\partial^2 \mathbf{u}}{\partial y^2} + a^2 k^2 \mathbf{u} = 0. \quad (12)$$

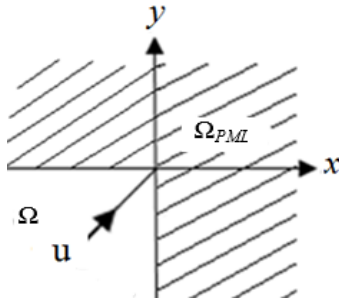


Fig. 2. The corner interface between Ω and Ω_{PML} .

Ideally, the attenuation factor (α) must be infinitely large to make sure that the field magnitude is immediately forced to zero in the PML region. However, in numerical applications, the PML must be terminated by an outer boundary and one must search for the optimum PML thickness, discretization (i.e.: mesh/grid density especially in the longitudinal direction), and α , in order to represent the field decay as smoothly as possible without causing “numerical” reflections. In other words, there is a tradeoff in the choice of the attenuation factor in having almost zero Dirichlet boundary condition on the outer PML boundary and providing the adequate rate of

attenuation within PML for a specific mesh/grid.

III. SEM FORMULATION OF HELMHOLTZ EQUATION

In scattering problems governed by Helmholtz equation, Sommerfeld radiation condition is satisfied:

$$\lim_{|r| \rightarrow \infty} \sqrt{|r|} \left(\frac{\partial \mathbf{u}}{\partial \mathbf{n}} - jk\mathbf{u} \right) = 0, \quad (13)$$

where r is the radiation direction. However, it is hard to apply this condition in SEM. Therefore, we use PML to truncate the computational domain. Based on the PML formulation given in Section II, and as seen from Fig. 4, the problem is defined as:

$$\nabla \Lambda \nabla \mathbf{u} + a k^2 \mathbf{u} = 0, \quad (14a)$$

for $\mathbf{x} = (x, y) \in \Omega \subset \mathbb{R}^2$ subject to the boundary conditions:

$$\mathbf{u}|_{\partial\Omega_D} = f, \quad \frac{\partial}{\partial \mathbf{n}} \mathbf{u}|_{\partial\Omega_N} = g, \quad (14b)$$

on the boundary $\partial\Omega = \partial\Omega_D \cup \partial\Omega_N$. Λ is a tensor defined as:

$$\Lambda = \begin{bmatrix} \Lambda_{11} & 0 \\ 0 & \Lambda_{22} \end{bmatrix}, \quad (14c)$$

where

$$\begin{bmatrix} \Lambda_{11} & \Lambda_{22} \end{bmatrix} = \begin{bmatrix} \frac{1}{a} & a \end{bmatrix} \text{ for x-decay,}$$

$$\begin{bmatrix} \Lambda_{11} & \Lambda_{22} \end{bmatrix} = \begin{bmatrix} a & \frac{1}{a} \end{bmatrix} \text{ for y-decay,}$$

$$\begin{bmatrix} \Lambda_{11} & \Lambda_{22} \end{bmatrix} = \begin{bmatrix} \frac{1}{a} & \frac{1}{a} \end{bmatrix} \text{ for a corner region,}$$

and $a = 1$ for Ω_{FS} .

SEM formulation involves two function spaces, namely, test and trial spaces. An approximate solution to (14) is sought in the trial space:

$$U = \left\{ \mathbf{u} \in \mathbf{H} \mid \mathbf{u}|_{\partial\Omega_D} = f, \quad \frac{\partial}{\partial \mathbf{n}} \mathbf{u}|_{\partial\Omega_N} = g \right\}. \quad (15)$$

The residual resulting from the substitution of the approximate solution from the trial space into (14) vanishes in the process of projection onto the test space:

$$V = \{ \mathbf{v} \in \mathbf{H} \mid \mathbf{v}|_{\partial\Omega_D} = 0 \}. \quad (16)$$

The projection is performed by using the weighted inner product operation:

$$(v, u)_\omega \equiv \int_{\Omega} \omega \bar{v} u \, d\mathbf{x}, \quad (17)$$

in the Hilbert space H where overbar denotes complex conjugation. The projection procedure:

$$(v, \nabla \Lambda \nabla u + a k^2 u)_\omega = 0, \quad (18)$$

leads to the variational (weak) form:

$$\int_{\Omega} \nabla(\omega \bar{v}) \Lambda \nabla u \, d\mathbf{x} - a k^2 \int_{\Omega} \omega \bar{v} u \, d\mathbf{x} = \int_{\partial\Omega_N} \omega \bar{v} g \, d\mathbf{x}, \quad (19)$$

after integration by parts that introduces the boundary integrals. The trial function is then decomposed as follows:

$$u = u_h + u_b \text{ where } u_h|_{\partial\Omega_D} = 0, \text{ and } u_b|_{\partial\Omega_D} = f, \quad (20)$$

resulting in:

$$\begin{aligned} & \int_{\Omega} \nabla(\omega \bar{v}) \Lambda \nabla u_h \, d\mathbf{x} - a k^2 \int_{\Omega} \omega \bar{v} u_h \, d\mathbf{x} = - \\ & \int_{\Omega} \nabla(\omega \bar{v}) \Lambda \nabla u_b \, d\mathbf{x} + a k^2 \int_{\Omega} \omega \bar{v} u_b \, d\mathbf{x} - \int_{\partial\Omega_N} \omega \bar{v} g \, d\mathbf{x}, \quad (21) \end{aligned}$$

after substitution into (19). The boundary conditions are now in place in the variational form with the introduction of the particular solution u_b satisfying the nonhomogeneous Dirichlet boundary condition. Adapting the formulation to arbitrary domain geometry is achieved in two steps. The first step involves partitioning of the domain into mutually disjoint elements:

$$\Omega = \Omega^1 \cup \dots \cup \Omega^e \dots \cup \Omega^M = \bigcup_{e=1}^M \Omega^e. \quad (22)$$

A typical integral in the variational form then becomes:

$$\int_{\Omega} \omega \bar{v} u_h \, d\mathbf{x} = \sum_{e=1}^M \int_{\Omega^e} \omega \bar{v} u_h \, d\mathbf{x}, \quad (23)$$

due to the linearity of integration operation. The second step is the introduction of the standard square element:

$$\Omega^{\text{std}} = \{(\xi, \eta) \in \mathbb{R}^2 \mid -1 \leq \xi \leq 1, -1 \leq \eta \leq 1\}, \quad (24)$$

that will standardize and facilitate the integral operations over a general quadrilateral element Ω^e with curved sides through mapping:

$$\mathbf{x} = \chi_1^e(\xi, \eta), \quad \mathbf{y} = \chi_2^e(\xi, \eta). \quad (25)$$

The operations can then be converted using the rules:

$$\begin{bmatrix} d\mathbf{x} \\ d\mathbf{y} \end{bmatrix} = \underbrace{\begin{bmatrix} \frac{\partial \chi_1^e}{\partial \xi} & \frac{\partial \chi_1^e}{\partial \eta} \\ \frac{\partial \chi_2^e}{\partial \xi} & \frac{\partial \chi_2^e}{\partial \eta} \end{bmatrix}}_{\mathbf{J}} \begin{bmatrix} d\xi \\ d\eta \end{bmatrix},$$

$$\nabla = \begin{bmatrix} \frac{\partial}{\partial \mathbf{x}} \\ \frac{\partial}{\partial \mathbf{y}} \end{bmatrix} = \frac{1}{|\mathbf{J}|} \begin{bmatrix} \frac{\partial \chi_1^e}{\partial \eta} & -\frac{\partial \chi_1^e}{\partial \xi} \\ -\frac{\partial \chi_2^e}{\partial \xi} & \frac{\partial \chi_2^e}{\partial \eta} \end{bmatrix} \begin{bmatrix} \frac{\partial}{\partial \xi} \\ \frac{\partial}{\partial \eta} \end{bmatrix}, \quad (26)$$

where $|\mathbf{J}|$ is the determinant of the Jacobian \mathbf{J} .

Numerical implementation of the procedure requires introduction of a spatial discretization that will facilitate the numerical evaluation of the derivatives and the integrals. This is equivalent to taking the trial and test spaces as finite dimensional spaces for which space of polynomials is the convenient choice. Jacobi polynomials as eigenfunctions of singular Sturm-Liouville differential operator provide a good basis for this space [8]. Numerically stable interpolation and highly accurate quadrature integration approximation techniques are provided by nodes and weights associated with Jacobi polynomials. In particular, Legendre polynomials are the convenient choice in that they are orthogonal under the weighted inner product with unity weight $\omega = 1$. The associated roots ζ_m as nodes provide the stable form of interpolation:

$$u(\zeta) = \sum_{m=0}^N u(\zeta_m) L_m(\zeta), \quad (27)$$

where L denotes respective Lagrange interpolants with the typical form

$$L_k(\zeta) = \prod_{\substack{\ell=0 \\ \ell \neq k}}^N \frac{(\zeta - \zeta_\ell)}{(\zeta_k - \zeta_\ell)}, \quad (28)$$

satisfying the cardinality property $L_k(\zeta_\ell) = \delta_{k\ell}$. This in turn provides the means for evaluating the derivatives, say:

$$\frac{d}{d\zeta} u(\zeta) \Big|_{\zeta_k} = \sum_{m=0}^N u(\zeta_m) L'_m(\zeta_k) = \sum_{m=0}^N u(\zeta_m) \underbrace{L'_m(\zeta_k)}_{D_{km}}, \quad (29)$$

where D_{km} is referred to as the differentiation matrix. It also provides Gauss-Legendre-Lobatto (GLL) quadrature:

$$\int_{-1}^1 u(\zeta) d\zeta = \sum_{k=0}^N \varpi_k u(\zeta_k), \quad (30)$$

which is exact for the integrand a polynomial of degree $\leq 2N - 1$. These can easily be extended to two dimensions over the tensor grid (ξ_k, η_l) with the mapping functions $\chi_i(\xi, \eta)$ constructed using the linear blending function approach [9,10].

IV. NUMERICAL RESULTS

A. Optimum attenuation factor

For the numerical experiments, it is assumed that u is known (analytical expression is available). In Fig. 3, on $\partial\Omega_1$ and $\partial\Omega_2$, u is imposed as a Dirichlet boundary condition (this is referred as “Case-a”). In Ω , u satisfies the homogenous Helmholtz equation. The numerical solution by SEM is then found. In Fig. 4, where the computational domain $\Omega = \Omega_{FS} \cup \Omega_{PML}$, u is imposed on $\partial\Omega_1$ only, and on $\partial\Omega_2$ zero Dirichlet boundary condition is simply imposed. This case is referred as “Case-b”, in which both the homogenous Helmholtz equation (governing the free space region, Ω_{FS}), and the PML partial differential equations (governing the PML region, Ω_{PML}) are satisfied. In this way, the SEM error without the PML (Case-a) and the SEM error with the utilization of the PML can be observed.

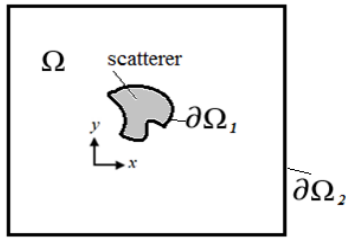


Fig. 3. The computational domain definition without the PML.

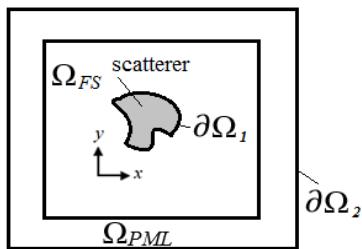


Fig. 4. The computational domain definition with the PML.

For sake of determining the optimum value of α in SEM at a fixed number of points per wavelength in PML region, several problems have been carefully studied. First, we considered the two-dimensional Green’s function that has Helmholtz equation as the governing PDE:

$$\nabla^2 u + k^2 u = -\delta(\vec{r}), \tag{31}$$

where the solution is given in terms of Hankel function of the second kind of order zero as $u(\vec{r}) = (j/4)H_0^{(2)}(k|\vec{r}|)$. To avoid singularity arising from the radiating point source being at the origin, we truncate the domain around the origin, and impose the Dirichlet boundary condition in terms of the field $u(\vec{r})$ over the boundary $\partial\Omega_1$ as shown in Fig. 5 (a). Then, to have a bounded domain, truncation by PML is applied. By utilizing the symmetry, only one-fourth of the computational domain is studied. Zero Dirichlet boundary is imposed on outer boundary of the PML region (i.e.: $\partial\Omega_2$) and zero Neumann symmetry condition is imposed on the boundary $\partial\Omega_N$. The computational domain is subdivided into eight elements as shown in Fig. 5 (b), with dimensions of $\lambda \times \lambda$ and resolution of $N \times N$ for each element. It is worth to point that the maximum incident angle (the angle between the ray and the normal to the free space-PML interface) in this problem is 45° in terms of a ray approximation.

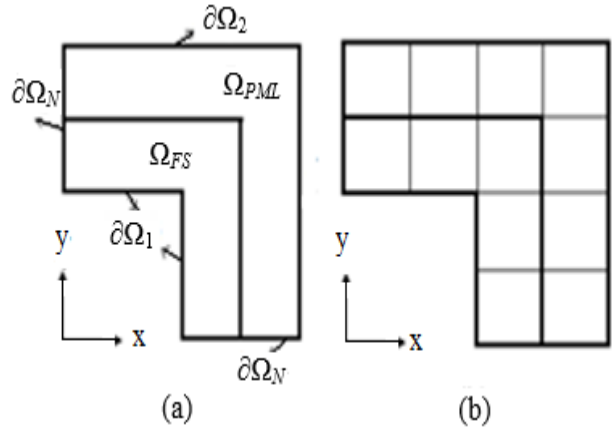


Fig. 5. The problem of the 2D Green’s function: (a) the problem definition, and (b) elements in SEM.

Throughout of this paper, the error measure is defined as:

$$\text{Err} = \max_i \frac{|u_{i,\text{exact}} - u_{i,\text{SEM}}|}{|u_{i,\text{exact}}|}, \quad (32)$$

where $u_{i,\text{exact}}$ and $u_{i,\text{SEM}}$ are the exact solution and the SEM solution, respectively, at the i^{th} node corresponding to the free space region, Ω_{FS} .

Table 1 shows the value of the attenuation factor (α), and the corresponding maximum relative error for each resolution (N). The values of α were well calibrated for each number of points per wavelength (N), such that the minimum possible error is obtained in each case. For instance, at N=11, the variation of against vs. α is presented in Fig. 6.

Table 1: Maximum relative errors obtained by SEM for the problem in Fig. 5

| N | α | Err |
|----|----------|------------|
| 7 | 4.40 | 4.5e-3 |
| 8 | 5.25 | 4.1746e-4 |
| 9 | 6.40 | 4.6100e-5 |
| 10 | 7.18 | 4.6486e-06 |
| 11 | 8.41 | 5.8466e-07 |
| 12 | 9.10 | 8.0365e-08 |
| 13 | 10.40 | 7.9952e-09 |
| 14 | 11.16 | 1.4402e-09 |
| 15 | 12.33 | 1.3769e-10 |
| 16 | 13.18 | 2.6012e-11 |
| 17 | 14.22 | 3.2078e-12 |
| 18 | 15.20 | 4.4765e-13 |

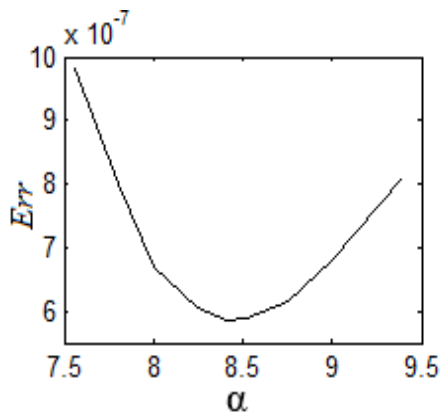


Fig. 6. Variation of SEM error vs. α at N=11.

It is important to check the accuracy of SEM when it is used to solve the 2D Green's function problem again, but this time, on a different computational domain in which the inner boundary is defined to be circular. Because of symmetry (i.e.: when the point source is placed at the origin), only two adjacent quadrants are studied as shown in Fig. 7 (a). Here, the field $u(\vec{r})$ is imposed over the inner boundary $\partial\Omega_1$, zero Dirichlet boundary condition and Neumann boundary condition are imposed on $\partial\Omega_2$ and $\partial\Omega_N$, respectively (Case-b). The chosen elements in SEM are shown in Fig. 7 (b) for convenience.

In "Case-a", simply the domain corresponding to the PML region is considered as free space satisfying the homogenous Helmholtz equation, and the field $u(\vec{r})$ is imposed over both the inner boundary, $\partial\Omega_1$ and the outer boundary, $\partial\Omega_2$. The errors are calculated for the following dimensions: $\lambda=1$, $r_c=b=0.5$, $d=c=1$, and presented in Table 2 for both Case-a and Case-b. It is worth to point that the errors are larger than the ones presented in Table 1. This is due to the fact that we have deformed elements in this problem.

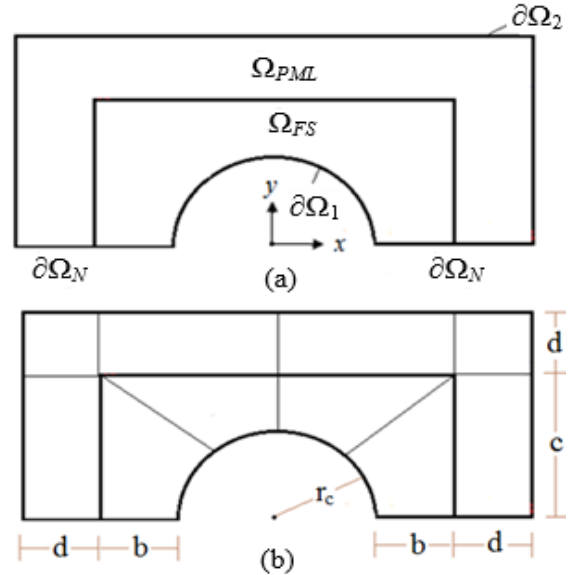


Fig. 7. The problem of the 2D Green's function having a circular inner boundary: (a) the problem definition, and (b) elements in SEM.

Table 2: Maximum relative errors obtained by SEM for the 2D Green's function problem with circular inner boundary

| N | α | Err (Case-a) | Err (Case-b) |
|----|----------|--------------|--------------|
| 7 | 4.40 | 0.003559 | 0.001994 |
| 8 | 5.25 | 0.000382 | 0.000342 |
| 9 | 6.40 | 5.24E-05 | 6.03E-05 |
| 10 | 7.18 | 6.92E-06 | 7.77E-06 |
| 11 | 8.41 | 8.50E-07 | 9.72E-07 |
| 12 | 9.10 | 1.06E-07 | 1.30E-07 |
| 13 | 10.40 | 1.29E-08 | 1.50E-08 |
| 14 | 11.16 | 1.32E-09 | 1.60E-09 |
| 15 | 12.33 | 2.44E-10 | 7.89E-10 |
| 16 | 13.18 | 6.37E-11 | 4.65E-10 |
| 17 | 14.22 | 1.71E-11 | 3.63E-10 |
| 18 | 15.20 | 4.62E-12 | 2.75E-10 |

B. Scattering cylinder

Next, we have studied scattering by a circular cylinder and considered the following incident plane wave on an infinitely long, circular conducting cylinder of radius r_c (see Fig. 8) of the form $\mathbf{u}^i = \mathbf{u}_0 e^{-j\mathbf{k}x}$.

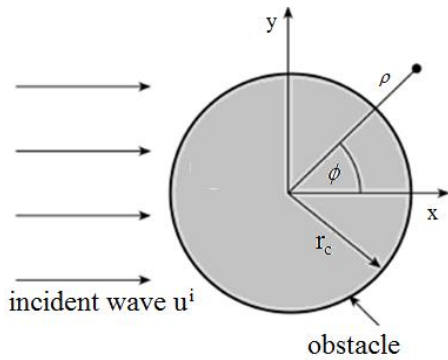


Fig. 8. An incident plane wave to an infinitely-long, circular conducting cylinder.

Because of symmetry in z direction, the problem is a two-dimensional one, and because of symmetry in 2D, only one half of the plane is considered. The scattered field is given analytically in terms of Bessel and Hankel functions as:

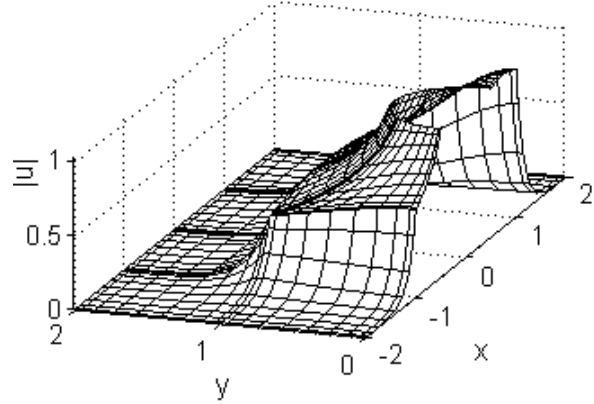
$$\mathbf{u}^s = -\mathbf{u}_0 \sum_{n=-\infty}^{\infty} (-j)^n \frac{J_n(kr_c) H_n^{(2)}(k\rho) e^{jn\phi}}{H_n^{(2)}(kr_c)}. \quad (33)$$

Here, for Case-a, the scattered field given in (33) is imposed on $\partial\Omega_1$ and $\partial\Omega_2$, and for Case-b,

the scattered field given in (33) is imposed on $\partial\Omega_1$ only, and zero Dirichlet boundary condition is imposed on $\partial\Omega_2$. Error results are presented in Table 3. As seen from the table, although we have deformed elements, the values of α still give the best accuracy when compared with the accuracy obtained for Case-a. The magnitude of the solution is shown in Fig. 9 at $N=10$.

Table 3: Maximum relative errors as obtained by SEM for scattering cylinder

| N | α | Err (Case-a) | Err (Case-b) |
|----|----------|--------------|--------------|
| 7 | 4.40 | 0.010563 | 0.00305 |
| 8 | 5.25 | 0.000817 | 0.00044 |
| 9 | 6.40 | 7.74E-05 | 8.02E-05 |
| 10 | 7.18 | 1.48E-05 | 1.63E-05 |
| 11 | 8.41 | 4.46E-06 | 4.51E-06 |
| 12 | 9.10 | 1.18E-06 | 1.18E-06 |
| 13 | 10.40 | 3.74E-07 | 3.80E-07 |
| 14 | 11.16 | 1.24E-07 | 1.27E-07 |
| 15 | 12.33 | 3.92E-08 | 4.78E-08 |
| 16 | 13.18 | 1.22E-08 | 3.22E-08 |
| 17 | 14.22 | 3.78E-09 | 2.64E-08 |
| 18 | 15.20 | 1.17E-09 | 2.21E-08 |


 Fig. 9. Magnitude of the scattered field by the cylinder (i.e.: $|u|$) at $N=10$.

C. Scattering by large objects

To investigate SEM accuracy using the obtained values of α when scattering by large objects is encountered, we considered a square region $6\lambda \times 6\lambda$ (standing for the dimensions of the object) whose boundary is $\partial\Omega_1$ (where the field $\mathbf{u}(\vec{r})$ is imposed) as shown in Fig. 10. Each of the free space region Ω_{FS} , and the PML region Ω_{PML} ,

has a width of λ . The computational domain is subdivided into 64 elements so that each element is of $\lambda \times \lambda$ ($\lambda=1$) and has a resolution of $N \times N$. The point source is chosen to be placed in 21 positions as seen from the right side of Fig. 10. Here, we note that because of symmetry, the average relative error of these selected positions is the same as if 121 positions were chosen and distributed uniformly over the object. In each position, the problem (zero Dirichlet bc. is imposed over $\partial\Omega_2$) is solved and the SEM relative error is calculated (i.e.: Case-b). The magnitude of the field when the point source is at position-16 is shown in Fig. 11 at $N=7$. It should be noted that the maximum incident angle ranges from 45° (for position-1) to 77° (for position-16).

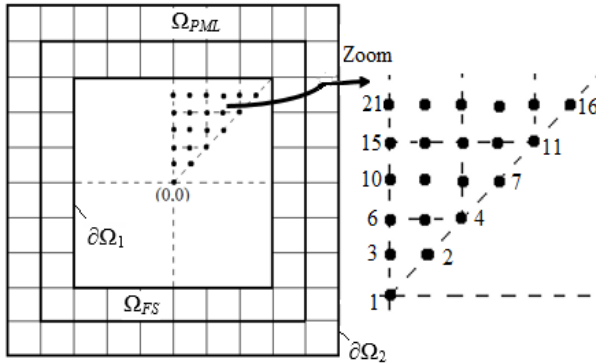


Fig. 10. Scattering by large objects: the computational domain (on the left), selected positions for the point source (on the right).

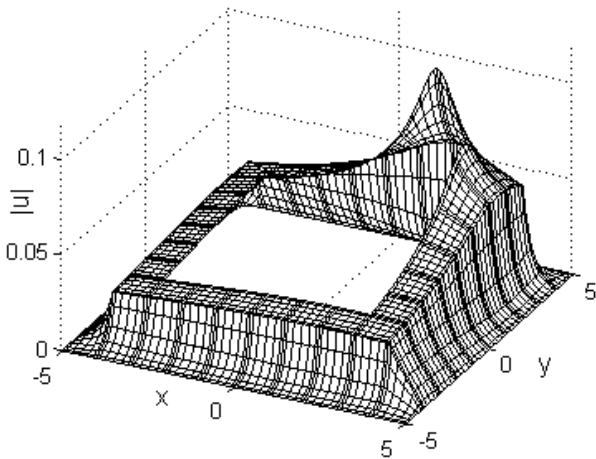


Fig. 11. Plot of $|u|$ for position-16 at $N=7$.

Although the solutions are obtained by changing the position of the point source whose field is governed by (31), taking the average of the maximum relative errors of all position will give an estimate of the accuracy when a dielectric object is involved. This is due to the fact that the error in our work is normalized with the field, and the solution when a dielectric object exists can be expressed as a linear combination of Hankel function of the second kind of order zero. In Table 4, the average of the errors obtained for the 21 positions are presented.

Table 4: The average of relative errors of the 21 positions

| N | α | Average Err |
|----|----------|-------------|
| 7 | 4.40 | 0.006971 |
| 8 | 5.25 | 0.001451 |
| 9 | 6.40 | 3.44E-04 |
| 10 | 7.18 | 1.32E-04 |
| 11 | 8.41 | 2.91E-05 |
| 12 | 9.10 | 1.23E-05 |
| 13 | 10.40 | 2.36E-06 |
| 14 | 11.16 | 8.71E-07 |
| 15 | 12.33 | 1.78E-07 |
| 16 | 13.18 | 7.91E-08 |
| 17 | 14.22 | 2.68E-08 |

D. One-dimensional problem

Finally, we considered Helmholtz equation in one dimension over $x \in [-1-\varepsilon, 1+\varepsilon]$, where ε is a real number chosen as 0.001 to avoid singularity (i.e.: to have the solution: $u = \exp(-jkx)$). The domain is divided into two elements each has N points and a length of $1+\varepsilon$. In the first element ($x \in [-1-\varepsilon, 0]$), the homogeneous Helmholtz equation is satisfied and in the second element (PML), the nonhomogeneous Helmholtz equation is satisfied:

$$\frac{1}{a^2} \frac{\partial^2 u}{\partial x^2} + k^2 u = 0, \text{ for } x \in [0, 1+\varepsilon]. \quad (34)$$

The boundary conditions are $u(-1-\varepsilon) = \exp(-jk(-1-\varepsilon))$ and $u(1+\varepsilon) = 0$. The maximum relative errors corresponding to the first element are presented in Table 5 for unity wavelength. The imaginary parts of the exact and SEM solution are shown in Fig. 12 at $N=18$.

Table 5: The maximum relative error of the one-dimensional problem

| N | α | Err |
|----|----------|------------|
| 7 | 4.40 | 0.0065 |
| 8 | 5.25 | 5.1111e-04 |
| 9 | 6.40 | 6.0577e-05 |
| 10 | 7.18 | 6.0067e-06 |
| 11 | 8.41 | 7.4124e-07 |
| 12 | 9.10 | 7.1254e-08 |
| 13 | 10.40 | 8.7009e-09 |
| 14 | 11.16 | 6.5970e-10 |
| 15 | 12.33 | 1.0664e-10 |
| 16 | 13.18 | 8.8274e-12 |
| 17 | 14.22 | 1.6588e-12 |
| 18 | 15.20 | 2.3845e-13 |

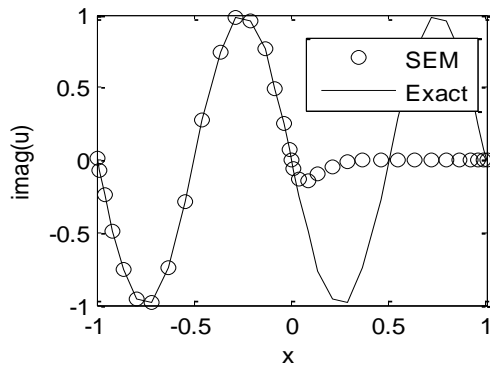


Fig. 12. Imaginary part of the exact and SEM solutions at N=18.

V. CONCLUSION

We have presented in this work the PML formulation for 2D frequency-domain problems and the corresponding SEM formulation taking into account the interface conditions. Based on the numerical results discussed in this paper for different geometries, it is obvious that only one PML layer is required to truncate the computational domain when SEM is used. It is also observed that the provided attenuation factor gives the best accuracy and has almost a linear relationship with the number of points per wavelength (slope ≈ 0.95). In addition, the accuracy of scattering by large objects is estimated. Finally, the optimum values of the attenuation factors are used to check the accuracy of SEM for a one-dimensional problem. In

conclusion, the applicability of PML in electromagnetic scattering problems by using SEM is very successful in terms of the attenuation factors provided in this work.

ACKNOWLEDGMENT

The first author acknowledges the financial support from Technical Research Council of Turkey (TUBITAK).

REFERENCES

- [1] J. P. Berenger, "A perfectly matched layer for the absorption of electromagnetic waves," *Journal of Computational Physics*, vol. 114, pp. 185-200, 1994.
- [2] Z. S. Sacks, D. M. Kingsland, R. Lee, and J. F. Lee, "A perfectly matched anisotropic absorber for use as an absorbing boundary condition," *IEEE Transactions on Antennas Propagation*, vol. 43, pp. 1460-1463, 1995.
- [3] D. H. Werner and R. Mittra, "New field scaling interpretation of berenger's PML and its comparison to other PML formulations," *Microwave and Optical Technology Letters*, vol. 16, pp. 103-106, 1997.
- [4] M. Kuzuoglu and R. Mittra, "A systematic study of perfectly matched absorbers," *Frontiers in Electromagnetics*, IEEE Press, 2000.
- [5] J. Lee, T. Xiao, and Q. H. Liu, "A 3-D spectral-element method using mixed-order curl conforming vector basis functions for electromagnetic fields," *IEEE Trans. On Microwave Theory and Techniques*, vol. 54-1, pp. 437-444, January 2006.
- [6] J. Lee and Q. H. Liu, "A 3-D spectral-element time-domain method for electromagnetic simulation," *IEEE Trans. On Microwave Theory and Techniques*, vol. 55-5, pp. 983-991, May 2007.
- [7] O. Z. Mehdizadeh and M. Paraschivoiu, "Investigation of a two-dimensional spectral element method for helmholtz's equation," *Journal of Computational Phys.*, vol. 189, pp. 111-129, 2003.
- [8] S. J. Hesthaven, S. Gottlieb, and D. Gottlieb, "Spectral methods for time-dependent problems," *Cambridge University Press*, 2007.
- [9] O. Deville, F. P. Fischer, and E. Mund, "High-order methods for incompressible fluid flow," *Cambridge University Press*, vol. 9, 2002.
- [10] J. W. Gordon and A. C. Hall, "Transfinite element methods: blending-function interpolation over arbitrary curved element domains," *Numer. Math.*, vol. 21.2, pp. 109-129, 1973.



Ibrahim Mahariq received his B.Sc. degree from the Department of Electrical and Computer Engineering/Palestine Polytechnic University in 2003. He worked there as Teaching Assistant from 2003-2005. He received his M.Sc. degree in Design of Electrical Machines, and his Ph.D. degree in Computational Electromagnetics from Middle East Technical University, Ankara, Turkey. Mahariq was granted TUBITAK scholarship for his Ph.D. studies in 2010, and is currently working in the Department of Electrical and Electronics Engineering at TOBB ETU for research purposes.



Mustafa Kuzuoglu received his B.Sc., M.Sc., and Ph.D. degrees in Electrical Engineering from Middle East Technical University (METU), Ankara, Turkey, in 1979, 1981, and 1986, respectively. He is currently a Professor with METU. His research interests include computational electromagnetics, inverse problems, and radars.



Hakan I. Tarman received his B.Sc. degree in Mechanical Engineering and Mathematics, and the M.Sc. degree in Mechanical Engineering from Boğaziçi University, İstanbul, Turkey. He received his Ph.D. degree in Applied Mathematics from Brown University, Providence, Rhode Island, USA. He is currently a Professor with the Department of Engineering Sciences, Middle East Technical University, Ankara, Turkey.

A Compact 2-18 GHz Halved Vivaldi Antenna

Ping Wang^{1,2}, Guangjun Wen¹, Yongjun Huang¹, and Haobin Zhang³

¹Centre for RFIC and System Technology
School of Communication and Information Engineering
University of Electronic Science and Technology of China, Chengdu 611731, China
wangpingcqz@163.com

²College of Electronic and Information Engineering
Chongqing Three Gorges University, Chongqing 404000, China

³Science and Technology on Electronic Information Control Laboratory
Chengdu 610036, China

Abstract — A compact, broadband, halved planar Vivaldi antenna has been proposed in this paper. The halved Vivaldi antenna is located on a large metal plane vertically, and connected to the metal plane through feed-line and short-line. The proposed antenna was designed, fabricated, and tested. Experimental and simulated results show that the proposed halved Vivaldi antenna has a wide bandwidth from approximately 1.44 to 18.5 GHz, and a small size of only 30 mm × 60.5 mm. Moreover, the designed antenna can provide excellent characteristics, including directive radiation characteristics and vertically polarized radiation pattern. These results prove that the proposed antenna should be useful in many metal surface-mounted communication systems, such as missile, unmanned aerial vehicles, and the like.

Index Terms — Metal plane, small size, ultra-wide bandwidth antenna, Vivaldi antenna.

I. INTRODUCTION

Tapered Slot Antennas (TSA), as its name suggests, is a class of antenna with tapered radiation slot-line and can be classified into different types according to its tapered curves, such as, linear TSA [1,2], constant width TSA [3], logarithmically TSA [4], exponentially TSA or Vivaldi antenna [5-9], and so on. The Vivaldi Tapered Slot Antenna (TSA) consists of an exponentially tapered slot cut in a metal film (with

or without a thin substrate) on one side of the material, which flares from a small slot (50Ω) to a large opening notch, matching to free space's wave impedance of 377Ω . It is normally fabricated by cutting a narrow slot in continuous metal film and the other end of the slot is connected by a quarter-wave cavity to improve its impedance matching and forward gain. A transmission line is placed on the other side of the substrate, and one end of that is connected with a quarter-wave micro-strip line cross over transition [10], which excites a circular or rectangular cavity on the slot side. The energy from this cavity is transferred to the slot-line taper, and propagating along the slot, radiates in the end-fire direction. To enhance the impedance bandwidths, the quarter-wave micro-strip line is generally replaced by the feed technique of a micro-strip fan-shaped stub [11]. However, a micro-strip fan-shaped stub produces very high radiation loss and even distorts radiation patterns; especially in a high frequency range, which limits its applications in some systems. To reduce the dissipative losses and unwanted radiation from the balun, it is necessary to seek for a new balun and then assemble it with tapered slot. In recent publications, two different planar fourth-order Marchand baluns were introduced [12,13], which reduce the physical size of the balun components and unwanted radiation. However, they have complex structure and narrower impedance bandwidths, and also depend on high permittivity

dielectric. Therefore, simple configuration and wide bandwidth are desirable.

On the other hand, it is commonly known that single Vivaldi antenna works best when it is more than one wavelength long and the height of the antenna aperture is greater than one-half wavelength referring to the lowest resonant frequency [11], which means that the antenna still has large dimension for some limited communication space, so it is a challenging task to minimize the physical size of Vivaldi antenna without simultaneously reducing the bandwidths. In this letter, we present a compact halved Vivaldi antenna. The proposed antenna with a compact size of only $30 \text{ mm} \times 60.5 \text{ mm}$ ($0.144 \lambda_0 \times 0.29 \lambda_0$, where λ_0 is the maximum working wavelength) offers a bandwidth from 1.44 to 18.5 GHz, and also possesses directive radiation patterns and low cross-polarization levels; which is very suitable for mounting on metallic surface of a variety of communication systems. Simulated and measured results show that the antenna has very wide frequency bandwidth, directive radiation patterns, small size and vertically polarized characteristics.

II. ANTENNA CONFIGURATION

The geometrical configuration of the proposed antenna is shown in Fig. 1. The antenna has a double-layer metallic structure and is printed on a substrate of thickness of 0.5 mm, with the dielectric constant of 3.55. In order to reduce the size and increase the bandwidth of the antenna, a resistor of $R=100 \ \Omega$ is integrated at the slot-line end of the proposed antenna. A $50 \ \Omega$ SMA connector is used as the feed source, whose inner conductor is directly soldered to one end of the feed-line, and the outer conductor is connected directly to the metal plane. In this design, the other end of feed-line is shorted to the metal surface of the antenna by metalized vias. The outer edge and inner edge taper of the proposed antenna are described by the mathematical exponential functions, which are defined as:

$$\begin{aligned} x_i &= c_1 \exp(R_1 z) + c_2, \\ x_o &= \exp(R_2 z \wedge sf) + c_3, \end{aligned} \quad (1)$$

where $c_1=(2w_1-w_0)/(2(\exp(R_1 L_1)-1))$, $R_1=0.07$, $c_2=(w_0 \exp(R_1 L_1)-2w_1)/(2(\exp(R_1 L_1)-1))$, $sf=1.65$, $c_3=(c_1 \exp(R_1 L_1)+c_2)+m-m_1$, $R_2=0.06$, x_i and x_o denote the distances from the slot center line to the inner and outer edges, respectively. Thus, the end-

point z -value of the outer exponential curve (P) can be expressed as:

$$P = \left(\ln \frac{c_1 \exp(R_1 L_1) + c_2 + m + 1 - c_3}{R_2} \right) \wedge \left(\frac{1}{sf} \right). \quad (2)$$

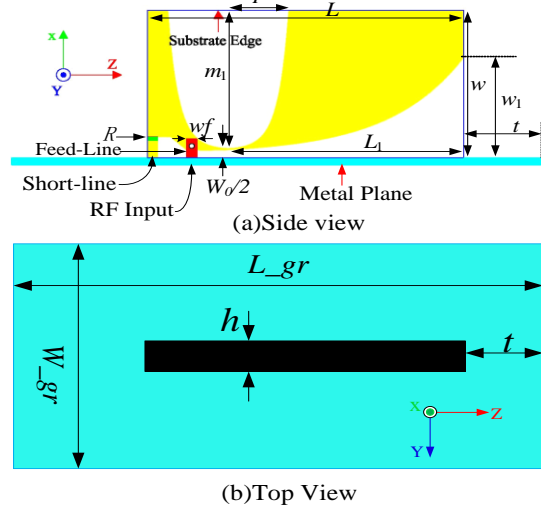


Fig. 1. Configuration of the proposed antenna.

The proposed antenna is located above a metal plane of size $W_{gr} \times L_{gr}$ ($200 \text{ mm} \times 200 \text{ mm}$), which is large enough for reducing the effect of SMA connector, and the top edge of that keeps a distance t from the edge of the metal plane. The proposed structure is optimized by using Ansoft High Frequency Structure Simulator (HFSS) and the optimized values are illustrated in Table 1.

Table 1: Parameters of the antenna as Fig. 1

| Parameter | m_1 | wf | w_0 |
|------------|-------|-------|---------|
| Value (mm) | 29.5 | 2 | 0.5 |
| Parameter | L_1 | L | t |
| Value (mm) | 45 | 60.5 | 0 |
| Parameter | w | w_1 | m |
| Value (mm) | 30 | 20 | $w-w_1$ |

III. SIMULATED AND MEASURED RESULTS

To validate the design concept, the prototype of the halved planar Vivaldi antenna was fabricated and tested. Measured and simulated VSWR for the proposed antenna are shown in Fig. 2, which presents a little discrepancy owing to the error of substrate parameters and tolerance in manufacturing. It is observed from Fig. 2 that the measured VSWR is less than 2.2 over the

frequency ranges of approximately 1.44-18.5 GHz (12.9:1), which almost satisfies the bandwidth requirement of 2-18 GHz. Radiation characteristics of the proposed antenna are also considered. The far-field radiation patterns of the proposed antenna in E-plane (xz -plane) and H-plane (yz -plane) for both E_ϕ and E_θ at frequencies of 2 GHz, 6 GHz and 10 GHz, are shown in Fig. 3. The measured patterns in general agree well with the simulated results. It is seen that the proposed antenna has directive radiation characteristics, and in E-plane the cross-polarization levels are 20 dB less than co-polarization levels. However, in H-plane, the cross-polarization curve has a deep depression in end-fire direction, which shows that the antenna has a high polarization ratio in end-fire direction, and in other directions the cross-polarization levels keep varying around -20 dB. It is also noticed that in E-plane, as the frequency is increased, the effective radiation area is far away from the edge of the metal plane; thus, the main beam direction

angle also increases, and when the frequency is increased continuously, the main beam direction angle keeps a maximum value of 30 degrees but a side lobe will be appeared in the close proximity of major lobe which varies from 65 to 80 degrees.

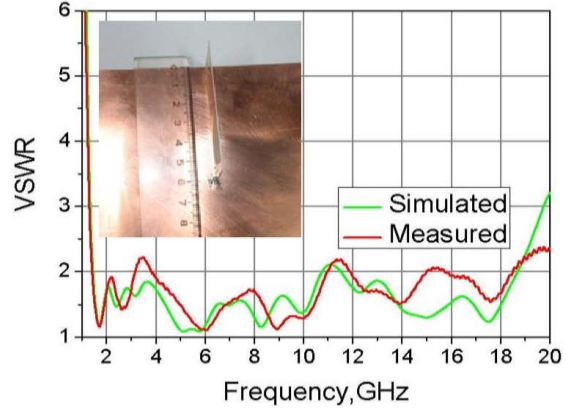


Fig. 2. Simulated and measured VSWR for the proposed antenna.

| Frequency (f) | Simulated Radiation Pattern | | Measured Radiation Pattern | |
|-------------------|-----------------------------|------------------------|----------------------------|------------------------|
| | E-plane (xz -plane) | H-plane (yz -plane) | E-plane (xz -plane) | H-plane (yz -plane) |
| 2 GHz | | | | |
| 6 GHz | | | | |
| 10 GHz | | | | |

Fig. 3. Normalized radiation pattern of the proposed antenna (— E_ϕ ; — E_θ).

With the help of the simulator HFSS, we can further study surface current distributions of the proposed antenna at two resonant frequencies (1.7 GHz and 5.8 GHz), which are presented in Fig. 4. It is seen clearly that at 1.7 GHz the main current

distributions are concentrated on the radiation slot-line and the end of slot-line, but for the other frequency the dominated current only flows along tapered slot, which proves the method of enhancing the bandwidth. It should be noticed that

Table 2 summarizes the performance comparison with other works [1,2,4,7] in terms of dielectric constant, size, operating frequency ranges, and bandwidth. By examining all the available low-profile tapered slot antennas, it was found that these designs are either using notched slot [2] which produces band-rejection in high frequency and can not extend higher working frequency ranges, or having larger size which is greater than $80 \times 140 \text{ mm}^2$ as in [4,7] or inadequate operating frequency ranges [1]. However, the proposed antenna not only has smaller size, but also has wider bandwidth.

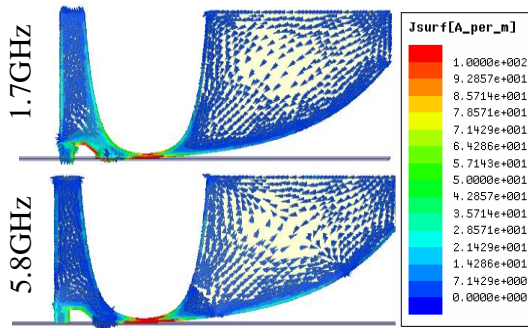


Fig. 4. Simulated current distributions of the proposed antenna at two lowest resonant frequencies.

Table 2: Performance comparison

| Works | ϵ_r | Dimension (mm ²) | Operating Frequency | Impedance Bandwidth |
|-----------|--------------|------------------------------|---------------------|---------------------|
| Ref. [1] | 2.65 | 18×23 | 6.2-12.3 GHz | 6.1 GHz |
| Ref. [2] | 4.55 | 35×36 | 3.1-10.6 GHz | 7.5 GHz |
| Ref. [4] | 2.65 | 170×300 | 0.89-13.8 GHz | 12.91 GHz |
| Ref. [7] | 4.4 | 80×140 | 1.8-14 GHz | 12.2 GHz |
| This work | 3.55 | 30×60.5 | 1.44-18.5 GHz | 17.06 GHz |

IV. PARAMETRIC STUDIES

In this section, parametric studies of the proposed antenna are presented to provide more detailed information about the antenna design and optimization. The parameters under study include the resistance value R , the substrate thickness h , length of radiation slot-line L_1 , height of radiation slot-line w_1 , and distance away from the edge of

ground plane t . To better understand the influence of the parameters on the performance of the antenna, only one parameter at a time will be varied, while others are kept unchanged unless especially indicated.

A. Resistance value (R)

To further enhance the bandwidth of the antenna, a resistor R is integrated at slot-line end of the antenna. Figure 5 shows the reflection coefficient curves for different values of R : 0 Ω , 50 Ω , 100 Ω , 200 Ω , and 500 Ω . It is clearly observed that the variation of the values of R has a significant effect on the reflection coefficient, especially in low frequency. As the figure describes, when the value of R is equal to zero, namely terminal patch shorted to the ground plane, the lowest resonant frequency is 2.72 GHz. However, as the resistor value of R becomes 100 Ω , the lowest resonant frequency becomes 1.5 GHz. If the value of R is increased continuously, such as to 500 Ω , the resonant frequency will be disappeared. This is owing to the current path extended as a resistor introduced, and an extra resonant mode is added in low frequency resulting in enhanced bandwidth, which seems to reasonably agree with surface current results shown in Fig. 4. For high frequency bands, the variation of R has minor effect on reflection coefficient value. Hence, to have a wider bandwidth, the resistance value R is selected as 100 Ω . It must be pointed out that the wider bandwidth is achieved due to not only the suitable resistance value, but also the dual-exponential edges configuration selected for smaller quality factor.

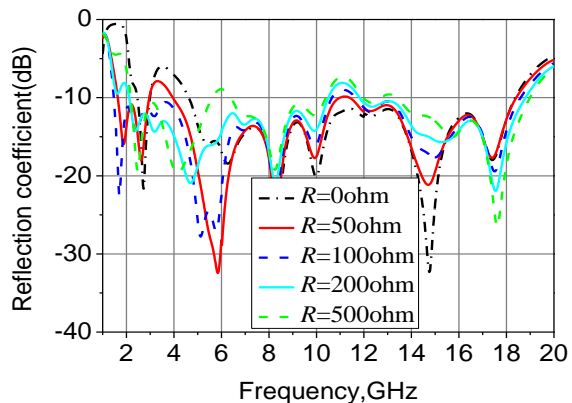


Fig. 5. Simulated reflection coefficient performances as a function of R .

B. Substrate thickness (h)

The effect of varying substrate thickness h on the antenna reflection coefficient is shown in Fig. 6. It is seen clearly from the figure that distance h has significant effect on the bandwidth of the antenna. With increasing h , the bandwidth is gradually decreased and cannot fully cover 1.5-18 GHz band. Hence, to have a wider impedance bandwidth, the distance h should be chosen as 0.5 mm.

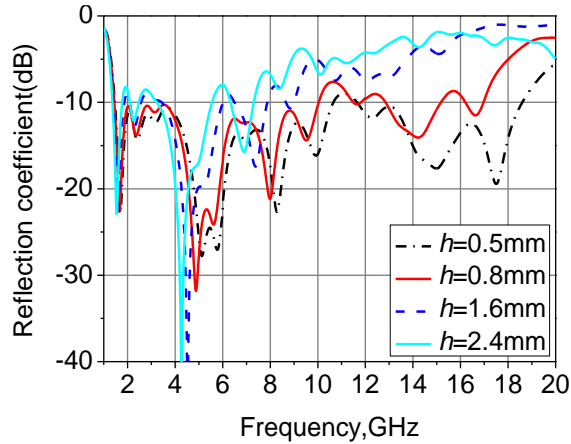


Fig. 6. Simulated reflection coefficient performances as a function of substrate thickness (h).

C. Length of radiation slot-line (L_1)

Figure 7 shows the effect of length L_1 of tapered slot line on reflection coefficient. The figure shows that with increasing L_1 from 40 mm to 65 mm, the reflection coefficient curves in low frequency bands have larger changes than that in high frequency bands. As depicted in Fig. 7, when the length L_1 is equal to 40 mm or 45 mm, the lowest resonant frequency occurs at 1.5 GHz; nevertheless, a stop-band is presented in low frequency as the length L_1 arrives at 55 mm and 65 mm (i.e., 2.8 GHz and 2.45 GHz, respectively). Figure 8 demonstrates the impact of varying the design parameter L_1 on the radiation pattern of the

proposed antenna. It is seen clearly from the figure that for same frequency with increasing the length L_1 , the proposed antenna keeps low cross-polarized levels, generally less than -20 dB at end-fire direction in E-plane (xz -plane) and H-plane (yz -plane), and the cross-polarized level in E-plane is lower than that in H-plane. It is also noticed that the radiation pattern is similar to monopole-like radiation at 2 GHz; in other words, the co-polarized pattern has two relative minimum points in x -axis to form a horizontal eight-shaped radiation pattern in E-plane and co-polarized pattern in H-plane keeps nearly omni-directional radiation pattern, which shows that the proposed antenna has vertical polarization characteristics. However, for same length L_1 , as frequency increases the main beam direction angle deviates from the z -axis and keeps the angle in 30 degrees, but when the working frequency exceeds 10 GHz the side lobe peak value will be increased, and the higher the frequency, more the side lobe will be. This behavior is largely due to the resonant slot working in high frequency away from the edge of ground plane, which leads to the radiant electromagnetic waves hardly crossing over the metal plane.

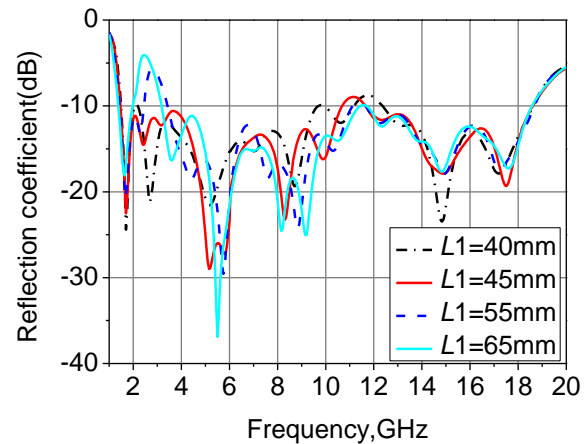


Fig. 7. Effect of length L_1 of radiation slot-line on the reflection coefficient.

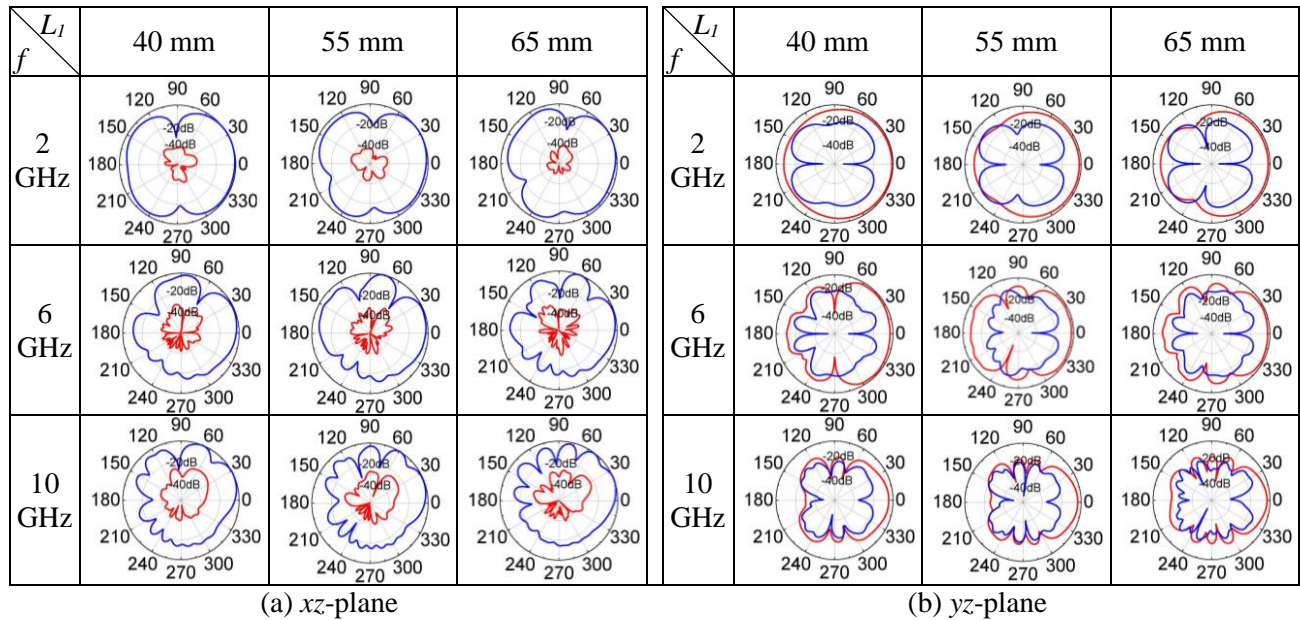


Fig. 8. Effect of length L_1 of tapered slot line on the radiation pattern (— E_ϕ ; — E_θ).

D. Width of radiation slot-line (w_1)

In this part of parametric studies, we change the height w_1 of antenna aperture to show effects of aperture dimensions on the reflection coefficient and radiation pattern. Figure 9 shows the simulation results for various values of aperture height when other parameters keep invariable. It can be seen that aperture height has larger effect on the reflection coefficient in low frequency bands than that in high frequency bands, and with increasing w_1 , the lowest resonant frequency is shifted downward and vice versa. On the other hand, Fig. 10 shows the effect of variation of height w_1 on the radiation pattern. It is found that in E-plane (xz -plane) when the height w_1 is increased, the radiation pattern keeps monopole-like radiation at 2 GHz. It is also observed from the E-plane figure that for same aperture height w_1 , with increasing frequency more minimum point of co-polarized pattern is also produced to form many side lobes, peak value of which is nearly equal to that of main beam, and the main beam directional angle measured from the z -axis increases (i.e., 30 degrees at 10 GHz). However, in H-plane, the co-polarized pattern almost remains unchanged when the height w_1 is varied, and for same height w_1 , with increasing frequency the co- and cross-

polarized patterns present random variation but the main beam direction of co-polarized pattern is always directed to z -axis and the cross-polarized pattern shows eight-shaped curve, the minimum point value of cross-polarized pattern is also increased. Note, that as the height w_1 is increased from 15 mm to 30 mm, the antenna also keeps low cross-polarization level with less than -20 dB at end-fire direction in both principal planes.

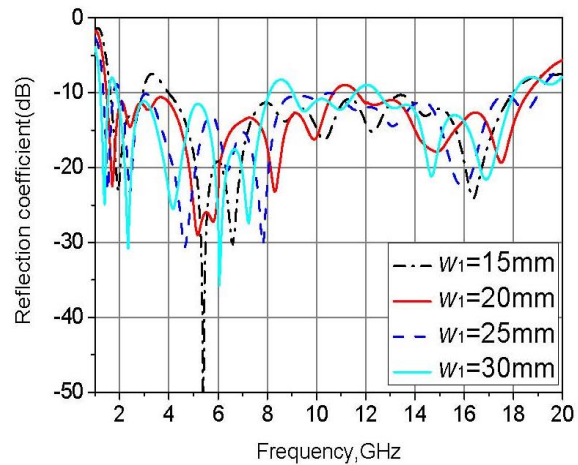


Fig. 9. Effect of height w_1 of antenna aperture on the reflection coefficient.

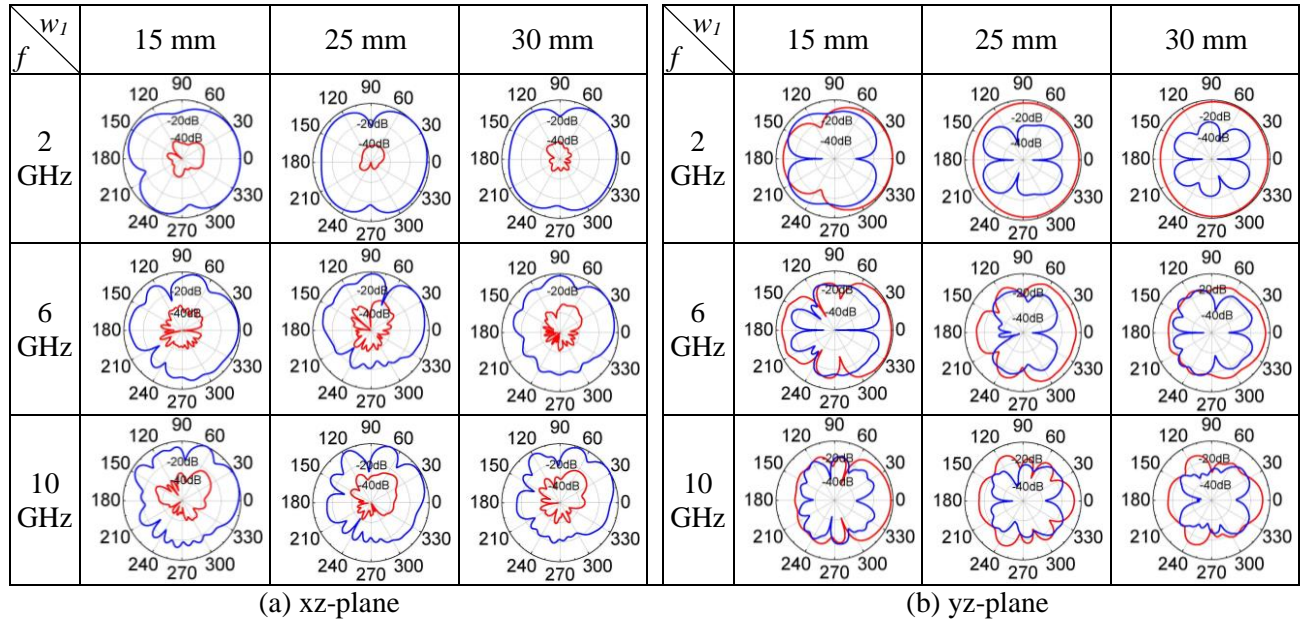


Fig. 10. Effect of height w_1 of antenna aperture on radiation pattern (— E_ϕ ; — E_θ).

E. Distance away from the edge of ground plane

To further know antenna performance, this section presents the effect of the variation of distance t on the reflection coefficient and radiation pattern. Figure 11 presents the effect of distance t on reflection coefficient. It is seen clearly that with variation of distance t , the reflection coefficient curves keep nearly invariable. Figure 12 demonstrates the impact of varying the parameter t on the radiation pattern of the proposed antenna. It is observed that for same working frequency as the distance t increases, the main beam direction angle of co-polarized pattern measured from the z -axis increases in E-plane; such as, at 2 GHz when distance t is equal to 5 mm, the main beam will be directed to z -axis, but when distance t is increased to 30 mm, the angle between main beam and z -axis is 30 degrees. If the distance t is increased continuously up to 50 mm, the main beam angle always remains at 30 degrees. Moreover, as the distance t keeps unchanged with increasing frequency, the side lobes are appeared in the close proximity of major lobe, and the higher the frequency, more the side lobe will be. As the frequency increases continuously, the main beam angle remains unchanged while the distance

t is varied from 5 to 50 mm. However, in H-plane, with increasing distance t , the co-polarized pattern almost keeps same shaped curve and cross-polarized pattern is also changed a little. It has been found that the variation of distance t has larger effect on E-plane radiation pattern as compared to the effect on the H-plane radiation pattern and the reflection coefficient.

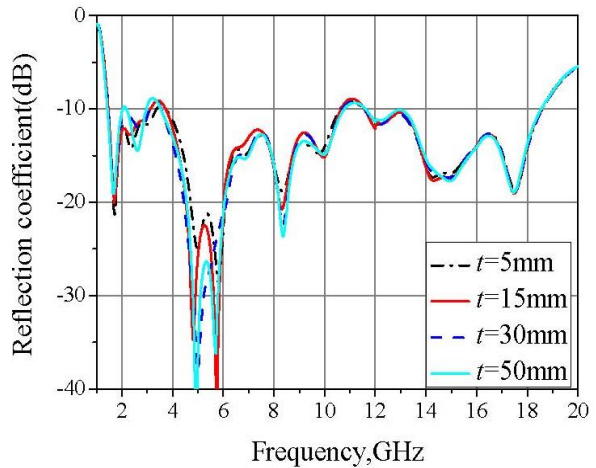


Fig. 11. Effect of distance t on reflection coefficient.

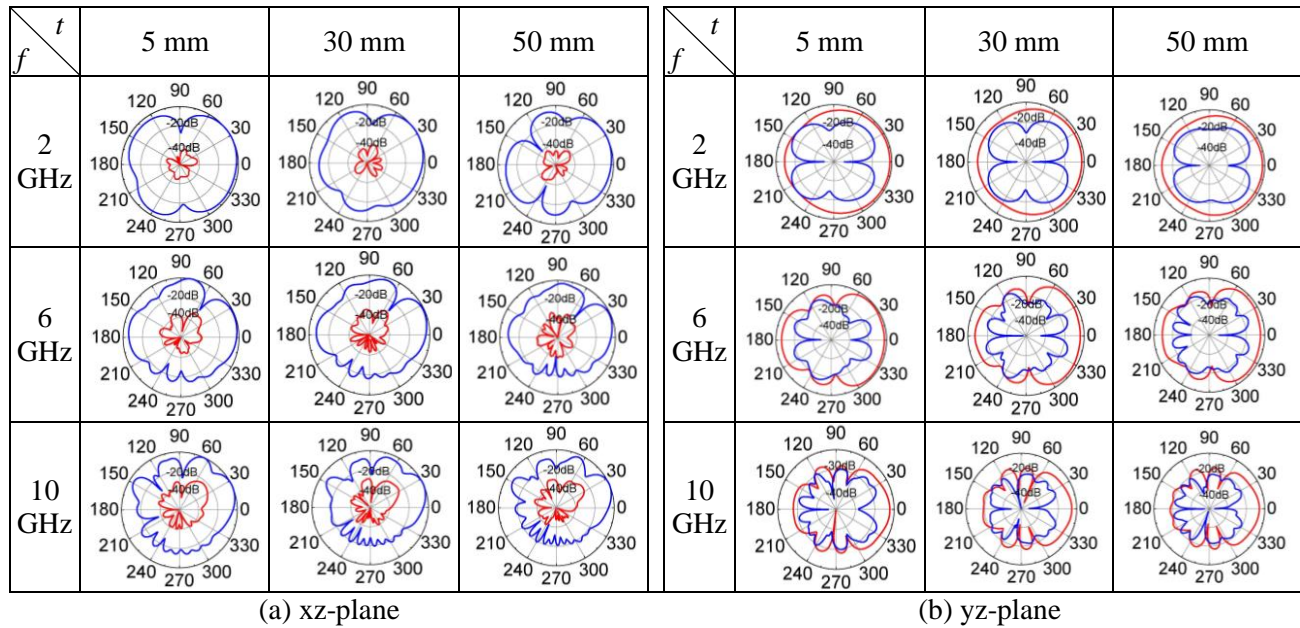


Fig. 12. Effect of the distance t on radiation pattern (— E_ϕ ; — E_θ).

V. CONCLUSION

In this paper, a compact halved Vivaldi antenna has been proposed, and the impedance bandwidth and radiation characteristics also have been presented. To obtain wide bandwidth and small size, a dual-exponential edges configuration is selected and a 100Ω resistor is integrated at the slot-line end of the proposed antenna. By adjusting each parameter carefully, it is easy to obtain the optimal antenna design and a small size of only $30 \text{ mm} \times 60.5 \text{ mm}$. The measured results show that the proposed antenna achieves an impedance bandwidth from 1.44 to 18.5 GHz for $\text{VSWR} \leq 2.2$, and has a cross-polarization level of more than 20 dB below the co-polarization level at end-fire direction. Overall, the proposed antenna has small size, low cross-polarization levels, directive radiation and vertically polarized characteristics. All these features make the proposed antenna a good candidate for mounting on metallic surface of a variety of communication systems, such as missile, unmanned aerial vehicles, and the like.

ACKNOWLEDGMENT

This work is supported by a Project from Science and Technology on Electronic Information Control Laboratory of China under Grant No. M16010101SYSJJ2010-5.

REFERENCES

- [1] F. Zhang, F. S. Zhang, G. Zhao, C. Lin, and Y. C. Jiao, "A loaded wideband linearly tapered slot antenna with broad beamwidth," *IEEE Antennas and Wireless Propag. Lett.*, vol. 10, pp. 79-82, 2011.
- [2] F. G. Zhu, S. Gao, et al., "Compact-size linearly tapered slot antenna for portable ultra-wideband imaging systems," *Int. J RF Microwave Comput.-Aided Eng.* (2012), first published online.
- [3] D. Schaubert, E. Kollberg, et al., "End-fire tapered slot antennas on dielectric substrates," *IEEE Trans. Antennas Propag.*, vol. 33, no. 12, pp. 1392-1400, 1985.
- [4] N. B. Wang, Y. C. Jiao, Y. Song, L. Zhang, and F. S. Zhang, "A microstrip-fed logarithmically tapered slot antenna for wideband applications," *Journal of Electromagnetic Waves and Applications*, vol. 23, pp. 1335-1344, 2009.
- [5] P. Wang, G. J. Wen, H. B. Zhang, and Y. H. Sun, "A wideband conformal end-fire antenna array mounted on a large conducting cylinder," *IEEE Trans. Antennas Propag.*, vol. 61, no. 9, 2013.
- [6] C. M. Hsu, L. Murphy, T. L. Chin, and E. Arvas, "Vivaldi antenna for GPR," *25th Annual Review of Progress in Applied Computational Electromagnetics*, pp. 8-12, California, March 2009.
- [7] B. Zhou, H. Li, X. Y. Zou, and T. J. Cui, "Broadband and high-gain planar vivaldi antennas based on inhomogeneous anisotropic zero-index metamaterials," *Progress In Electromagnetics*

- Research*, vol. 120, pp. 235-247, 2011.
- [8] P. Wang, H. B. Zhang, G. J. Wen, and Y. H. Sun, "Design of modified 6-18 GHz balanced antipodal vivaldi antenna," *Progress In Electromagnetics Research C*, vol. 25, pp. 271-285, 2012.
- [9] P. Wang, G. J. Wen, Y. H. Sun, and H. B. Zhang, "Design of wideband conformal end-fire antenna array on a large conducting cylinder," *2012 IEEE Asia-Pacific Conference on Antennas and Propagation*, pp. 27-29, Singapore, August 2012.
- [10] J. R. Verbiest and G. A. E. Vandenbosch, "Low-cost small-size tapered slot antenna for lower band UWB applications," *Electron. Lett.*, vol. 42, pp. 670-671, 2006.
- [11] J. Shin and D. H. Schaubert, "A parameter study of stripline-fed vivaldi notch-antenna arrays," *IEEE Trans. Antennas Propag.*, vol. 47, no. 5, pp. 879-886, 1999.
- [12] E. W. Reid, L. O. Balbuena, and K. Moez, "Integrated low-loss balun for vivaldi antennas," *Electron. Lett.*, vol. 45, pp. 442-444, 2009.
- [13] E. W. Reid, L. O. Balbuena, A. Ghadiri, and K. Moez, "A 324-element vivaldi antenna array for radio astronomy instrumentation," *IEEE Trans. Instru. Measur.*, vol. 61, no. 1, pp. 241-250, 2012.



Ping Wang was born in Chongqing, China, in 1981. He received his B.S. degree in Physics from Western Chongqing University of China, in 2005, and the M.S. degree in Theoretical Physics from Chongqing University, Chongqing, in 2008.

Currently, he is working towards his Ph.D. degree at the University of Electronic Science and Technology of China (UESTC). His current research interests include patch antennas, wideband antennas, and arrays.



Guangjun Wen was born in Sichuan, China, in 1964. He received his M.S. and Ph.D. degrees from Chongqing University of China in 1995 and from University of Electronic Science and Technology of China in 1998, respectively. He is currently a

Professor at the University of Electronic Science and Technology of China. His research and industrial experience covers a broad spectrum of electromagnetics, including RF, Microwave, Millimeter wave Integrated Circuits and Systems design, and networks, antennas, as well as, model of electromagnetic metamaterial.



Yongjun Huang was born in Sichuan, China, in 1985. Currently, he is working towards his Ph.D. degree at the University of Electronic Science and Technology of China (UESTC). His research interests include electromagnetic metamaterial and its application in

microwave engineering area, FDTD analysis for the model and RCS characteristic of metamaterials.

Haobin Zhang received his Ph.D degree in Northwest Polytechnical University, China. Currently, he is working at Science and Technology on Electronic Information Control Laboratory of China. His research interests include analytical and numerical modeling of antenna, and antenna theory and design.

Multi-Resonance Monopole Antenna with Inverted Y-Shaped Slit and Conductor-Backed Plane

S. Ojaroudi ¹, Y. Ojaroudi ¹, and N. Ojaroudi ²

¹ Young Researchers and Elite Club
Islamic Azad University, Germe Branch, Germe, Iran

² Young Researchers and Elite Club
Islamic Azad University, Ardabil Branch, Ardabil, Iran
n.ojaroudi@yahoo.com

Abstract — This manuscript introduces a new design of multi-resonance monopole antenna for Ultra-Wideband (UWB) applications. The proposed antenna consists of an ordinary square radiating patch and a modified ground plane with inverted Y-shaped slit and conductor-backed plane, which provides a wide usable fractional bandwidth of more than 135%. By cutting an inverted Y-shaped slit in the ground plane and also by embedding an Inverted Y-shaped conductor-backed plane in the feed gap distance, additional (third and fourth) resonances are excited and hence much wider impedance bandwidth can be produced; especially at the higher band. By obtaining these resonances, the usable lower frequency is decreased from 3.12 to 2.9 GHz, and also the usable upper frequency of the presented monopole antenna is extended from 10.3 to 14.85 GHz. The measured results show that the proposed antenna can achieve the Voltage Standing Wave Ratio (VSWR) requirement of less than 2.0 in frequency range from 2.83 to 14.87 GHz, which is suitable for UWB systems.

Index Terms — Bandwidth enhancement, conductor-backed plane, DGS, UWB applications.

I. INTRODUCTION

After allocation of the frequency band from 3.1 to 10.6 GHz for the commercial use of Ultra-Wideband (UWB) systems by the Federal Communication Commission (FCC) [1], ultra-wideband systems have received phenomenal gravitation in wireless communication. Designing

an antenna to operate in the UWB band is quite a challenge, because it has to satisfy the requirements such as ultra wide impedance bandwidth, omni-directional radiation pattern, constant gain, high radiation efficiency, constant group delay, low profile, easy manufacturing, etc. [2]. In UWB communication systems, one of key issues is the design of a compact antenna while providing wideband characteristic over the whole operating band. Consequently, a number of microstrip antennas with different geometries have been experimentally characterized [3-4]. Some methods are used to obtain the multi-resonance function in the literature [5-8].

In this paper, a new design is proposed to obtain the very wideband bandwidth for the compact monopole antenna. In the proposed antenna, to obtain the multi-resonance property, the inverted Y-shaped slit and conductor-backed plane are used in the ground plane, which provides a wide usable fractional bandwidth of more than 130%. Regarding Defected Ground Structures (DGS) theory, the creating slits in the ground plane provide additional current paths. Moreover, these structures change the inductance and capacitance of the input impedance, which in turn leads to change the bandwidth [9].

Therefore, by cutting an inverted Y-shaped slit in the ground plane, much enhanced impedance bandwidth may be achieved. In addition, based on Electromagnetic Coupling Theory (ECT), by adding an inverted Y-shaped conductor-backed plane in the air gap distance, additional coupling is introduced between the bottom edge of the square

patch and the ground plane and its impedance bandwidth is improved without any cost of size or expense. The proposed antenna has an ordinary square radiating patch, therefore displays good omni-directional radiation patterns even at the higher frequencies.

II. MICROSTRIP ANTENNA DESIGN

The presented small monopole antenna fed by a microstrip line is shown in Fig. 1, which is printed on an FR4 substrate of thickness of 1.6 mm, permittivity of 4.4, and loss tangent 0.018.

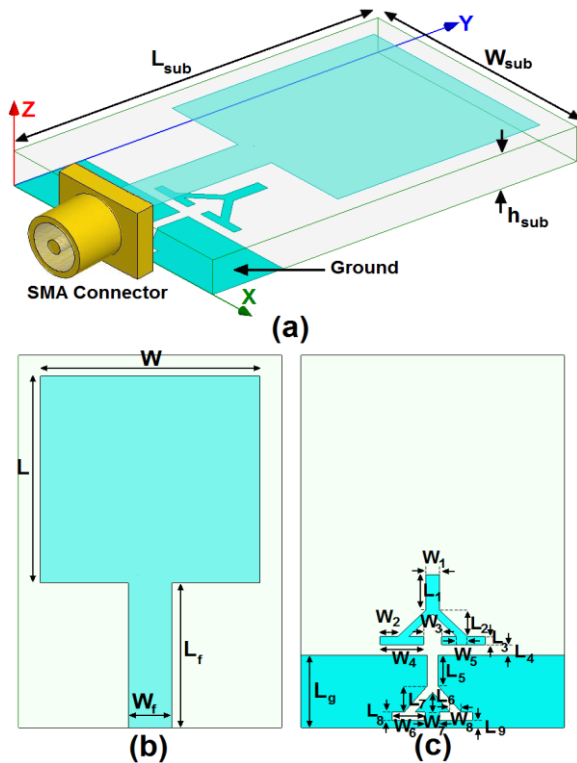


Fig. 1. Geometry of proposed monopole antenna: (a) side view, (b) top layer, and (c) bottom layer.

The basic monopole antenna structure consists of a square patch, a feed line and a ground plane. The square radiating patch has a width W . The patch is connected to a feed line of width W_f and length L_f . The width of the microstrip feed line is fixed at 2 mm, as shown in Fig. 1. On the other side of the substrate, a conducting ground plane with two inverted fork-shaped slits and a pair of Γ -shaped parasitic structures is placed. The proposed antenna is connected to a 50-SMA connector for signal transmission.

The DGS applied to a ground plane causes a resonant character of the structure transmission with a resonant frequency controllable by changing the shape and size of the slits. In addition, based on ECT, by using a parasitic structure in the feed gap distance, the antenna impedance bandwidth is improved. The final dimensions of the designed antenna are specified in Table 1.

Table 1: Final dimensions of the antenna

| | | | | | |
|------------|-----------|-----------|-----------|-------|-------|
| Parameter | W_{sub} | L_{sub} | h_{sub} | W | L |
| Value (mm) | 12 | 18 | 1.6 | 10 | 10 |
| Parameter | W_1 | L_1 | W_2 | L_2 | W_3 |
| Value (mm) | 0.5 | 1.7 | 0.8 | 1.3 | 0.8 |
| Parameter | L_3 | W_f | L_f | W_4 | L_4 |
| Value (mm) | 0.4 | 2 | 7 | 2 | 0.5 |
| Parameter | W_5 | L_5 | W_6 | L_6 | W_7 |
| Value (mm) | 0.5 | 1.5 | 1.5 | 1 | 0.7 |
| Parameter | L_7 | W_8 | L_8 | L_9 | L_g |
| Value (mm) | 1.25 | 0.5 | 0.4 | 0.35 | 3.5 |

III. RESULTS AND DISCUSSIONS

The proposed microstrip monopole antenna with various design parameters was constructed and the numerical and experimental results of input impedance and radiation characteristics are presented and discussed. The analysis and performance of the proposed antenna is explored by using Ansoft simulation software High-Frequency Structure Simulator (HFSS) [10], for better impedance matching.

Figure 2 shows the configuration of the various antennas used for simulation studies. VSWR characteristics for ordinary monopole antenna (Fig. 2 (a)), the antenna with an inverted Y-shaped slits (Fig. 2 (b)), and the proposed antenna (Fig. 2 (c)) structures are compared in Fig. 3. As shown in Fig. 3, in the proposed antenna configuration, the ordinary square monopole can provide the fundamental and next higher resonant radiation band at 4.8 and 8.1 GHz, respectively, in the absence of the inverted Y-shaped slit and conductor-backed plane structures. It is observed that by using these modified elements, additional third (10.3 GHz) and fourth (14.4 GHz) resonances are excited, respectively, and hence, the bandwidth is increased. Also, the input impedance of the proposed antenna on a Smith Chart is shown in Fig. 4.

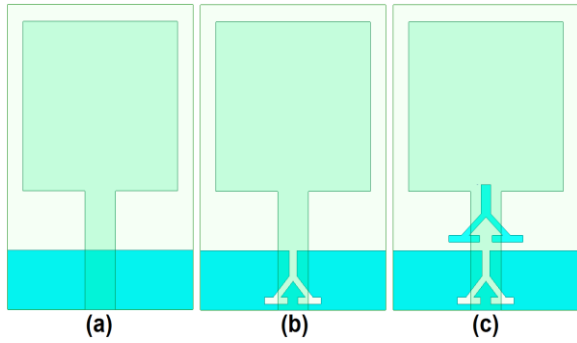


Fig. 2. (a) Ordinary square monopole antenna, (b) square antenna with an inverted Y-shaped slit in the ground plane, and (c) the proposed monopole antenna.

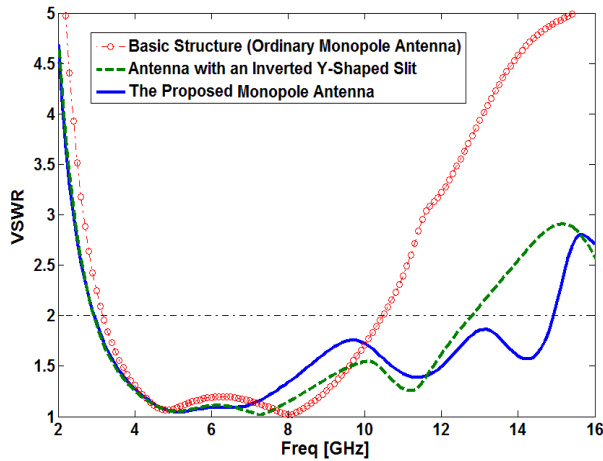


Fig. 3. Simulated VSWR characteristics for the various monopole antennas shown in Fig. 2.

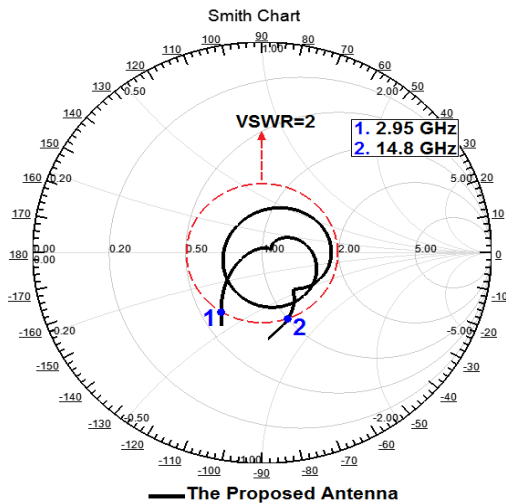


Fig. 4. Simulated input impedance on a Smith Chart for the proposed antenna.

In order to understand the phenomenon behind the multi-resonance performance of the proposed, the simulated current distributions on the ground plane for the proposed antenna at 5, 6.7, 11.3 and 14.4 GHz (resonance frequencies) are presented in Fig. 5. As illustrated in Figs. 5 (a) and 5 (b), at the lower frequencies it can be observed that the directions of surface currents at the ground plane are reversed in comparison with each other, which cause the antenna impedance changes at these frequencies. Also, as shown in Figs. 5(c) and 5 (d), at the additional resonances frequencies (third and fourth) the currents concentrated on the edges of the interior and exterior of the inverted Y-shaped slits and conductor-backed plane [11].

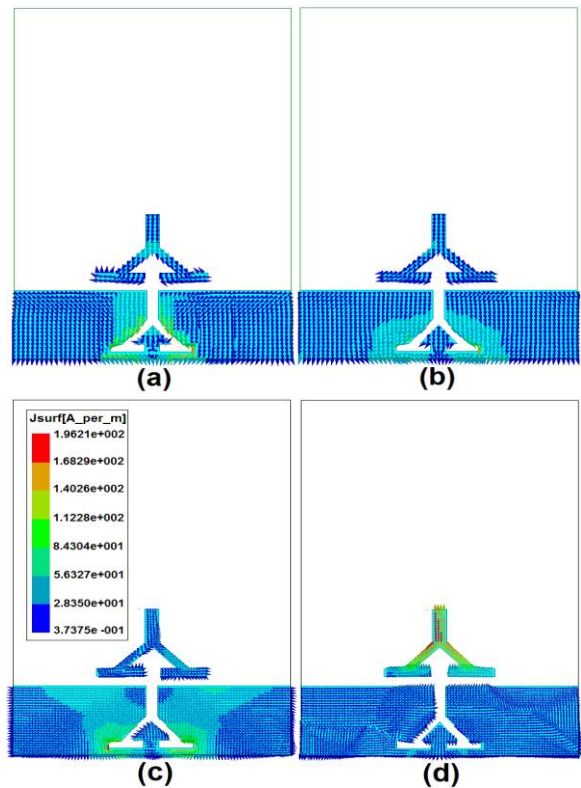


Fig. 5. Simulated surface current distributions on the ground plane for the proposed antenna at: (a) 5 GHz, (b) 6.7 GHz, (c) 11.3 GHz, and (d) 14.4 GHz.

The proposed antenna was fabricated and tested. Figure 6 shows the measured and simulated radiation patterns, including the co-polarization in the *H*-plane (*x-z* plane) and *E*-plane (*y-z* plane). The main purpose of the radiating patterns is to demonstrate that the antenna actually radiates over

a wide frequency band. It can be seen that the radiation patterns in x - z plane are nearly omnidirectional for the three frequencies. The radiation patterns on the y - z plane are like a small electric dipole leading to bidirectional patterns in a very wide frequency band. With the increase of frequency, the radiation patterns become worse, because of the increasing effects of the cross-polarization [12-13].

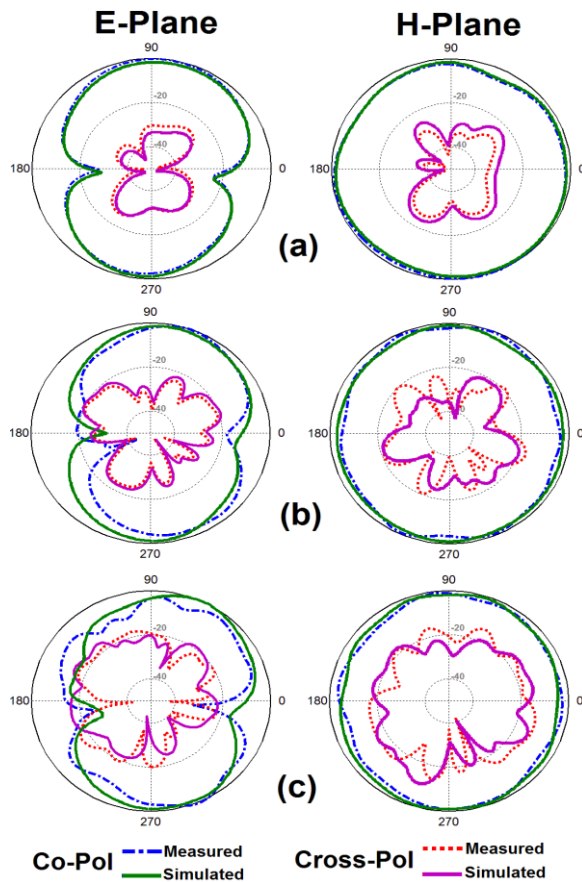


Fig. 6. Measured and simulated radiation patterns of the proposed antenna: (a) 5 GHz, (b) 9 GHz, and (c) 13 GHz.

Figures 7 and 8 show the measured and simulated VSWR and return loss characteristics of the proposed antenna. As seen, the fabricated antenna has the frequency band of 2.95 to 14.84 GHz.

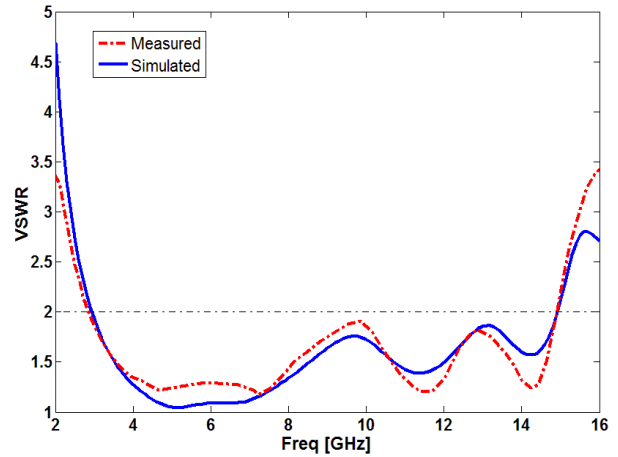


Fig. 7. Measured and simulated VSWR characteristics for the proposed antenna.

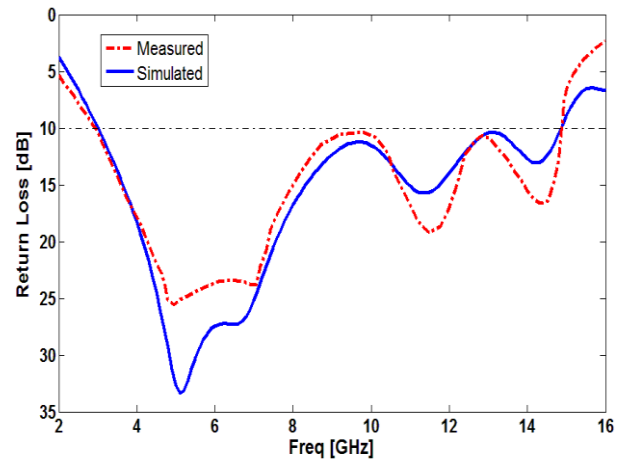


Fig. 8. Measured and simulated return loss characteristics for the proposed antenna.

The simulated radiation efficiency characteristic of the proposed antenna is shown in Fig. 9. Results of the calculations using the software HFSS, indicated that the proposed antenna features a good efficiency, being greater than 82% across the entire radiating band. In addition, the measured maximum gain of the antenna against frequency is illustrated in Fig. 9. The antenna gain has a flat property which increases by the frequency. As seen, the proposed antenna has sufficient and acceptable gain levels

in the operation bands [14-15].

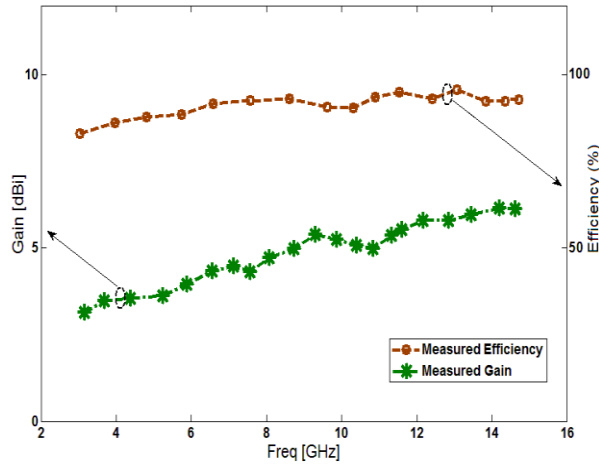


Fig. 9. Radiation efficiency (simulated) and gain (measured) characteristics of the antenna.

The radiating mechanism of the proposed antenna is more novel than was explained in previous works. The proposed structure is the combination of the monopole antenna with the dipole and slot antenna. In this study, the modified ground-plane structure is the combination of the monopole antenna and the slot antenna. By using the modified conductor-backed plane, the interaction of the two parts of the overall antenna is occurred. The embedding parasitic structure in the ground plane of the monopole antenna acts as a dipole antenna that can provide an additional current path. Also, the entire back conducting plane could be part of the radiator, especially when operating at lower frequencies [16].

Table 2 summarizes the proposed antenna and the previous designs [17-24]. As seen, the proposed antenna has a compact size with very wide bandwidth, in comparison with the previous works. In addition, the proposed antenna has good omni-directional radiation patterns with low cross-polarization level, even at the higher and upper frequencies. As the proposed antenna has symmetrical structure and an ordinary square radiating patch without any slot and parasitic structures at top layer, in comparison with previous multi-resonance UWB antennas, the proposed antenna displays a good omni-directional radiation pattern even at lower and higher frequencies. Also, the proposed antenna has sufficient and acceptable radiation efficiency,

group delay and antenna gain levels in the operation bands [25-28].

Table 2: Comparison of previous designs with the proposed antenna

| Ref. | FBW (%) | Dimension (mm) | Gain (dBi) |
|------------------|-------------|----------------|----------------|
| [17] | 47% | 33×33 | 3.5~6 |
| [18] | 87% | 22×24 | 1~5.5 |
| [19] | 87% | 32×25 | 2~5.5 |
| [20] | 91% | 26×26 | 3-7 |
| [21] | 112% | 20×20 | 2~4.7 |
| [22] | 118% | 40×10 | 2.3~6.3 |
| [23] | 130% | 12×18 | 2.7-5.5 |
| [24] | 132% | 25×26 | not reported |
| <i>This Work</i> | <i>136%</i> | <i>12×18</i> | <i>3.2~6.3</i> |

IV. CONCLUSION

In this manuscript, a compact Printed Monopole Antenna (PMA) with multi-resonance characteristic for UWB applications has been proposed. The fabricated antenna can operate from 2.95 to 14.84 GHz. In order to enhance the bandwidth, an inverted Y-shaped slit is inserted in the ground plane and also by adding an inverted Y-shaped conductor-backed plane structure, additional third and fourth resonances are excited, and hence much wider impedance bandwidth can be produced. The designed antenna has a simple configuration with small size of $12 \times 18 \text{ mm}^2$. Simulated and experimental results show that the proposed antenna could be a good candidate for UWB systems application.

ACKNOWLEDGMENT

The author is thankful to MWT Company staff for their help (www.microwave-technology.com).

REFERENCES

- [1] "FCC News release," *FCC NEWS (FCC 02-48)*, February 14, 2002.
- [2] D. Cheng, "Compact ultra wideband microstrip resonating antenna," *US Patent 7872606*, January 2011.
- [3] N. Ojaroudi, "Design of ultra-wideband monopole antenna with enhanced bandwidth," *21st Telecommunications Forum, TELFOR 2013*, Belgrade, Serbia, pp. 1043-1046, November 27-28, 2013.
- [4] N. Ojaroudi, "A new design of koch fractal slot antenna for ultra-wideband applications," *21st*

- Telecommunications Forum, TELFOR 2013*, Belgrade, Serbia, pp. 1051-1054, November 27-28, 2013.
- [5] N. Ojaroudi, "Compact UWB monopole antenna with enhanced bandwidth using rotated I-shaped slots and parasitic structures," *Microw. Opt. Technol. Lett.*, vol. 56, pp. 175-178, 2014.
- [6] A. Dastranj and H. Abiri, "Bandwidth enhancement of printed e-shaped slot antennas fed by CPW and microstrip line," *IEEE Trans. Antenna Propag.*, vol. 58, pp. 1402-1407, 2010.
- [7] A. J. Kerkhoff, R. L. Rogers, and H. Ling, "Design and analysis of planar monopole antennas using a genetic algorithm approach," *IEEE Trans Antennas Propag.*, vol. 2, pp. 1768-1771, 2004.
- [8] N. Ojaroudi, S. Amiri, and F. Geran, "A novel design of reconfigurable monopole antenna for UWB applications," *Applied Computational Electromagnetics Society (ACES) Journal*, vol. 28, no. 6, pp. 633-639, July 2013.
- [9] K. Chung, T. Yun, and J. Choi, "Wideband CPW-fed monopole antenna with parasitic elements and slots," *Electronics Letters*, vol. 40, no. 17, pp. 1038-1040, 2004.
- [10] "Ansoft high frequency structure simulation (HFSS)," ver. 13, Ansoft Corporation, 2010.
- [11] T. K. Pakkiam, J. S. Mandeep, and M. T. Islam, "Design of microstrip antenna for modern wireless communication," *1st IEEE International Symposium on Telecommunication Technologies*, 2012.
- [12] N. Ojaroudi, "Application of protruded strip resonators to design an UWB slot antenna with WLAN band-notched characteristic," *Progress in Electromagnetics Research C*, vol. 47, pp. 111-117, 2014.
- [13] N. Ojaroudi, "Design of small reconfigurable microstrip antenna for UWB-CR applications," *19th International Symposium on Antenna and Propagation, ISAP2014*, Kaohsiung, Taiwan, December 2-5, 2012.
- [14] L. Liu, S. W. Cheung, R. Azim, and M. T. Islam, "A compact circular-ring antenna for ultra-wideband applications," *Microwave and Optical Technology Letters*, vol. 53, no. 10, pp. 2283-2288, 2011.
- [15] R. Azim, M. T. Islam, N. Misran, S. W. Cheung, and Y. Yamada, "Planar UWB antenna with multi-slotted ground plane," *Microwave and Optical Technology Letters*, vol. 53, no. 5, pp. 966-968, 2011.
- [16] R. Azim, M. T. Islam, and N. Misran, "Ground modified double-sided printed compact UWB antenna," *Electronics Letters*, vol. 47, no. 1, pp. 9-11, 2011.
- [17] W. L. Chen, G. M. Wang, and C. X. Zhang, "Bandwidth enhancement of a microstrip-line-fed printed wide-slot antenna with a fractal-shaped slot," *IEEE Transactions on Antennas and Propagation*, vol. 57, pp. 1276-2179, 2009.
- [18] R. Azim, M. T. Islam, and N. Misran, "Compact tapered-shape slot antenna for UWB applications," *IEEE Antennas and Wireless Propagation Letters*, vol. 10, pp. 1190-1193, 2011.
- [19] Y. Li, W. Li, Y. Lu, "A switchable UWB slot antenna using SIS-HSIR and SIS-SIR for multi-mode wireless communications applications," *Applied Computational Electromagnetics Society (ACES) Journal*, vol. 27, pp. 340-351, 2012.
- [20] L. Liu, S. W. Cheung, and T. I. Yuk, "Compact MIMO antenna for portable devices in UWB applications," *IEEE Transactions on Antennas and Propagation*, vol. 61, pp. 4257-4264, 2013.
- [21] M. Ojaroudi and N. Ojaroudi, "Ultra-wideband small rectangular slot antenna with variable band-stop function," *IEEE Trans. Antennas Propag.*, vol. 62, pp. 490-494, 2014.
- [22] X. N. Low, Z. N. Chen, and T. S. P. See, "A UWB dipole antenna with enhanced impedance and gain performance," *IEEE Transactions on Antennas and Propagation*, vol. 57, pp. 2966-2959, 2009.
- [23] N. Ojaroudi and M. Ojaroudi, "Small monopole antenna with multiresonance characteristic by using rotated t-shaped slit and parasitic structure for UWB systems," *Microw. Opt. Technol. Lett.*, vol. 55, pp. 482-485, 2013.
- [24] A. K. Gautam, S. Yadav, and B. K. Kanaujia, "A CPW-fed compact UWB microstrip antenna," *IEEE Antennas and Wireless Propagation Letters*, vol. 12, pp. 151-154, 2013.
- [25] N. Ojaroudi, "Small microstrip-fed slot antenna with frequency band-stop function," *21st Telecommunications Forum, TELFOR 2013*, Belgrade, Serbia, pp. 1047-1050, November 27-28, 2013.
- [26] N. Ojaroudi, "Design of microstrip antenna for 2.4/5.8 GHz RFID applications," *German Microwave Conference, GeMic 2014*, RWTH Aachen University, Germany, March 10-12, 2014.
- [27] N. Ojaroudi, "Microstrip monopole antenna with dual band-stop function for UWB applications," *Microw. Opt. Technol. Lett.*, vol. 56, pp. 818-822, 2014.
- [28] N. Ojaroudi, "New design of multi-band PIFA for wireless communication systems," *19th International Symposium on Antenna and Propagation, ISAP2014*, Kaohsiung, Taiwan, December 2-5, 2012.

Analytical Estimation of Radar Cross Section of Arbitrary Compact Dipole Array

H. L. Sneha, Hema Singh, and R. M. Jha

Centre for Electromagnetics
CSIR-National Aerospace Laboratories, Bangalore 560017, India
hemasingh@nal.res.in, jha@nal.res.in

Abstract — This paper presents the scattering estimation and analysis of an arbitrary phased array with parallel, centre-fed dipole elements, in the presence of mutual coupling. The total Radar Cross Section (RCS) of the uniform dipole array is computed by considering the signal reflections within the array system. The results are shown for two types of feed networks, *viz.* series feed and parallel feed. The scattering due to higher order reflections and edge effects are neglected. The analytical formulae presented for array RCS emphasize the dependence of scattered field on the design parameters, like dipole length, inter-element spacing, geometrical and electrical properties of phase shifters, couplers and terminal impedances. The results indicate that the mutual coupling effect on the overall RCS pattern is identical for both equal and unequal length dipole arrays. This paper identifies the design parameters that can be optimized towards the RCS control of phased array. These parameters include dipole-length, geometric configuration and terminal impedance.

Index Terms — Dipole array, feed network, impedance mismatch, Radar Cross Section (RCS), reflection, transmission.

I. INTRODUCTION

Radar Cross Section (RCS) relates the electromagnetic energy at the receiver due to the reflection from the target to the electromagnetic energy impinging on it. The total antenna radar cross section consists of both structural RCS and antenna mode RCS [1]. However, for an antenna array operating within the frequency band similar to that of radar, the scattering due to antenna mode

becomes predominant [2]. An efficient antenna system is required to meet the requirements of both optimum radiation characteristics and low detectability. In few cases, the antenna RCS becomes even greater than the structural RCS of the platform. Hence, it is essential that RCS of an object is reduced without affecting its radiation performance [3]. In order to achieve this objective, a detailed and accurate analysis of antenna mode scattering is required.

The estimation of antenna array scattering should include the effect of feed network architecture, terminating impedance, and mutual coupling. The total scattered field of an antenna array comprises of the fields reflected from different impedance mismatches at each level of feed network [4]. The corresponding scattered field magnitudes can be expressed in terms of reflection coefficients and terminal impedances of the array elements. Further, the values of the terminal impedances are influenced by the mutual coupling effect, which depends on the array geometry. This makes it crucial to analyze the signal path through each of the junction and mismatches within the antenna system towards the RCS estimation of phased array.

The scattering behavior of phased array has been determined and analyzed using various techniques. A finite dipole array has been studied in view of its radiation and scattering characteristics with the compensation of coupling effect [5]. The moment method along with RWG basis functions is used to calculate scattered field of equal half-wavelength dipoles, in the presence of mutual coupling. Although, the parametric analysis of scattering behavior of dipole array is presented, the feed network is not considered. The

numerical technique like FDTD method is also employed to calculate the scattering from impedance loaded dipole array without feed network [6].

The scattering behavior of antenna array with feed network has been reported but for infinitesimal dipole array [2], [7]. Moreover, the results presented ignore the mutual coupling effect in between the dipole elements. However, in a practical phased array, one cannot ignore the finite dimensions of antenna elements, coupling effect and the role of feed network while estimating the antenna RCS. The RCS of finite dipole array with series and parallel feed network including mutual coupling effect has been determined in terms of network parameters [8]. The dipoles were considered to be of equal length in different geometric configurations. In this paper, the RCS estimation of arbitrary dipole array for both series and parallel feed network is presented. In particular, the array design for unequal-length dipoles differs from earlier work [8] in two aspects. At first, it uses an extra component, which can be either the waveguide bend or the transmission line, in order to connect the dipole terminals to the corresponding phase-shifter. This extra component is taken as perfectly matched line towards the phase-shifters so as to have zero contribution towards total array RCS, for the sake of convenience. Otherwise, the impedance mismatch within this extra line is to be included in the calculations. Secondly, the dipole lengths are taken to be unequal as an attempt towards the RCS reduction within the arbitrary array system.

In this paper, an arbitrary compact dipole array is considered, in which the dipole can be either equal-length or unequal-length. Unlike [9], the results include both linear and planar dipole array.

The scattered field is determined in terms of reflections and transmissions of the signal propagating through the levels of the array system. It is the impedance mismatch at each level of the feed that results in the total scattering cross section of the array system. In the subsequent sections, the detailed analytical description of the RCS estimation of dipole array is presented. The equations derived can be used for both equal and unequal-length dipole array, with either series or parallel feed network.

II. RCS OF DIPOLE ARRAY

A uniform linear array of centre-fed dipoles each with length of $2l_n$, $n=1,2,\dots,N$ is considered. The inter-element spacing is taken as d and the staggered height of the dipoles from the reference plane is assumed to be h_n . The geometry of dipole array considered is generalized and it can be converted to any standard array configuration, like side-by-side, collinear or parallel-in-echelon by appropriate changes in the design parameters.

The dipoles in the array are excited by a feed network comprising of extra component, phase-shifters and couplers, in order from radiators towards the receive port. Assuming the dipoles in the array to be lossless and x -polarized, the scattered field at n^{th} dipole is given as [2], [8]:

$$|\vec{E}_n^s(\theta, \varphi)| = \left[\frac{j\eta_0}{4\lambda Z_{s_n}} \left(\int_{\Delta_n} \cos(kl_n) dl_n \right)^2 (\cos\theta) \vec{E}_n^r(\theta, \varphi) \right] \frac{e^{-j\vec{k}\vec{R}}}{R} \hat{x}, \quad (1)$$

where λ is the wavelength, η_0 is the impedance of free space, \vec{k} is the propagation vector, R is the distance between the target and the receiver, l_n is the length of n^{th} dipole element, $\vec{E}_n^r(\theta, \varphi)$ is the total reflected field towards the aperture, and Z_{s_n} is the impedance of n^{th} dipole element. It is pointed out that for the simpler case of isotropic source, related expression has been earlier derived by Jenn [2]. In order to determine the total RCS of N -element dipole array, scattered fields at each of its elements are summed-up. Thus, the scattered field is expressed as [8]:

$$|\vec{E}_n^s(\theta, \varphi)| = \left[\frac{j\eta_0}{4\lambda Z_{s_n}} \left(\int_{\Delta_n} \cos(kl_n) dl_n \right)^2 (\cos\theta) \vec{E}_n^r(\theta, \varphi) \right] \frac{e^{-j\vec{k}\vec{R}}}{R} \hat{x}. \quad (2)$$

The total scattered field, and hence the RCS of the dipole array can be decomposed in terms of individual reflections at each level including antenna aperture and the feed network. These reflected fields are determined by the magnitude of reflection coefficients as per the path through which the signal propagates within the array. As a result, the RCS of the dipole array is specific to the structure of the feed network used to excite the antenna elements. In this paper, the scattering from arbitrary dipole array for two different feed networks, (i) series feed and (ii) parallel feed is derived. Since the network architecture remains the same for either type of feeds till one reaches

the coupler level, the contribution to the total RCS remains identical for all the levels preceding the level of coupler(s) in antenna system.

A. Reflection at the dipole terminals

The first source of scattering for a signal impinging on the array (Fig. 1) is the junction of radiators and connectors. The corresponding RCS equation is given as:

$$\sigma_r(\theta, \varphi) = \frac{4\pi}{\lambda^2} \left| \sum_{n=1}^N \left\{ \frac{j\eta_0}{4\lambda Z_{s_n}} \left(\int_{\Delta_n} \cos(kl_n) dl_n \right) (\cos\theta) r_n e^{j2(n-1)\alpha} \right\} \right|^2, \quad (3)$$

where α is the inter-element space delay of incident wave along array axis and r_n is the reflection coefficient of n^{th} dipole, the magnitude of which is determined by the mismatch between the impedances of dipoles and the impedance of the additional line (Fig. 1) connecting the dipole terminals to the inputs of phase-shifters,

$$r_n = \frac{Z_{a_n} - Z'_0}{Z_{a_n} + Z'_0}. \quad (4)$$

Here, Z'_0 is the impedance of the extra component (assumed to be the same as the impedance of phase-shifter Z_0) and Z_{a_n} is the impedance at the n^{th} dipole terminal, computed in the presence of coupling between the dipole elements in the array. The calculation for self and mutual impedances of a dipole array with infinitesimally thin, parallel, centre-fed, unequal length dipoles is detailed in [10] and [11], respectively.

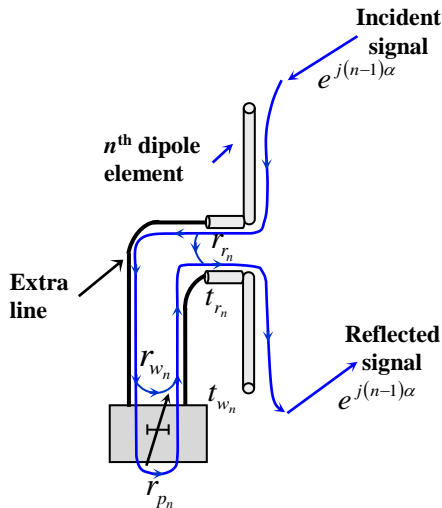


Fig. 1. The reflection and transmission coefficients till the phase-shifters.

B. Reflection at the terminals of extra component

Next, the signal would travel towards the input port of phase-shifters via the extra line. As this section of feed is assumed to be perfectly matched, its reflection coefficient will be zero. Thus, the contribution of reflections occurring at the terminals of extra line to the array RCS is:

$$\sigma_w(\theta, \phi) = 0. \quad (5)$$

C. Reflection at the phase-shifters

The signal reaching the phase-shifters will get reflected at its input ports due to the impedance mismatch. The corresponding reflection coefficient r_{p_n} is given as:

$$r_{p_n} = \frac{Z_{p_n} - Z'_0}{Z_{p_n} + Z'_0} \quad (Z'_0 = Z_0 \text{ for matched extra line}), \quad (6)$$

where Z_{p_n} is the impedance at the end terminals of the delay-lines. This yields the RCS due to the reflections at the terminals of phase-shifters as:

$$\sigma_p(\theta, \varphi) = \frac{4\pi}{\lambda^2} \left| \sum_{n=1}^N \left\{ \frac{j\eta_0}{4\lambda Z_{s_n}} \left(\int_{\Delta_n} \cos(kl_n) dl_n \right) \times \left[(\cos\theta) t_n^2 t_{w_n}^2 r_{p_n} e^{j2(n-1)\alpha} \right] \right\} \right|^2, \quad (7)$$

r_{p_n} is the reflection coefficient of n^{th} phase-shifter and t_{w_n} is the transmission coefficient of n^{th} extra line. For the matched extra line, it is always one; i.e.:

$$t_{w_n} = \sqrt{1 - r_{w_n}^2}, \quad \because r_{w_n} = 0. \quad (8)$$

D. Reflection at the coupler ports

Next level in the feed network that contributes to the RCS is the junction of phase-shifters and the input ports of couplers.

Signal reflection at the input port(s) of the couplers connected to phase-shifters:

The contribution of reflections at the input terminal of couplers connected to phase-shifters for the RCS of dipole array is given as:

$$\sigma_c(\theta, \varphi) = \frac{4\pi}{\lambda^2} \left| \sum_{n=1}^N \left\{ \frac{j\eta_0}{4\lambda Z_{s_n}} \left(\int_{\Delta_n} \cos(kl_n) dl_n \right) \times \left[(\cos\theta) t_n^2 t_{w_n}^2 t_{p_n}^2 r_c e^{j2(n-1)\alpha} \right] \right\} \right|^2, \quad (9)$$

where t_{p_n} is the transmission coefficient of n^{th} phase-shifter, r_c is the reflection coefficient of coupler port connected to the end of phase-shifter

[8] and $\zeta=\alpha+\alpha_s$; α_s is the inter-element phase to scan beam along the array axis. However, the calculations of the coefficients at this level depend on the type of feed. This is because, the couplers in parallel feed interact with multiple antenna elements, unlike in series feed [11].

Signal reflection at other coupler ports

The signal that enters through the input port of

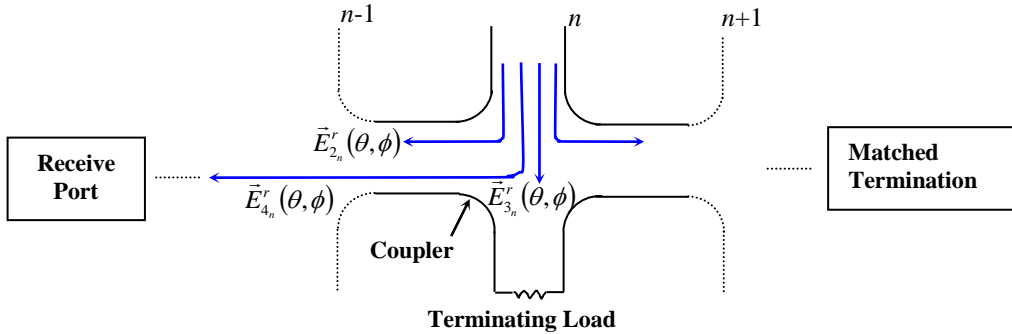


Fig. 2. Signal paths and the corresponding reflected fields at n^{th} dipole element.

The RCS due to the couplers in series feed network is expressed as:

$$\sigma_s(\theta, \varphi) = \frac{4\pi}{\lambda^2} \sum_{n=1}^N \left[\frac{j\eta_0}{4\lambda Z_{s_n}} \left(\int_{\Delta_n} \cos(kl_n) dl_n \right)^2 \times \left. \begin{aligned} &(\cos\theta) \left\{ \vec{E}_{1_n}^r(\theta, \varphi) + \vec{E}_{2_n}^r(\theta, \varphi) \right\} \\ &+ \vec{E}_{3_n}^r(\theta, \varphi) + \vec{E}_{4_n}^r(\theta, \varphi) \end{aligned} \right\} \right]^2 \quad (10)$$

where $\vec{E}_{1_n}^r(\theta, \varphi)$ is the reflected field at n^{th} dipole arising from the signal propagating towards the next antenna element, given by:

$$\vec{E}_{1_n}^r(\theta, \varphi) = \left[\begin{aligned} &t_r t_w t_p r_n j c_n e^{j(n-1)\zeta} \times \\ &\sum_{m=n+1}^N \left(t_r t_w t_p j c_m e^{j(m-1)\zeta} \prod_{i=n}^{m-1} t_{c_i} e^{j\psi} \right) \end{aligned} \right]. \quad (11)$$

$\vec{E}_{2_n}^r(\theta, \varphi)$ is the reflected field at n^{th} dipole arising from the signal propagating towards previous antenna element(s) in the array, given by:

$$\vec{E}_{2_n}^r(\theta, \varphi) = \left[\begin{aligned} &t_r t_w t_p j c_n e^{j(n-1)\zeta} \times \\ &\sum_{m=1}^{n-1} t_r t_w t_p r_m j c_m e^{j(m-1)\zeta} \prod_{i=m}^{n-1} t_{c_i} e^{j\psi} \end{aligned} \right]. \quad (12)$$

$\vec{E}_{3_n}^r(\theta, \varphi)$ is the reflected field at n^{th} dipole due to signal propagating towards the terminating load,

coupler, gets reflected within the coupler. Since the geometrical arrangement and the nature of couplers differ for the series and parallel feed network, the RCS formulation also varies.

For series feed network: Fig. 2 illustrates the signal paths and the corresponding reflected fields at n^{th} dipole in a series-fed dipole array.

given by:

$$\vec{E}_{3_n}^r(\theta, \varphi) = r_n t_r^2 t_w^2 t_p^2 t_c^2 e^{j2(n-1)\zeta}, \quad (13)$$

and $\vec{E}_{4_n}^r(\theta, \varphi)$ is the reflected field at n^{th} dipole due to the signal propagating towards the receive port, given by:

$$\vec{E}_{4_n}^r(\theta, \varphi) = \left[r_n t_r^2 t_w^2 t_p^2 (j c_n)^2 e^{j2(n-1)\zeta} \left(\prod_{i=1}^{n-1} t_{c_i} e^{j\psi} \right)^2 \right]. \quad (14)$$

It can be noted that the mutual impedance is included in the calculation of coefficients (c , t_c , t_s) of the coupler level in the feed network.

For parallel feed network: The RCS due to the first level of coupler is expressed as:

$$\sigma_{sd_1}(\theta, \varphi) = \frac{4\pi}{\lambda^2} \sum_{n=1,3,\dots}^{N-1} \left\{ \begin{aligned} &\frac{j\eta_0}{4\lambda Z_{s_n}} \left(\int_{\Delta_n} \cos(kl_n) dl_n \right)^2 \times \\ &(\cos\theta) \vec{E}_n^r(\theta, \varphi) + \frac{j\eta_0}{4\lambda Z_{s_{(n+1)}}} \times \\ &\left(\int_{\Delta_{(n+1)}} \cos(kl_{(n+1)}) dl_{(n+1)} \right)^2 (\cos\theta) \vec{E}_{(n+1)}^r(\theta, \varphi) \end{aligned} \right\}^2, \quad (15)$$

where

$$\vec{E}_{n_1}^r(\theta, \varphi) = t_{\xi} t_{w_n} t_{p_n} e^{j(n-1)\zeta} \left\{ \begin{array}{l} r_{s_{1i}} c_{1i} e^{j\psi} \left(c_{1i} e^{j\psi} t_{\xi} t_{w_n} t_{p_n} e^{j(n-1)\zeta} \right. \\ \left. + t_{\xi_{n+1}} t_{w_{n+1}} t_{p_{n+1}} e^{j\psi} t_{c_{1i}} \right) \\ + r_{d_{1i}} t_{c_{1i}} \left(t_{\xi} t_{w_n} t_{p_n} e^{j(n-1)\zeta} t_{c_{1i}} \right. \\ \left. + t_{\xi_{n+1}} t_{w_{n+1}} t_{p_{n+1}} e^{j\psi} c_{1i} e^{j\psi} \right) \end{array} \right\},$$

$$\vec{E}_{(n+1)_1}^r(\theta, \varphi) = t_{\xi_{n+1}} t_{w_{n+1}} t_{p_{n+1}} e^{j\psi} \left\{ \begin{array}{l} r_{s_{1i}} t_{c_{1i}} \left(t_{\xi} t_{w_n} t_{p_n} e^{j(n-1)\zeta} c_{1i} e^{j\psi} \right. \\ \left. + t_{c_{1i}} t_{\xi_{n+1}} t_{w_{n+1}} t_{p_{n+1}} e^{j\psi} \right) \\ + r_{d_{1i}} c_{1i} e^{j\psi} \left(t_{\xi} t_{w_n} t_{p_n} e^{j(n-1)\zeta} t_{c_{1i}} \right. \\ \left. + t_{\xi_{n+1}} t_{w_{n+1}} t_{p_{n+1}} e^{j\psi} c_{1i} e^{j\psi} \right) \end{array} \right\},$$

and the RCS due to the first level coupler is:

$$\sigma_{sd_1}(\theta, \varphi) = \frac{4\pi}{\lambda^2} \sum_{n=1,3,\dots}^{N-3} \left\{ \begin{array}{l} \left(\frac{j\eta_0}{4\lambda Z_{s_n}} \int_{\Delta_n} \cos(kl_n) dl_n \right)^2 (\cos\theta) \times \\ \vec{E}_{n_2}^r(\theta, \varphi) + \frac{j\eta_0}{4\lambda Z_{s_{(n+1)}}} \left(\int_{\Delta_{(n+1)}} \cos(kl_{(n+1)}) dl_{(n+1)} \right)^2 \times \\ (\cos\theta) \vec{E}_{(n+1)_2}^r(\theta, \varphi) + \frac{j\eta_0}{4\lambda Z_{s_{(n+2)}}} \times \\ \left(\int_{\Delta_{(n+2)}} \cos(kl_{(n+2)}) dl_{(n+2)} \right)^2 (\cos\theta) \vec{E}_{(n+2)_2}^r(\theta, \varphi) \\ + \frac{j\eta_0}{4\lambda Z_{s_{(n+3)}}} \left(\int_{\Delta_{(n+3)}} \cos(kl_{(n+3)}) dl_{(n+3)} \right)^2 \times \\ (\cos\theta) \vec{E}_{(n+3)_2}^r(\theta, \varphi) \end{array} \right\}^2, \quad (16)$$

where, the reflected fields are expressed as

$$\vec{E}_{n_2}^r(\theta, \varphi) = t_{\xi} t_{w_n} t_{p_n} e^{j(n-1)\zeta} c_{1i} e^{j\psi} t_{s_{1i}} \times$$

$$\left[\begin{array}{l} r_{s_{2i}} c_{2i} e^{j\psi} \left\{ \begin{array}{l} t_{\xi} t_{w_n} t_{p_n} e^{j(n-1)\zeta} c_{1i} e^{j\psi} t_{s_{1i}} c_{2i} e^{j\psi} + t_{\xi_{n+1}} t_{w_{n+1}} t_{p_{n+1}} \\ e^{j\psi} t_{c_{1i}} t_{s_{1i}} t_{c_{2i}} e^{j\psi} + t_{\xi_{n+2}} t_{w_{n+2}} t_{p_{n+2}} e^{j(n+1)\zeta} c_{1(i+1)} e^{j\psi} \\ t_{c_{1(i+1)}} t_{c_{2i}} + t_{\xi_{n+3}} t_{w_{n+3}} t_{p_{n+3}} e^{j(n+2)\zeta} t_{c_{1(i+1)}} t_{s_{1(i+1)}} t_{c_{2i}} \end{array} \right\} \\ + r_{d_{2i}} t_{c_{2i}} \left\{ \begin{array}{l} t_{\xi} t_{w_n} t_{p_n} e^{j(n-1)\zeta} c_{1i} e^{j\psi} t_{s_{1i}} t_{c_{2i}} + t_{\xi_{n+1}} t_{w_{n+1}} t_{p_{n+1}} e^{j\psi} t_{c_{1i}} \\ t_{s_{1i}} t_{c_{2i}} + t_{\xi_{n+2}} t_{w_{n+2}} t_{p_{n+2}} e^{j(n+1)\zeta} c_{1(i+1)} e^{j\psi} t_{s_{1(i+1)}} c_{2i} e^{j\psi} \\ + t_{\xi_{n+3}} t_{w_{n+3}} t_{p_{n+3}} e^{j(n+2)\zeta} t_{c_{1(i+1)}} t_{s_{1(i+1)}} c_{2i} e^{j\psi} \end{array} \right\} \end{array} \right], \quad (17a)$$

$$\vec{E}_{(n+1)_2}^r(\theta, \varphi) = t_{\xi_{n+1}} t_{w_{n+1}} t_{p_{n+1}} e^{j\psi} t_{c_{1i}} t_{s_{1i}} \times$$

$$\left[\begin{array}{l} r_{s_{2i}} c_{2i} e^{j\psi} \left\{ \begin{array}{l} t_{\xi} t_{w_n} t_{p_n} e^{j(n-1)\zeta} c_{1i} e^{j\psi} t_{s_{1i}} c_{2i} e^{j\psi} + \\ t_{\xi_{n+1}} t_{w_{n+1}} t_{p_{n+1}} e^{j\psi} t_{c_{1i}} t_{s_{1i}} c_{2i} e^{j\psi} + \\ t_{\xi_{n+2}} t_{w_{n+2}} t_{p_{n+2}} e^{j(n+1)\zeta} c_{1(i+1)} e^{j\psi} t_{s_{1(i+1)}} \\ \times t_{c_{2i}} + t_{\xi_{n+3}} t_{w_{n+3}} t_{p_{n+3}} e^{j(n+2)\zeta} t_{c_{1(i+1)}} t_{s_{1(i+1)}} t_{c_{2i}} \end{array} \right\} \end{array} \right],$$

$$+ r_{d_{2i}} t_{c_{2i}} \left\{ \begin{array}{l} t_{\xi} t_{w_n} t_{p_n} e^{j(n-1)\zeta} c_{1i} e^{j\psi} t_{s_{1i}} t_{c_{2i}} \\ + t_{\xi_{n+1}} t_{w_{n+1}} t_{p_{n+1}} e^{j\psi} t_{c_{1i}} t_{s_{1i}} t_{c_{2i}} + \\ t_{\xi_{n+2}} t_{w_{n+2}} t_{p_{n+2}} e^{j(n+1)\zeta} c_{1(i+1)} e^{j\psi} t_{s_{1(i+1)}} c_{2i} e^{j\psi} \\ + t_{\xi_{n+3}} t_{w_{n+3}} t_{p_{n+3}} e^{j(n+2)\zeta} t_{c_{1(i+1)}} t_{s_{1(i+1)}} c_{2i} e^{j\psi} \end{array} \right\}, \quad (17b)$$

$$\vec{E}_{(n+2)_2}^r(\theta, \varphi) = t_{\xi_{n+2}} t_{w_{n+2}} t_{p_{n+2}} e^{j(n+1)\zeta} c_{1(i+1)} e^{j\psi} t_{s_{1(i+1)}} \times$$

$$\left[\begin{array}{l} r_{s_{2i}} t_{c_{2i}} \left\{ \begin{array}{l} t_{\xi} t_{w_n} t_{p_n} e^{j(n-1)\zeta} c_{1i} e^{j\psi} t_{s_{1i}} c_{2i} e^{j\psi} + t_{\xi_{n+1}} t_{w_{n+1}} \\ \times t_{p_{n+1}} e^{j\psi} t_{c_{1i}} t_{s_{1i}} c_{2i} e^{j\psi} + t_{\xi_{n+2}} t_{w_{n+2}} t_{p_{n+2}} e^{j(n+1)\zeta} \\ \times e^{j\psi} c_{1(i+1)} t_{s_{1(i+1)}} t_{c_{2i}} + t_{\xi_{n+3}} t_{w_{n+3}} t_{p_{n+3}} e^{j(n+2)\zeta} \\ \times t_{c_{1(i+1)}} t_{s_{1(i+1)}} t_{c_{2i}} \end{array} \right\} \\ + r_{d_{2i}} c_{2i} e^{j\psi} \left\{ \begin{array}{l} t_{\xi} t_{w_n} t_{p_n} e^{j(n-1)\zeta} c_{1i} e^{j\psi} t_{s_{1i}} t_{c_{2i}} + t_{\xi_{n+1}} t_{w_{n+1}} \\ \times t_{p_{n+1}} e^{j\psi} t_{c_{1i}} t_{s_{1i}} t_{c_{2i}} + t_{\xi_{n+2}} t_{w_{n+2}} t_{p_{n+2}} e^{j(n+1)\zeta} \\ \times e^{j\psi} c_{1(i+1)} t_{s_{1(i+1)}} c_{2i} e^{j\psi} + t_{\xi_{n+3}} t_{p_{n+3}} e^{j(n+2)\zeta} \\ \times t_{c_{1(i+1)}} t_{s_{1(i+1)}} c_{2i} e^{j\psi} \end{array} \right\} \end{array} \right], \quad (17c)$$

$$\vec{E}_{(n+3)_2}^r(\theta, \varphi) = t_{\xi_{n+3}} t_{w_{n+3}} t_{p_{n+3}} e^{j(n+2)\zeta} t_{c_{1(i+1)}} t_{s_{1(i+1)}} \times$$

$$\left[\begin{array}{l} r_{s_{2i}} t_{c_{2i}} \left\{ \begin{array}{l} t_{\xi} t_{w_n} t_{p_n} e^{j(n-1)\zeta} c_{1i} e^{j\psi} t_{s_{1i}} c_{2i} e^{j\psi} + t_{\xi_{n+1}} t_{w_{n+1}} \\ \times t_{p_{n+1}} e^{j\psi} t_{c_{1i}} t_{s_{1i}} c_{2i} e^{j\psi} + t_{\xi_{n+2}} t_{w_{n+2}} t_{p_{n+2}} \\ \times e^{j(n+1)\zeta} c_{1(i+1)} e^{j\psi} t_{s_{1(i+1)}} t_{c_{2i}} + t_{\xi_{n+3}} t_{w_{n+3}} t_{p_{n+3}} \times \\ e^{j(n+2)\zeta} t_{c_{1(i+1)}} t_{s_{1(i+1)}} t_{c_{2i}} \end{array} \right\} \\ + r_{d_{2i}} c_{2i} e^{j\psi} \left\{ \begin{array}{l} t_{\xi} t_{w_n} t_{p_n} e^{j(n-1)\zeta} c_{1i} e^{j\psi} t_{s_{1i}} t_{c_{2i}} + t_{\xi_{n+1}} t_{w_{n+1}} \\ \times t_{p_{n+1}} e^{j\psi} t_{c_{1i}} t_{s_{1i}} t_{c_{2i}} + t_{\xi_{n+2}} t_{w_{n+2}} t_{p_{n+2}} e^{j(n+1)\zeta} \\ \times c_{1(i+1)} e^{j\psi} t_{s_{1(i+1)}} c_{2i} e^{j\psi} + t_{\xi_{n+3}} t_{w_{n+3}} t_{p_{n+3}} \\ \times e^{j(n+2)\zeta} t_{c_{1(i+1)}} t_{s_{1(i+1)}} c_{2i} e^{j\psi} \end{array} \right\} \end{array} \right]. \quad (17d)$$

The total RCS of unequal length dipole array with mutual coupling effect for series feed is given by:

$$\sigma(\theta, \varphi) = \sigma_r(\theta, \varphi) + \sigma_p(\theta, \varphi) + \sigma_c(\theta, \varphi) + \sigma_s(\theta, \varphi), \quad (18)$$

and for parallel feed network till q level of couplers, the RCS of dipole array is expressed as:

$$\sigma(\theta, \varphi) = \sigma_r(\theta, \varphi) + \sigma_p(\theta, \varphi) + \sigma_c(\theta, \varphi) + \sum_{i=1}^q \sigma_{sd_i}(\theta, \varphi). \quad (19)$$

III. RESULTS AND DISCUSSION

The RCS estimation of uniform linear dipole array includes mutual coupling effect. Multiple

reflections and edge effects are ignored. It is assumed that the extra component, connecting antenna element with the phase shifter in the feed network is perfectly matched.

A. RCS estimation of series-fed dipole array

First, the RCS patterns of equal and unequal length dipole arrays are compared. Two 30-element arrays of equal length $\lambda/3$ and $\lambda/4$ dipoles are considered. The $\lambda/4$ and $\lambda/3$ length dipoles are arranged alternately, so as to form an unequal length dipole array.

In all cases, the staggered height of the dipoles is taken as $\lambda/3$ below and above the reference plane for odd and even-positioned dipoles, respectively. Other design parameters are taken as $d=0.25\lambda$, $Z_0=100\Omega$, $Z_t=200\Omega$. The elements are excited as per Taylor amplitude distribution (-45 dB SLL; $\bar{n}=4$). Figure 3 shows that the level of RCS is minimum for $\lambda/4$ equal-length dipole array and maximum for $\lambda/3$ equal-length dipole array. On the other hand, the RCS level of unequal length dipole array lies in between the levels of two equal-length dipole array, for major portion of the pattern. However, the RCS level of unequal length dipole array is observed to increase drastically for the aspect angles beyond $\pm 50^\circ$. It can be inferred that the optimization of dipole lengths could facilitate the reduction and control of the array RCS.

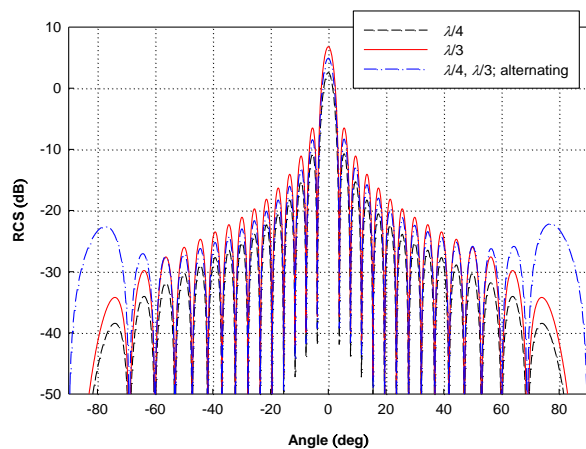


Fig. 3. Broadside RCS of equal and unequal length series-fed dipole array.

Next, the effect of mutual coupling on the scanned array RCS is demonstrated. An array of 20 thin-wire (radius= 10^{-5} λ) dipoles with

alternative length of $\lambda/2$ and $\lambda/3$ is considered. The staggered height of dipoles *w.r.t.* reference plane is taken as $-\lambda/4$ for odd-positioned elements and $\lambda/6$ for even-positioned elements. Other parameters are $d=0.2\lambda$, $Z_0=100\Omega$, $Z_t=40\Omega$; with cosine squared on pedestal element excitation. Figure 4 compares the scanned ($\theta_s=50^\circ$) RCS pattern of this array with and without mutual coupling effect. It can be observed that the scanned RCS of dipole array differ significantly for with and without mutual coupling cases. The variation in the scanned RCS pattern further increases for larger values of scan angle. This may be due to the inter-element interactions that vary the terminal impedances of the dipole elements, and hence the reflections within the array system and the RCS.

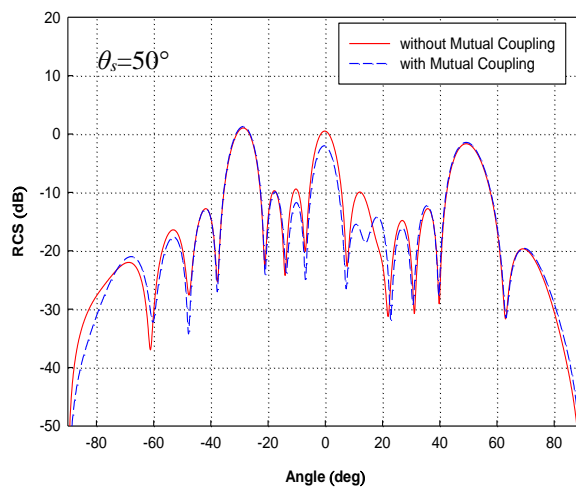


Fig. 4. Scanned ($\theta_s=50^\circ$) RCS patterns of 20-element unequal length linear dipole array, with and without mutual coupling effect.

Next, the effect of varying the terminal impedances of the coupler ports on the RCS pattern of 25-element unequal length uniform ($d=0.2\lambda$) dipole array is analyzed. The dipoles in the array are taken to be of lengths $\lambda/3$ and $\lambda/2$ at odd- and even-positions of the array, respectively. The staggered heights of the elements *w.r.t.* reference plane are taken to be $\lambda/4$ and $-\lambda/3$ alternately. The amplitude distribution is Dolph-Chebyshev with -40 dB Sidelobe Level (SLL). The characteristic impedance is 75Ω . Figure 5 shows the broadside RCS pattern for the array when the terminating impedance is varied from 0Ω to 200Ω .

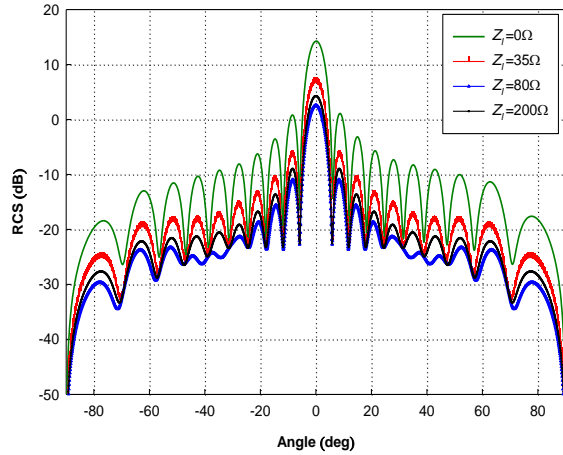


Fig. 5. Dependence of RCS pattern of a 25-element unequal-length dipole array on the terminal impedance.

It is seen that the RCS levels decrease as the terminal impedance value increases from 0Ω to 35Ω and further to 80Ω . However, for terminal impedance of 200Ω , the RCS level shows rise. This indicates that the decrease in RCS with variation of impedance terminating the coupler ports possess a limit. On reaching the limiting value of terminating impedance, the RCS level starts increasing with the load impedance Z_l . This effect is similar to the case of equal length array. This feature of terminating load dependence can be exploited for array RCS control.

B. RCS estimation of parallel-fed dipole array

The RCS of two parallel-fed linear dipole arrays, each with 32-element equal and unequal-length dipoles is computed. The dipole lengths are taken as $\lambda/2$, for equal-length array, whereas, random for unequal-length dipole array. The dipoles at odd and even positions in the array are arranged at heights of $\lambda/4$ below and above the reference line, respectively. The RCS patterns of these dipole arrays including mutual coupling effect are compared in Fig. 6. The dipoles are spaced 0.4λ apart and are excited by uniform unit amplitude distribution.

The characteristic impedance and load impedance are taken as 75Ω and 20Ω , respectively. Scattering is considered till second level of couplers. It is apparent that the RCS pattern of $\lambda/2$ dipole array has definite lobes *viz.* specular lobe ($\theta=0^\circ$), lobes due to first level

coupler mismatches ($\theta=\pm 38^\circ$) and lobes due to the mismatches at second level of couplers ($\theta=\pm 17^\circ$). However, for the random length dipole array considered, it is difficult to identify any other lobe, except for the specular lobe. Moreover, the RCS level in case of random dipoles is observed to be less than that for $\lambda/2$ array. Although, at other aspect angles, the level of scattering in the random-length array exceeds that of equal-length array, the level is well below 0 dB , and hence less significant.

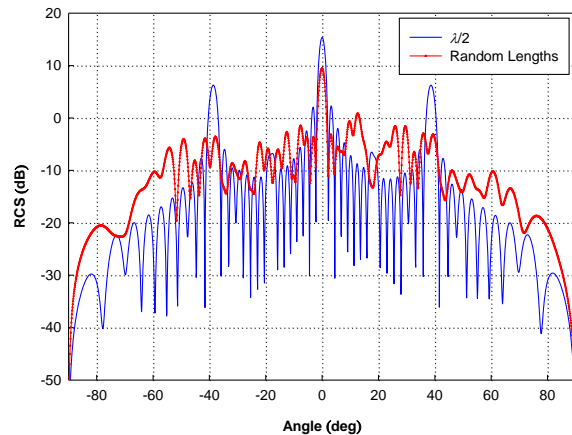


Fig. 6. Comparison of broadside RCS pattern of equal and random length dipole arrays.

Next, the mutual coupling effect in unequal-length parallel-fed dipole array is discussed. The dipole array consists of 16-elements with odd-positioned dipole lengths ($=\lambda/3+(n-1)\times 0.01\lambda/3$). The dipole lengths at the even-positions decrement in the steps of $0.01\lambda/2$, starting from $\lambda/2$. All the dipoles are at the height of $\lambda/4$ above the reference plane. The inter-element spacing is taken as 0.4λ . The characteristic and load impedances are 75Ω and 200Ω , respectively. Figure 7 shows the broadside RCS pattern obtained, for with and without mutual coupling cases. The scattering till first level of couplers is considered. In order to analyze the effect of terminating impedance on the array RCS, a 64-element array is considered, in which the dipoles of lengths $\lambda/3$ and $\lambda/2$ are arranged alternately with staggered heights of $\lambda/4$ below and above the reference plane, respectively. The spacing between elements is 0.4λ . The influence of impedance terminating the coupler ports on the RCS pattern of such an unequal length parallel-in-echelon dipole array is shown in Fig. 8.

Dipoles are excited by uniform distribution and the characteristic impedance is taken as 75Ω .

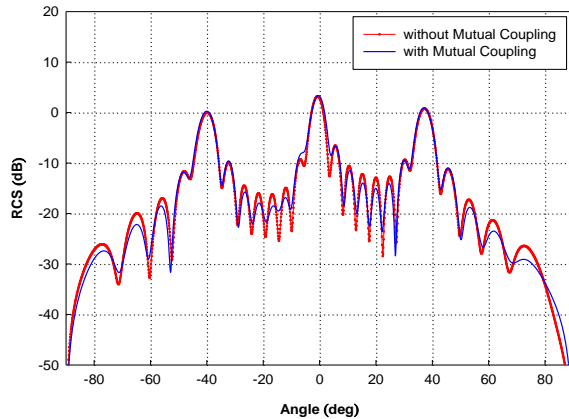


Fig. 7. Broadside RCS pattern of 16-element unequal length parallel-fed dipole array.

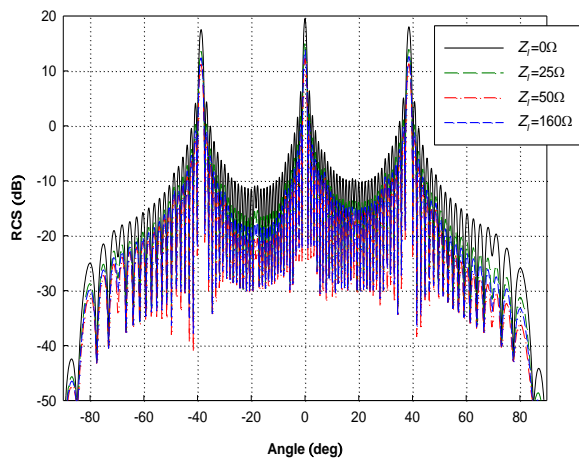


Fig. 8. Effect of varying the terminating impedances on the RCS pattern of 64-element unequal length parallel-in-echelon dipole array.

The scattering effect is considered till second level of couplers. It is observed that the RCS level is maximum for 0Ω termination and decreases as the impedance is increased to 25Ω and 50Ω . However, for 160Ω termination, the level of RCS lobes increases. This emphasizes that the concept of limiting impedance holds good, irrespective of the design parameters including length of dipoles, scan angle, amplitude distribution and the feed.

IV. CONCLUSION

This paper presents an analytical estimation of the RCS of arbitrary linear dipole array with

uniform spacing. The formulation holds good for both unequal and equal length dipole arrays arranged in any random configuration. The reflections within the antenna system and the effects of mutual coupling between array elements are taken into account. The scattering due to higher order reflections is neglected and the computations are restricted till second level of couplers. The variation in the dipole lengths is shown to affect the RCS pattern of the array significantly. The dipole length could be a potential parameter for the reduction of array RCS. Moreover, the mutual coupling affects the RCS pattern for both types of feeds. The variation in RCS pattern becomes further noticeable as the scan angle of array increases, irrespective of any other design criteria. The terminating impedance is another important parameter that can be exploited for RCS control. There is a limiting value of terminating impedance beyond which RCS value of phased array increases. In broad sense, the effect of varying the design parameters on overall RCS pattern is similar in both equal- and unequal-length dipole arrays.

REFERENCES

- [1] S. Hu, H. Chen, C. L. Law, Z. Shen, L. Zhu, W. Zhang, and W. Dou, "Backscattering cross section of ultra-wideband antennas," *IEEE Ant. & Wireless Propag. Letters*, vol. 6, pp. 70-73, 2007.
- [2] D. C. Jenn and S. Lee, "In-band scattering from arrays with series feed networks," *IEEE Trans. Ant. & Propag.*, vol. 43, pp. 867-873, August 1995.
- [3] J. Ling, S. X. Gong, B. Lu, H. W. Yuan, W. T. Wang, and S. Liu, "A microstrip printed dipole antenna with UC-EBG ground for RCS reduction," *JEWA*, vol. 23, pp. 607-616, 2009.
- [4] Y. Liu and L. You, "Research on the estimation and reduction measures of antenna mode RCS of airborne phased array," *Proc. IEEE 4th Intl. Symp. on Microwave, Ant. Propag. and EMC Tech. for Wireless Comm.*, China, pp. 79-82, November 2011.
- [5] Y. Liao, S. Yang, H. Ma, and Y. Hou, "Research on scattering property of finite dipole array," *Proc. of 6th Int. Conf. ITS Telecomm.*, Chengdu, China, pp. 412-415, June 2006.
- [6] L. Zengrui, W. Junhong, L. Limei, and Z. Xueqin, "Study on the scattering property of the impedance terminated dipole array with finite reflector by FDTD method," *IEEE Int. Sym. on Microwave, Ant. Propag. and EMC Tech. for Wireless Comm.*, China, pp. 1003-1007, August 16-17, 2007.

- [7] D. C. Jenn and V. Flokas, "In-band scattering from arrays with parallel feed networks," *IEEE Trans. Ant. & Propag.*, vol. 44, pp. 172-178, February 1996.
- [8] H. L. Sneha, H. Singh, and R. M. Jha, "Mutual coupling effects for radar cross section (RCS) of a series-fed dipole antenna array," *Int. J. Ant. & Propag.*, vol. 2012, p. 20, August 2012.
- [9] H. L. Sneha, H. Singh, and R. M. Jha, "Scattering analysis of an unequal-length dipole array in the presence of mutual coupling," *IEEE Ant. and Propag. Mag.*, vol. 55, pp. 333-351, August 2013.
- [10] C. A. Balanis, "Antenna theory, analysis and design," *New Jersey: John Wiley & Sons*, ISBN: 0-471-66782-X, p. 1117, 2005.
- [11] H. E. King, "Mutual impedance of unequal-length antennas in echelon," *IRE Trans. Ant. & Propag.*, vol. 5, pp. 306-313, July 1957.



H. L. Sneha obtained her B.E. (ECE) in 2010 from Visvesvaraya Technological University, (Belgaum), Karnataka. She worked as a NALTech Project Engineer and Project Graduate Trainee at the Centre for Electromagnetics (CEM) of CSIR-National Aerospace Laboratories, Bangalore, India. Her research interests include Radar Cross Section (RCS) of phased arrays. Sneha has co-authored twelve scientific research papers and technical reports.



Hema Singh is currently working as a Senior Scientist at the Centre for Electromagnetics of CSIR-National Aerospace Laboratories, Bangalore, India. Earlier, she was Lecturer in EEE, BITS, Pilani, India. She obtained her Ph.D. degree in Electronics Engineering from IIT-BHU, Varanasi, India. Her active areas of research are CEM for Aerospace Applications, Phased Arrays, and Radar Cross Section (RCS) Studies. Singh has co-authored one book chapter, and over 110 scientific research papers and technical reports.



Rakesh Mohan Jha is currently a Chief Scientist & Head, at the Centre for Electromagnetics, CSIR-National Aerospace Laboratories, Bangalore. Jha obtained his B.E. and M.Sc. degrees (Physics) from BITS, Pilani (Rajasthan) in 1982. He obtained his Ph.D. (Eng.) degree from the Department of Aerospace Engineering, of Indian Institute of Science, Bangalore in 1989, in the area of Computational Electromagnetics for Aerospace Applications. Jha was a SERC (UK) Visiting Post-Doctoral Research Fellow at the University of Oxford, Department of Engineering Science in 1991. He worked as an Alexander von Humboldt (AvH) Fellow at the Institute for High-Frequency Techniques and Electronics of the University of Karlsruhe, Germany (1992-1993, 1997). He was awarded Sir C.V. Raman Award for Aerospace Engineering for the Year 1999. Jha was elected Fellow of INAE (FNAE) in 2010, for his contributions to the EM Applications to Aerospace Engineering. He is also the Fellow of IETE and Distinguished Fellow of ICCES. Jha has authored or co-authored more than four hundred scientific research papers and technical reports.

A Novel Dual-Mode Wideband Band Pass Filter

A. Ahmadi¹, S. V. Makki², A. Lalbakhsh¹, and S. Majidifar³

¹Department of Electrical Engineering, Kermanshah Branch
Islamic Azad University, Kermanshah, Iran
aahmadi70@gmail.com, ali.lalbachsh@yahoo.com

²Department of Electrical Engineering
Razi University, Bagh-E-Abrisham, Kermanshah, Iran
v.makki@razi.ac.ir

³Department of Electrical Engineering
Kermanshah University of Technology, Kermanshah, Iran
s.majidi@kut.ac.ir

Abstract — A novel Wideband (WB) Bandpass Filter (BPF) with improved passband performance using a Defected Ground Structure (DGS) is presented in this paper. The proposed BPF is composed of two novel basic WB resonators and six Dumbbell-Shaped (DS) DGSs. By cascading resonators we can achieve better skirt characteristics, and by using DS-DGSs under interdigital coupled I/O lines we can improve the return loss within the passband. The simulated and measured results are found in good agreement with each other showing a wide passband from 4.93 to 11.62 GHz, a wide upper stopband with around 25 dB attenuation up to 20 GHz, and sharp roll-offs around 0.03 in lower and upper edges.

Index Terms — Dual mode, microstrip bandpass filter, wide passband.

I. INTRODUCTION

Microstrip filters are in high demand in modern communication systems according to their importance in selecting the desired frequency range among numerous neighbor bands, and also suppressing the undesired harmonics [1-7]. In the front-end of the Ultra-Wideband (UWB) systems, a small circuit size, high selectivity, and wide stopband microwave Bandpass Filters (BPF) are essential to provide better frequency responses.

Since the federal communications commission has allocated 7.5 GHz of spectrum for unlicensed use of UWB devices [8], many attempts have been made to produce various kinds of wideband BPFs [9-19]. These wideband filters can be divided into two basic types. The first type is based on the design of a single Stepped Impedance Resonator (SIR) and strong I/O coupling, which is named as Multiple Mode Resonator (MMR) [9-10]. The second UWB filter was initially presented as an optimum distributed highpass filter [11], but some sections were added to the highpass filter in order to create transmission nulls which were used to control upper passband edge [12-13]. In [14], a single modified square slot-line resonator and parallel microstrip feed lines have been used for UWB filter design. Here, the improved upper stopband has been obtained by exploiting the frequency dispersive coupling behavior between the feed lines and the resonator. A wideband bandpass filter has been designed in [15], using Composite Right/Left Handed (CRLH) transmission lines and floating slot in the ground plane in order to get high coupling in comparison to conventional edge coupled microstrip line. In [16], parallel coupled line filters have been constructed, employing tight-coupling structures; however, the reported FBW only achieved around 64% of the bandwidth. Wideband bandpass filters using multiple-mode

resonators to achieve a fractional bandwidth of 100% have been reported in [17]. However, these wideband filters suffer from some problems, such as larger size and slow rejection skirt. Although in [18-19], the authors could realize sharp roll-off and good stopband characteristic using a new fractal geometry, the proposed filter did not provide wide passband. In this paper, a novel dual-mode wide band bandpass filter using symmetric interdigital coupled Input/Output (I/O) lines with the patterns of DGS is proposed. The mechanism of the proposed dual-mode resonator filter is investigated in detail using even and odd-mode analysis. Finally, this proposed filter is verified by simulation and measurement.

II. ANALYSIS AND DESIGN

A. Structure and equivalent circuit of the proposed basic wide band resonator

Figure 1 (a) shows the schematic diagram of the proposed basic WB resonator. The dimensions of the basic resonator in Fig. 1 (a) are: $L1 = 7.43$, $L2 = 6.38$, $L3 = 4.3$, $W1 = 0.11$, $W2 = 0.32$, $W3 = 0.1$, $W4 = 0.1$, $W5 = 0.56$ (all in millimeter). The equivalent circuit model of the proposed resonator is shown in Fig. 1 (b), which consists of $Ls=4.6$ nH (Ls is the inductance of upper and lower inductive lines), $Lt=13.1$ nH (Lt is the inductance of central inductive line), $Cc=0.07$ pF (Cc is the coupling capacitance between these inductive lines), and $Cb=0.05$ pF (Cb is the capacitance between the edge parts of the resonators and the ground plane). The obtained values of those parameters are extracted using methods discussed in [11]. This structure is designed on RO4003 with a dielectric constant of 3.38, height of 0.508 mm, and loss tangent of 0.0021.

The simulated S-parameters of the basic resonator are shown in Fig. 1 (c). As it is shown in Fig. 1 (c), the simulated S-parameter of the designed resonator has ripple in the passband and also suffers from big return loss within the passband. For solving this problem, we proposed a Defected Microstrip Structure (DMS) to suppress unwanted ripples and decrease the return loss. Frequency responses and the layout of this structure are shown in Fig. 2. The dimensions of the layout in Fig. 2 are: $P1 = 6.8$, $P2 = 4.4$, $M1 = 0.4$, $M2 = 1$, $M3 = 0.4$, $M4 = 0.3$, $M5 = 0.63$ (all in millimeter), while the widths of lines are the same as mentioned.

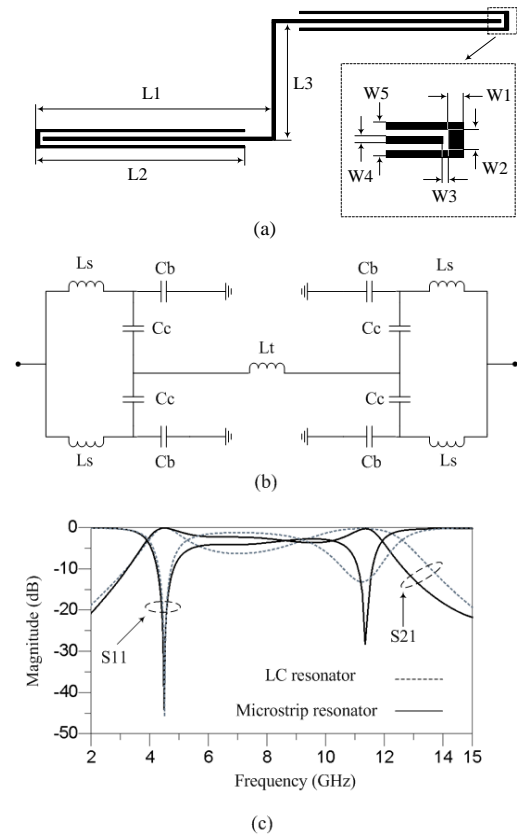


Fig. 1. Basic resonator: (a) layout, (b) LC model, and (c) frequency responses.

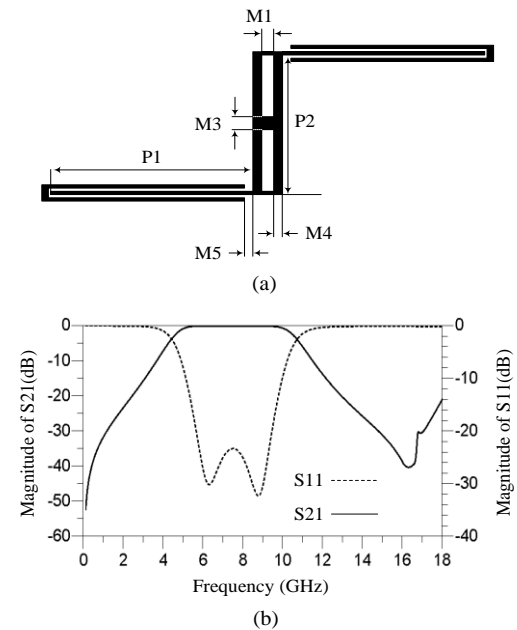


Fig. 2. Basic resonator with DMS: (a) layout, and (b) simulation results.

B. Dual mode characteristic

The resonator in Fig. 2 can be divided into two sections along the symmetric plane of the filter; an open-circuited resonator for even mode and a short-circuited for odd mode [11], as shown in Fig. 3 (a). The resonant characteristic of the resonator against the length of P2 is depicted in Fig. 3 (b). Weak coupling is applied in the simulation of decreasing the influence of the input and output lines of the resonator. As it is shown in Fig. 3 (b), resonant frequency of even modes of the resonator is mainly determined by P1 and P2. Keeping P1 stable and increasing the length of P2, the fundamental mode remains unchanged while the second resonant mode f_{even} of the resonator will move towards the fundamental mode. Thus, a dual-mode characteristic can be achieved by tuning the length of P2.

Figure 3 (c) shows the resonance frequencies of the two modes against the length of P1. The horizontal axis is the length of the left/right branch P1, and the vertical axis is the resonator frequency of the two modes. As is shown in Fig. 3 (c), when P1 varies from 3.9 mm to 9.9 mm, the resonance frequencies of the odd and even modes decrease almost linearly from 9.51 to 4.438 and 13.72 to 6.74 GHz, respectively. It is evident from Fig. 3 that the resonant frequency of the even mode is determined by both P1 and P2, while the resonant frequency of the odd mode is controlled by the length of P2. So changing the even-mode resonance frequencies will not affect the odd-mode resonance frequencies. Having this feature, the dual-mode filters with the flexible passband frequencies can be designed.

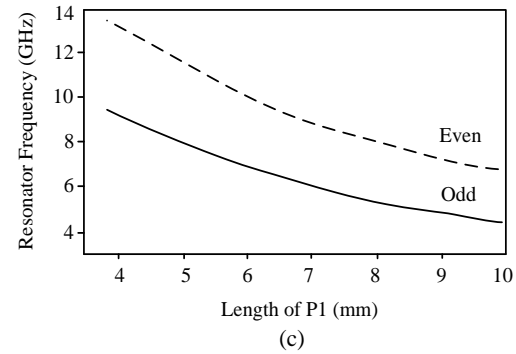
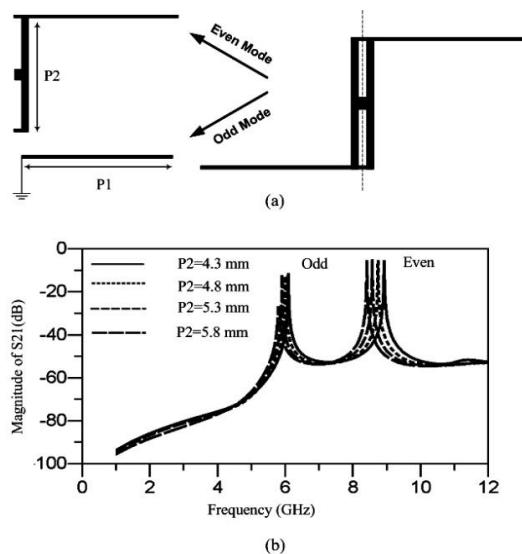


Fig. 3. (a) The configuration of the dual-mode microstrip resonator, (b) simulated resonances of the two modes against P2, and (c) simulated resonances of the two modes against P1.

C. Coupling coefficient

The coupling coefficient can be evaluated from the two dominant resonant frequencies for any two synchronously tuned coupled resonators. If f_{p1} and f_{p2} are defined to be the lower-odd mode and higher-even mode of the two resonant frequencies respectively, the coupling coefficient can be obtained by [11]:

$$M = \frac{f_{p2}^2 - f_{p1}^2}{f_{p2}^2 + f_{p1}^2} \tag{1}$$

The coupling coefficient of the proposed resonator in Fig. 2 (a) is only controlled by the width of the line in the middle of the interdigital coupled I/O lines-denoted by W4-the values of coupling coefficient M is given against the width of W4 by Fig. 4. As can be seen from this figure, by increasing the width of W4 and keeping unchanged the spaces between the coupled lines, the coupling coefficient increases.

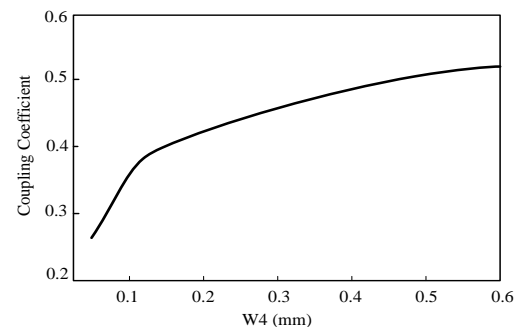


Fig. 4. Coupling coefficient of the proposed resonator versus the width of the central line.

III. FILTER DESIGN

A. Two cascaded resonators

Based on the above formulation, a bandpass filter characterizing sharp roll-off and wide bandwidth has been designed. The wide passband is realized by applying DMS, whereas the sharp roll-off is achieved by cascading two cells as illustrated in Fig. 5.

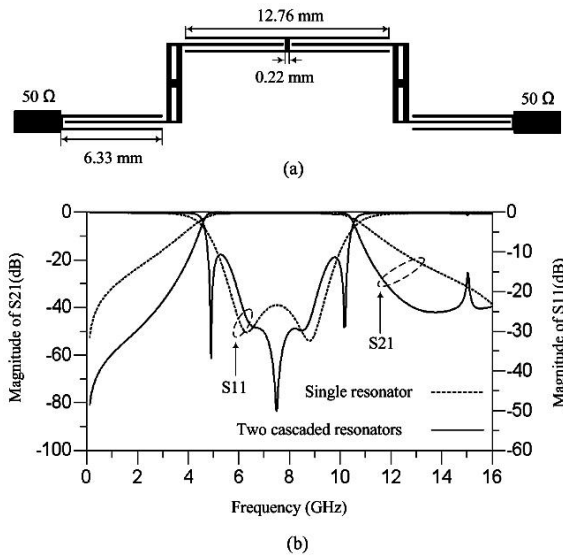


Fig. 5. Two cascaded resonators: (a) schematic, and (b) simulation.

It can be seen from Fig. 5 (b) that as a result of cascading two cells the lower and upper transition bands decrease from 2.11 and 2.3 GHz to 0.7 and 0.87 GHz, respectively, while the passband remains unchanged.

B. Applying dumbbell-shaped pattern defected ground structure

Unlike the previous researches which employed DGS to improve the stopband characteristics [20-21], here we have designed three Dumbbell-Shaped (DS) pattern Defected Ground Structure (DS-DGS) to decrease return loss within the passband.

To explain the DS-DGS effects, the LC model of this structure is extracted in Fig. 6. In this figure, the DS-DGS that is modeled by a parallel LC resonator [2], crates a transition pole. If the frequency of this pole matches with the transition zero frequency (in the passband of the proposed

WB bandpass filter), then the passband performance will improve.

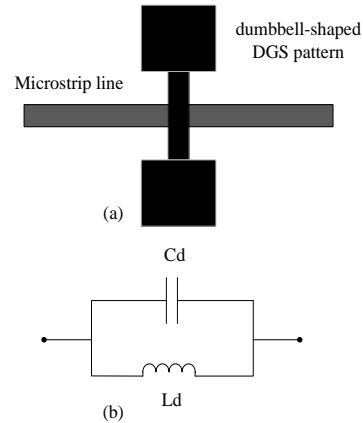


Fig. 6. DS-DGS: (a) layout, and (b) LC model.

In another approach, to explain how DS-DGS affects the return loss, one half of the basic resonator (in the presence of the DS-DGS) in Fig. 1 (a) and its equivalent circuit are studied. Introducing DS-DGS causes a reduction in electric field between edge parts of microstrip lines and ground plane, as well as between microstrip lines themselves; the former leads to a decrease in capacitance of C_b and the latter causes a reduction in the capacitance of C_c . As far as magnetic field is concerned, the proposed DS-DGS increases magnetic field around the perimeter of defected area, which results in a small increase in the inductance of L_s and L_p (L_p is the inductance of the central strip line in the half-resonator). Figure 7 shows the effects of these changes on the frequency responses of the half-resonator. As it is shown in Fig. 7, decreasing the C_b decreases return loss drastically, while decreasing C_c increases the return loss very slightly-around one dB-and increasing L_s and L_p have no effects on the return loss. The resultant of these effects causes only a reduction in return loss, while the resonance frequency keeps unchanged because the variation of C_b has no effect on resonance frequency, and shifting effects on resonance frequency caused by variation of C_c and inductors neutralize each other. It should be noticed that the dominant effect of DS-DGS decreases the electric field between ground plane and microstrip lines, which causes a huge decrease in return loss. So C_b has a dominant impact on the return loss.

Based on above explanations, three applied DS-DGS improved the return loss to around -23 dB. As it is shown in Fig. 8, the dumbbell-shaped patterns have etching dimensions of: $S1 = 0.5, S2 = 0.16, S3 = 0.39, S4 = 2.09$ (all in millimeter). The final dimensions of studied filter are tabulated in Table 1.

Table 1: Final dimension of the proposed filter (unit: mm)

| | | | | | | | |
|------|------|------|------|------|------|------|------|
| W1 | W2 | W3 | W4 | W5 | P1 | P2 | M1 |
| 0.1 | 0.31 | 0.11 | 0.10 | 0.54 | 6.34 | 3.95 | 0.59 |
| M2 | M3 | M4 | M5 | S1 | S2 | S3 | S4 |
| 0.90 | 0.40 | 0.15 | 0.61 | 0.5 | 0.16 | 0.39 | 2.09 |

IV. SIMULATION AND EXPERIMENTAL RESULTS

The proposed WB filter is fabricated on the RO4003 substrate with a dielectric constant of 3.38, a thickness of 0.508 mm and loss tangent of 0.0021. The size of the fabricated filter is $27.15 \times 10.8 \text{ mm}^2$, which corresponds to $1.12 \lambda_g \times 0.45 \lambda_g$, where λ_g is the guided wavelength at the center frequency. Measured results of the filter are characterized in an Agilent network analyzer N5230A. Figures 9 and 10 show the photograph and the simulated and measured results of the fabricated filter respectively. The measured results of the filter have 3 dB Fractional Bandwidth (FBW) of 88% at 7.57 GHz; the maximum insertion loss within the whole wide passband is 1.9 dB and the minimum return loss is around 15 dB. There is no undesired passband on the left side of the wide passband. On the right side of the passband, the 24 dB rejection band is extended from 12.27 to 20 GHz. The return loss in the stopband region is very small indicating negligibly small radiation loss. The lower transition band from 4.931 to 4.39 and the upper transition band from 11.62 to 12.27 GHz with -3 and -20 dB are 0.54 and 0.65GHz respectively, showing that the filter has excellent skirt performance.

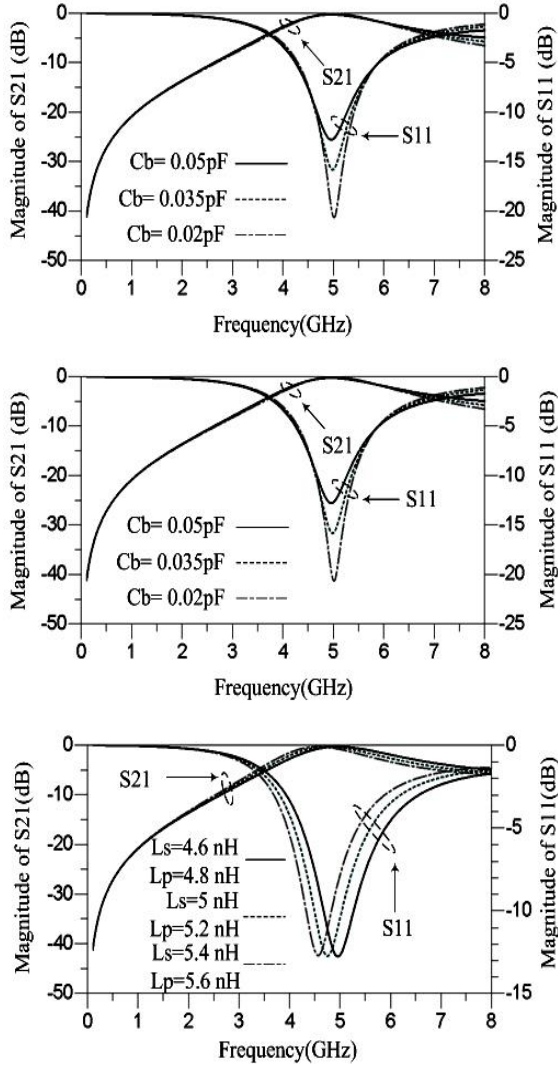


Fig. 7. Simulated results of the half-resonator model.

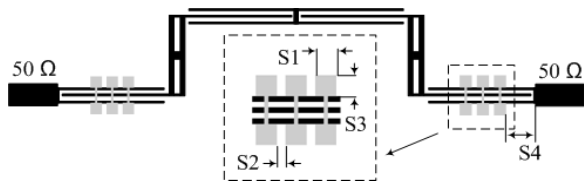
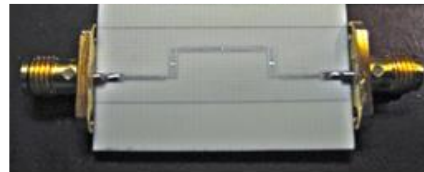


Fig. 8. Layout of the final filter.



(a)



(b)

Fig. 9. Photograph of the fabricated filter: (a) top view, and (b) bottom view.

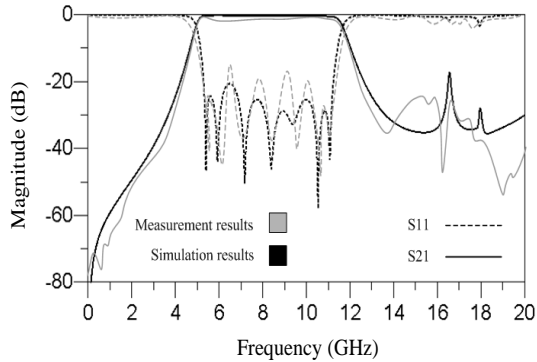


Fig. 10. Simulated and measured results.

V. DEVELOPMENT OF THE PROPOSED DESIGN

The proposed method is to scale all of the basic resonator dimensions with a constant factor. This method is suitable to make significant variations to the central frequency of the bandpass filter. Figure 11 shows the central frequency and fractional bandwidth of basic resonator as a function of scaling factor.

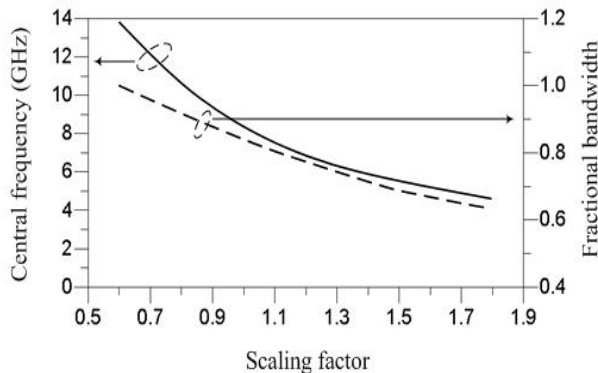


Fig. 11. The central frequency and fractional bandwidth of the basic resonator as a function of the scaling factor.

Design process of a WB bandpass filter with a different central frequency is performed by the following steps:

1. Selection of the appropriate scaling factor, according to the desired central frequency using Fig. 11.
2. Cascading two basic resonators to improve sharp roll-off, as illustrated in Fig. 5.
3. Applying dumbbell-shaped pattern defected ground structure in order to passband performance improvement.

VI. CONCLUSION

In this paper, a novel dual-mode wideband BPF based on the odd and even mode resonance frequency analysis are presented. The passband of the filter is completely adjustable and provided a sharp roll-off in the upper and lower edges. In addition, a new approach to DGS was introduced in order to improve the return loss in the passband.

REFERENCES

- [1] L. Yang, Y. Hongchun, W. Yawei, and X. Shaoqiu, "Ultra-wideband bandpass filter based on parallel-coupled microstrip lines and defected ground structure," *Appl. Comp. Electro. Soc. (ACES) Journal*, vol. 28, no. 1, pp. 21-25, January 2013.
- [2] N. M. Garmjani and N. Komjani, "Improved microstrip folded tri-section stepped impedance resonator bandpass filter using defected ground structure," *Appl. Comp. Electro. Soc. (ACES) Journal*, vol. 25, no. 11, pp. 975-983, November 2010.
- [3] M. Hayati, A. Khajavi, and H. Abdi, "A miniaturized microstrip dual-band bandpass filter using folded UIR for multimode WLANs," *Appl. Comp. Electro. Soc. (ACES) Journal*, vol. 28, no. 1, pp. 35-40, January 2013.
- [4] S. Lotfi, S. V. Makki, and S. Majidifar, "Design of microstrip low-pass filter with ultra-wide stopband and sharp rejection," *International Journal of Engineering & Technology Sciences (IJETS)*, vol. 2, no. 1, pp. 47-57, 2014.
- [5] S. V. Makki, A. Ahmadi, S. Majidifar, H. Sariri, and Z. Rahmani, "Sharp response microstrip LPF using folded stepped impedance open stubs," *Radioengineering Journal*, vol. 22, no. 1, pp. 328-332, 2013.
- [6] H. Sariri, Z. Rahmani, A. Lalbakhsh, and S. Majidifar, "Compact LPF using T-shaped resonator," *Frquenz Journal*, vol. 67, no. (1-2), pp. 17-20, 2013.
- [7] M. Hayati, S. Majidifar, and O. S. Fathabadi, "Compact microstrip lowpass filter with wide stopband and high attenuation," *Microwave Journal*, April 2012.
- [8] "Revision of part 15 of the commission's rules regarding ultra-wideband transmission systems," *First Note and Order Federal Communications Commission*, ET-docket 2002, pp. 98-153, 2002.
- [9] R. Li and L. Zhu, "Compact UWB bandpass filter using stub-loaded multiple-mode resonator," *IEEE Microw. Wireless Compon. Lett.*, vol. 17, no. 1, pp. 40-42, January 2007.
- [10] S. Sun, L. Zhu, and H. H. Tan, "A compact wideband bandpass filter using transversal resonator and asymmetrical interdigital coupled lines," *IEEE*

Microw. Wireless Compon. Lett., vol. 18, no. 3, 2008.

- [11] J. S. Hong and M. J. Lancaster, "Microstrip filters for RF/microwave applications," *New York: Wiley*, 200173-175, March 2008.
- [12] H. Shaman and J. S. Hong, "Ultra-wideband bandpass filter with embedded band notch structures," *IEEE Microw. Wireless Compon. Lett.*, vol. 17, no. 3, pp. 193-195, March 2007.
- [13] H. Shaman and J. S. Hong, "Input and output cross-coupled wideband bandpass filter," *IEEE Trans. Microw. Theory Tech.*, vol. 55, no. 12, pp. 2562-2568, December 2007.
- [14] P. Monda and M. K. Mandal, "Compact ultra-wideband bandpass filter with improved upper stopband," *IEEE Microw. Wireless Compon. Lett.*, vol. 17, no. 9, pp. 643-645, 2007.
- [15] P. Mondal, A. Roy, and S. K. Parui, "Wide-band bandpass filter using CRLH transmission line and floating slot approach," *2nd Int. Conf. Computer, Communication, Control and Information Technology*, vol. 4, pp. 466-471, 2012.
- [16] C. C. Chen, J. T. Kuo, M. Jiang, and A. Chin, "Study of parallel coupled-line microstrip filter in broadband," *Microw. Opt. Tech. Lett.*, vol. 48, no. 2, 373-375, February 2006.
- [17] R. Li and L. Zhu, "Compact UWB bandpass filter using stub-loaded multiple-mode resonator," *IEEE Microw. Wireless Compon. Lett.*, vol. 17, no. 1, 40-42, January 2007.
- [18] A. A. Lotfi-Neyestanak and A. Lalbakhsh, "Improved microstrip hairpin-line bandpass filters for spurious response suppression," *IEE Electron. Lett.*, vol. 48, no. 14, July 2012.
- [19] A. Lalbakhsh, A. A. Lotfi-Neyestanak, and M. N. Moghaddasi, "Microstrip hairpin bandpass filter using modified minkowski fractal shape for suppression of second harmonic," *IEICE Trans. Electron.*, vol. E95-C, no. 3, pp. 378-381, 2012.
- [20] J. Park, J. P. Kim, and S. Nam, "Design of a novel harmonic-suppressed microstrip low-pass filter," *IEEE Microw. Wireless Compon. Lett.*, vol. 17, pp. 424-426, 2007.
- [21] M. H. AlSharkawy, D. Abd El-Aziz, and E. G. Mahmoud, "A miniaturized lowpass/bandpass filter using double arrow head defected ground structure with centered etched ellipse," *Progress In Electromagnetics Research Letters*, vol. 24, pp. 99-107, 2011.



Arash Ahmadii received his B.Sc. and M.Sc. degrees in Electronics Engineering from Sharif University of Technology and Tarbiat Modares University, Tehran, Iran, in 1993 and 1997 respectively. He joined soon after to the Electrical Engineering Department of Razi University, Kermanshah, Iran as a faculty member. He received his Ph.D. degree in Electronics from the University of Southampton, United Kingdom in 2008. From 2008 to 2010, he was a Fellow Researcher with the University of Southampton. He is currently an Assistant Professor in the Electrical Engineering Department, Razi University. His current research interests include implementation of signal processing systems, electronic circuit design and optimization and bio-inspired computing.



Seyed Vahab Al-Din Makki was born in Kermanshah. He received his Ph.D. degree in Electrical Engineering-Waves from Khaje Nasir Toosi University in 2008. His current research interests include modern digital radio propagation systems, microwave devices and radio transmitters. He is with the Electrical Engineering Department of Razi University in Kermanshah and Islamic Azad University, Kermanshah Branch, since 2008.



Ali Lalbakhsh was born in Tehran, Iran in 1985. He received his B. Sc. and M. Sc. degrees in Communication Eng. in 2008 and 2011 from Islamic Azad University, Borujerd Branch, Borujerd, Iran and Islamic Azad University, Science and Research Branch, Tehran, Iran. Since 2010 he has been teaching in the Department of Electrical Engineering at Islamic Azad University, Kermanshah Branch, Kermanshah, Iran. His research interests include microstrip filter, microstrip antenna, RF circuit design and evolutionary algorithm. Lalbakhsh is a member of IEEE and the Institute of Electronics, Information and Communication Engineers (IEICE). He is also a Reviewer to The Applied Computational Electromagnetics Society (ACES).



Sohrab Majidifar received his B.Sc. and M.Sc. degrees in Electrical Engineering from Razi University of Kermanshah in 2009 and 2011 respectively. He joined Kermanshah University of Technology in 2011 as a Lecturer. His research interests include microwave passive circuits, chipless RFID and RFIC.

Design of a Broadband Microstrip-to-Microstrip Vertical Transition

Ziwen Tao, Jianpeng Wang, and Yan Dou

Ministerial Key Laboratory of JGMT

Nanjing University of Science and Technology, Nanjing 210094, China
taozw5901075@163.com, eejpwang@gmail.com, eleyandou@gmail.com

Abstract — A broadband microstrip-to-microstrip vertical transition is presented in this paper. The proposed transition consists of two quarter-wavelength microstrip stubs and a half-wavelength slotline Stepped Impedance Resonator (SIR) on the common ground plane. The low-impedance section of the microstrip stub is formed by three single arms connecting in parallel, while the high-impedance section of slotline SIR is formed by four single arms connecting in series. A sample transition is designed and measured. Experimental results indicate that over 143% bandwidth with better than 10 dB return loss and below 2 dB insertion loss can be achieved.

Index Terms — Microstrip transition, multilayer circuits, slotlines, Stepped Impedance Resonator (SIR).

I. INTRODUCTION

In high-density multilayer integrated circuits such as Monolithic Microwave-Integrated Circuits (MMIC's), microstrip-to-microstrip vertical transitions are essential. Typically there are three methods to achieve microstrip vertical transitions. The first method is based on a via hole or via hole array [1-2]. This type of transition exhibits a low-pass behavior. Thus, the performance of the via-hole transition will be reduced as the operating frequency increases. The second method is based on the slot/aperture-coupled structure. The slot/aperture-coupled transition is basically a band-pass circuit and is realized via electromagnetic coupling through the slot/aperture on the common ground. By using

wide aperture whose length is quarter-wavelength at the center frequency, a bandwidth (at 8 dB return loss) of 4-12 GHz is obtained in [3] and a bandwidth (at 12.5 dB return loss) of 3-11 GHz is achieved in [4]. In [5-6], the wideband microstrip vertical transitions are obtained by using slot, which is quarter-wavelength away from the open end of the microstrip stubs. Different slot shapes are investigated in [5] in order to enhance the bandwidth. In [6], a bandwidth (at 10 dB return loss) of 3.1-11.56 GHz is obtained by using a half-wavelength U-shaped slot on the common ground. The third method is based on cavity-coupled structure [7-8]. This kind of transition needs to construct a cavity in a thick common ground, which increases the complexity of the circuit processing.

As is known to all, how to improve the bandwidth of the microstrip-to-microstrip vertical transition is a key consideration for the designers. Therefore, the motivation of this paper is to design a microstrip-to-microstrip transition with enhanced bandwidth. The main innovation of this work is to propose a new microstrip vertical transition with two major low-impedance microstrip stubs and a slotline SIR on the common ground. With this new structure, a transition with good performance can be obtained. Furthermore, this new design scheme can realize more design flexibility, as the bandwidth and impedance-matching of the transition can be easily controlled by changing the length of the high-impedance section of the slotline SIR. Measured results show that the proposed transition provides a bandwidth of 2.3-

14 GHz with return loss better than 10 dB.

II. MICROSTRIP VERTICAL TRANSITION DESIGN

The layout of proposed transition is shown in Fig. 1, and the transition structure parameters are shown in Fig. 2. We can see that the transition mainly consists of two parts. The first part is the port and the quarter-wavelength microstrip stub that is composed of a short microstrip line and a low-impedance microstrip stub on the top/bottom layer. The structure of the quarter-wavelength microstrip stub is shown in Fig. 3. It should be mentioned that the low-impedance stub acted as the major part of the quarter-wavelength microstrip stub and is constructed by three single arms connecting in parallel. With this form in the resonator, we can avoid the propagation of microstrip higher order modes and can reduce the radiation effects as analyzed in [10]. The second part is a half-wavelength slotline SIR on the common ground, which is at the middle layer of the structure. The high-impedance section of the slotline SIR is realized by four single arms connecting in series.

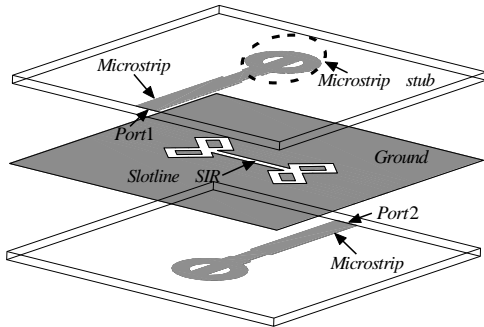


Fig. 1. Layout of the proposed microstrip-to-microstrip vertical transition.

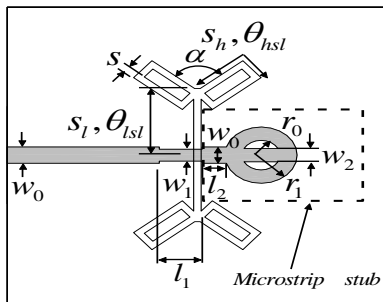


Fig. 2. Structure parameters of the proposed transition.

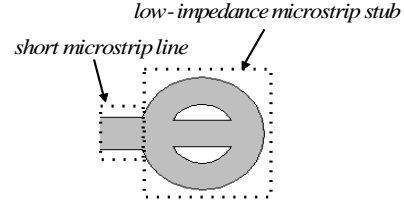


Fig. 3. Structure of the quarter-wavelength microstrip stub.

To illustrate the design theory of the proposed transition, the effect of the stubs impedance on bandwidth is primary analyzed. The equivalent circuit of presented transition is shown in Fig. 4, when the microstrip stubs and slotline stubs are uniform. The impedance looking into A-A' plane can be expressed as (assumed $\theta_{ms} = \theta_{sl} = \Phi$):

$$z_{in} = z_0 \frac{1 - j2 \frac{z_{ms}}{z_0} \cot \phi - 2 \frac{z_{ms}}{n^2 z_{sl}} \cot^2 \phi + j2 \frac{z_{ms}^2}{n^2 z_0 z_{sl}} \cot^3 \phi}{1 - j2 \frac{z_0}{n^2 z_{sl}} \cot \phi - 2 \frac{z_{ms}}{n^2 z_{sl}} \cot^2 \phi} \quad (1)$$

where n is slowly varying functions of frequency as described in [9], Z_{ms} is the characteristic impedance of microstrip stub, Z_{sl} is the characteristic impedance of slotline stub, and Φ is the electrical size of microstrip stub and slotline stub. If we set:

$$z_{ms} = \frac{z_0^2}{n^2 z_{sl}} \quad \text{and} \quad \frac{z_{ms}^2}{n^2 z_0 z_{sl}} \rightarrow 0, \quad (2)$$

equation (1) will be simplified as $Z_{in}=Z_0$. Replacing Z_{ms} by $Z_0^2/n^2 Z_{sl}$, the impedance Z_{in} becomes:

$$z_{in} = z_0 \frac{1 - j2 \frac{n^2 z_0}{z_{sl}} \cot \phi - 2 \frac{n^4 z_0^2}{z_{sl}^2} \cot^2 \phi + j2 \frac{n^6 z_0^3}{z_{sl}^3} \cot^3 \phi}{1 - j2 \frac{n^2 z_0}{z_{sl}} \cot \phi - 2 \frac{n^4 z_0^2}{z_{sl}^2} \cot^2 \phi} \quad (3)$$

That is to say, when Z_{ms} means a low impedance and Z_{sl} means a high impedance, a wide bandwidth can be obtained.

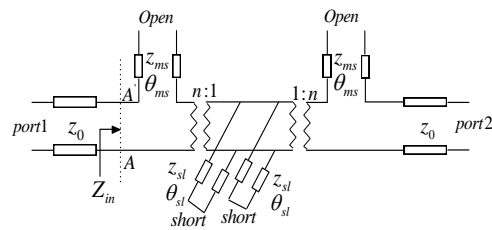


Fig. 4. Equivalent circuit of the presented transition with uniform microstrip and slotline stubs.

In order to realize broad bandwidth and good impedance-matching, here, the high-impedance slotline stubs are replaced by a slotline SIR. To illustrate this point, the performance of the proposed transition varies with the high-impedance section of the slotline SIR and is simulated and shown in Fig. 5, while the total length of the slotline SIR keeps half-wavelength. As can be seen from Fig. 5, a larger θ_{hsl} can achieve a wider transition bandwidth, yet degrade the impedance-matching performance. Thus, choosing suitable θ_{hsl} , both wide bandwidth and good impedance-matching can be realized. Moreover, the width W_1 is another important factor in the presented transition as it affects the coupling coefficients between the microstrip and the slotline SIR.

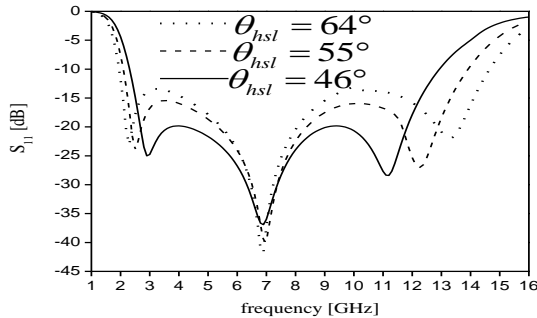


Fig. 5. S_{11} with different high-impedance slotline stub length θ_{hsl} .

III. SIMULATION AND MEASUREMENT RESULTS

Simulation was accomplished by using EM simulation software ANSOFT HFSS 12. Measurement was carried out on an Agilent 8722ES network analyzer. To verify the design, the proposed microstrip vertical transition is fabricated on the substrate with dielectric constant of 3.38 and a thickness of 0.508 mm. Figure 6 is the photograph of the proposed transition. The center frequency is designed at 8 GHz. The structure parameters are: $w_0=1.1$ mm, $w_1=0.8$ mm, $w_2=0.9$ mm, $l_1=1.5$ mm, $l_2=1.1$ mm, $r_0=1$ mm, $r_1=1.9$ mm, $S=0.3$ mm, $S_1=2.9$ mm, $S_h=4.5$ mm, and $\alpha=100^\circ$. Three microstrip arms are considered to have approximately the same length of 4.6 mm. The low-impedance microstrip stub is 20Ω with an electrical size of 72° . The total electrical size of the microstrip stub is approximately 89° . For the low-impedance

section of the slotline SIR, it has an impedance of 110Ω and an electrical size θ_{sl} of 35° , while the high-impedance section of the slotline SIR features with an impedance of 440Ω and an electrical size θ_{hsl} of 55° . The total electrical size of the slotline SIR is 180° . Notice that all these electrical parameters are estimated at 8 GHz.

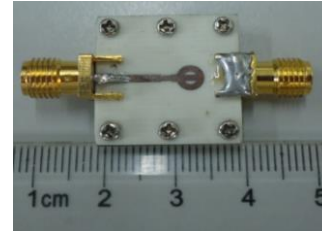


Fig. 6. Photograph of the proposed microstrip vertical transition.

Figure 7 shows the simulated and measured results of the proposed microstrip vertical transition. Measured results indicate that a broad transition bandwidth from 2.3 GHz to 14 GHz is achieved, referring to a criterion of better than 10 dB return loss. Inside the transition band, the maximum and minimum insertion losses are 2.0 dB and 0.3 dB, respectively, which ensures a good passband performance. There are some discrepancies between the simulated and measured results, which might be brought by the multiple reflections along the feed lines. The multiple reflections are due to the unexpected discontinuity effects between the SMA connectors and input/output terminals of the transition. For comparison, Table 1 summarizes the performance of some published microstrip-to-microstrip vertical transitions. It shows that the proposed transition has the property of wide bandwidth and good passband performance.

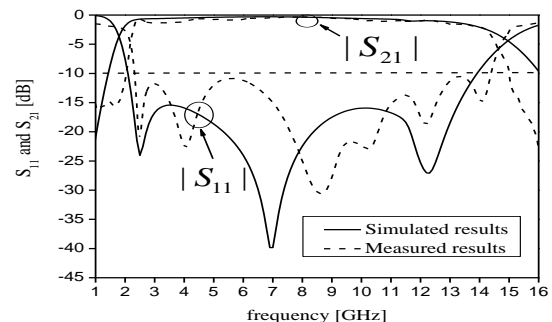


Fig. 7. Simulated and measured performance of the proposed transition.

Table 1: Performance comparisons among published microstrip-to-microstrip vertical transitions and proposed one

| Ref. | Return Loss | Bandwidth | Insertion Loss |
|-----------|-------------|----------------------|----------------|
| [3] | 8 dB | 4-12 GHz (100%) | ≤ 2.7 dB |
| [4] | 12.5 dB | 3-11 GHz (114%) | ≤ 1 dB |
| [6] | 10 dB | 3.1-11.56 GHz (115%) | ≤ 2 dB |
| [7] | 10 dB | 2.6-7.8 GHz (100%) | ≤ 1.5 dB |
| [8] | 10 dB | 18.3-22 GHz (18%) | ≤ 2.5 dB |
| This work | 10 dB | 2.3-14 GHz (143%) | ≤ 2 dB |

IV. CONCLUSION

A broadband microstrip-to-microstrip vertical transition is presented in this letter. One prototype of transition with center frequency at 8 GHz has been demonstrated. The demonstrator exhibits the properties of compact size and broad bandwidth. With all these good features, the proposed transition could be widely applied in high-density multilayer integrated circuits.

ACKNOWLEDGEMENT

This work was supported by the Nature Science Foundation of China under Grant No. 61101047, the Specialized Research Fund for the Doctoral Program by the Ministry of Education of China under Grant No. 20113219120015 and the Zijin Intelligent Program by the Nanjing University of Science and Technology.

REFERENCES

- [1] R. Valois, D. Baillargeat, S. Verdyme, M. Lahti, and T. Jaakola, "High performances of shielded LTCC vertical transitions from DC up to 50 GHz," *IEEE Trans. Microw. Theory Tech.*, vol. 53, no. 6, pp. 2026-2032, June 2005.
- [2] F. Casares-Miranda, C. Viereck, C. Camacho-Penãlosa, and C. Caloz, "Vertical microstrip transition for multilayer microwave circuits with decoupled passive and active layers," *IEEE Microw. Wireless Compon. Lett.*, vol. 16, no. 7, pp. 401-403, July 2006.
- [3] L. Zhu and K. Wu, "Ultra broadband vertical transition for multilayer integrated circuits," *IEEE Microw. Guided Wave Lett.*, vol. 9, no. 11, pp. 453-455, November 1999.
- [4] M. Abbosh, "Ultra wideband vertical microstrip-microstrip transition," *IET Microw. Antennas Propag.*, vol. 1, no. 5, pp. 968-972, October 2007.
- [5] C. Chen, M. Tsai, and G. Alexopoulos, "Optimization of aperture transitions for multi-port microstrip circuits," *IEEE Trans. Microw. Theory Tech.*, vol. 44, no. 12, pp. 2457-2465, December 1996.
- [6] X. B. Huang and K. L. Wu, "A broadband and vialess vertical microstrip-to-microstrip transition," *IEEE Trans. Microw. Theory Tech.*, vol. 60, no. 4, pp. 938-944, April 2012.
- [7] E. S. Li, J. Cheng, and C. Lai, "Designs for broadband microstrip vertical transitions using cavity couplers," *IEEE Trans. Microw. Theory Tech.*, vol. 54, no. 1, pp. 464-472, January 2006.
- [8] T. Swierczynski, D. McNamara, and M. Clenet, "Via-walled cavities as vertical transitions in multilayer millimeter-wave circuits," *IET Electron. Lett.*, vol. 39, no. 25, pp. 1829-1831, December 2003.
- [9] J. Chramiec, "Reactances of slotline short and open circuits on alumina substrate," *IEEE Trans. Microw. Theory Tech.*, vol. 37, no. 10, pp. 1638-1641, October 1989.
- [10] P. Soltysiak and J. Chramiec, "Design of broadband transitions from microstrip to slotline," *IET Electronics Letters*, vol. 30, no. 4, pp. 328-329, February 1994.



Ziwen Tao is currently working towards his Master's degree in Electromagnetic Field and Microwave Technology at NJUST. His research interest is the design of microwave and millimeter wave transition structure.



Jianpeng Wang received his M. Sc. and Ph. D. degrees from UESTC, Chengdu, China, in 2004 and 2007, respectively, both in Electronic Engineering. Since January 2008, he has been with the Ministerial Key Laboratory of JGMT, School of Electronic and Optical Engineering, NJUST, where he is currently an Associate Professor. His research interests include the high performance microwave/millimeter-wave passive components, circuits and systems realized on PCB, LTCC, etc.



Yan Dou received her B.S. degree in Electronics and Information Engineering from Anhui University, Hefei, China, in 2011. She is currently working towards her Master's degree in Electromagnetic Field and Microwave Technology at NJUST. Her research interest is the design of miniaturized high performance microwave passive device.

CPW-Fed Fractal Monopole Antenna for UWB Communication Applications

Y. Zehforoosh¹ and M. Naser-Moghadasi²

¹Department of Electrical Engineering
Islamic Azad University, Urmia Branch, Urmia-Iran
y.zehforoosh@srbiau.ac.ir

²Faculty of Engineering
Islamic Azad University, Science and Research Branch, Tehran-Iran
mn.moghaddasi@srbiau.ac.ir

Abstract — This paper presents the results of a novel fractal monopole antenna that exhibits Ultra-Wideband (UWB) performance. Higher order iteration of the fractal motif constituting the antenna was analyzed and its performance evaluated in order to optimize the antenna's characteristics. Compared to a typical circular monopole antenna, the proposed antenna generates reflection-coefficient resonances that significantly improve its impedance bandwidth by 160%. The antenna's measured performance conforms to the desired UWB specifications.

Index Terms — CPW-fed, fractal technology, small antenna, UWB.

I. INTRODUCTION

In recent years, many fractal geometries have been used to develop antennas by utilizing the attributes of fractal geometry to perturb the antenna's electromagnetic field [1,2]. Fractals are complex geometric designs that repeat themselves and can be described as 'self-similar' and independent of scale [3,4]. Ultra-wideband antenna designs are driven by two desires: i.e., to make an antenna for a given frequency band as small as possible and to make an antenna cover several bands [5-8]. Fractal antennas have performance parameters that repeat periodically with an arbitrary fineness dependent on the iteration depth. Although the finite iteration depth fractal antenna is not frequency independent, it

however can cover frequency bands close together.

Fractal geometries are usually generated by applying an infinite number of times an iterative algorithm, such as the Multiple Reduction Copy Machine (MRCM) algorithm [9]. This iterative procedure involves using an initial structure called generator, which is replicated many times at different scales, positions and directions to construct the final fractal shape. The properties exhibited by fractals make them ideal to miniaturize wideband antennas with characteristics very similar to their larger counterparts [10-13]. In the case when the dimensions of an antenna are much smaller than the wavelength at its operating frequency, the efficiency of the antenna deteriorates drastically, since its radiation resistance decreases and the reactive energy stored in its near field increases [14]. However, fractal geometry provides an amazingly satisfying solution to this problem without undermining the antenna's characteristics. Hence, fractal geometries have become an inventive approach for designing miniaturized wideband and multiband antennas.

In this paper, we present a novel miniaturized CPW-fed fractal antenna that exhibits ultra-wideband performance. The proposed fractal monopole antenna is engendered in an iterative fashion, leading to self-similar structure. The antenna design operates across 2.10 to 19.04 GHz for $VSWR \leq 2$. Unlike other antennas reported in

the literature to date, the proposed antenna displays a good omni-directional radiation pattern, even at higher frequencies. The fractal monopole antenna was analyzed using Ansoft’s High Frequency Simulator (HFSS™). Simulated and measured results are presented to validate the usefulness of the proposed antenna’s structure for UWB applications.

II. FRACTAL ANTENNA STRUCTURE

Production of the proposed fractal monopole antenna involved replication of a geometric motif with some scaling and translation. Figure 1 shows the three steps required to create the fractal monopole antenna for UWB applications. The fractal antenna shown in Fig. 1 (c), is generated with an initial circular microstrip patch in Fig. 1 (a) of radius R_1 . An equilateral triangle is inscribed inside the circular patch, as shown in Fig. 1 (b). A second circle of diameter R_2 is inscribed inside this triangle so that it touches the sides of the equilateral triangle. The triangle is then subtracted from the outer and inner circular patches. This process is repeated and the third iteration uses a circle with diameter of R_3 . The upper segments of the circular patches are then subtracted to realize the required fractal geometry representing the radiating patch. Finally, the upper section of the ground-plane is truncated in a tapered shape, as shown in Fig. 1 (c), with the aim of reducing area of radiating patch.

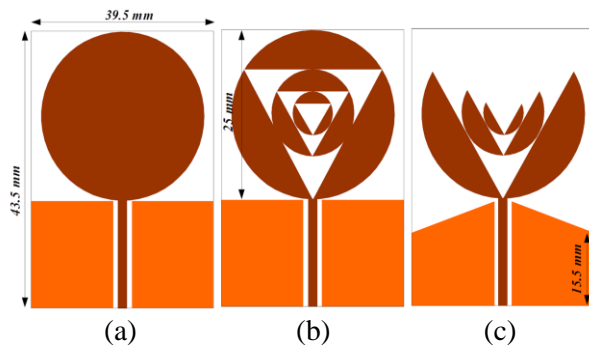


Fig. 1. Steps required to create the antenna structure.

The finalized microstrip monopole antenna design used a third order iteration fractal as an infinite iterative structure, it’s not practically possible because of fabrication constraints. The proposed antenna was constructed from FR4

substrate with thickness of 1.6 mm, relative dielectric constant of 4.4, and loss tangent $\tan\delta=0.02$. The width of the microstrip feed-line is fixed at 1.36 mm. The antenna’s dimensions are $28 \text{ mm} \times 35 \text{ mm}$.

III. ANTENNA PERFORMANCE

The proposed antenna’s characteristics were investigated by changing one of its parameters at a time, while keeping fixed all others to make the effect of that parameter clear in the plots. The fractal antenna’s performance was analyzed in order to determine its optimal parameters using HFSS™. The optimum magnitudes of the proposed antenna’s physical parameters defined in Fig. 2, are given in Table 1.

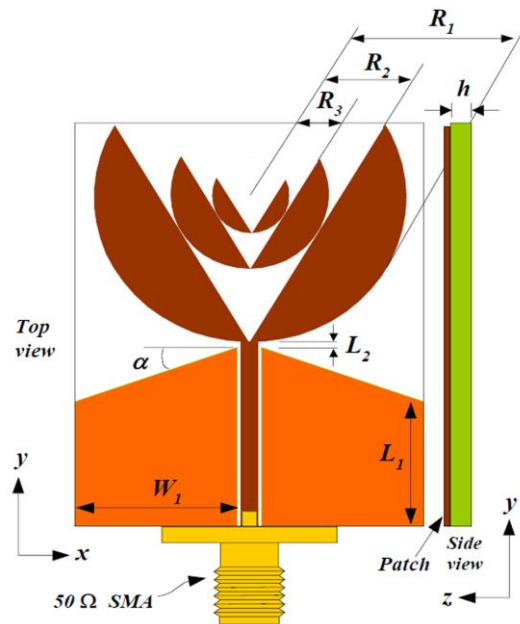


Fig. 2. The proposed antenna structure showing characterizing parameters.

Table 1: Dimensions (mm) of the proposed antenna

| R_1 | R_2 | R_3 | W_1 | L_1 | L_2 | α |
|-------|-------|-------|-------|-------|-------|-----------|
| 12.5 | 6.25 | 3.125 | 13.09 | 13.89 | 0.22 | 7° |

The effect of the iteration order on the fractal geometry constituting the proposed monopole antenna was studied. Reflection-coefficient characteristic for the first, second and third order iteration is presented in Fig. 3. It is observed that the impedance bandwidth of the antenna

effectively improves over the lower and upper frequency range as number of iterations increases. Although the overall effect on the reflection-coefficient is not significant, however, the order of iteration can affect the antenna's radiation efficiency as will be shown later.

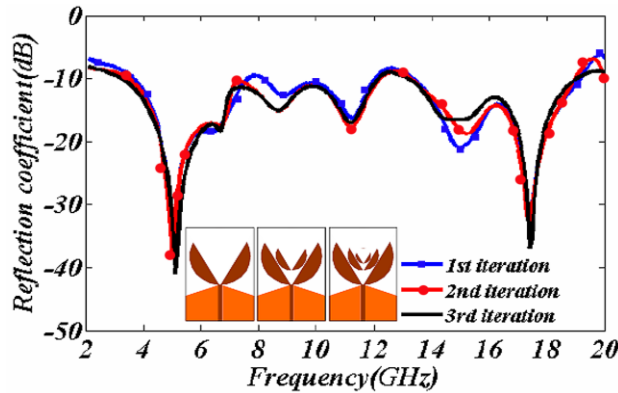


Fig. 3. Reflection-coefficient plot for the first three iterations of the antenna.

The effect of the ground-plane width (W_1) on the antenna's response is shown in Fig. 4, which shows very small changes in the parameter's dimensions and can significantly influence the antenna's reflection-coefficient. However, reflection-coefficient ≤ -10 dB is maintained over a very large bandwidth when it's optimized.

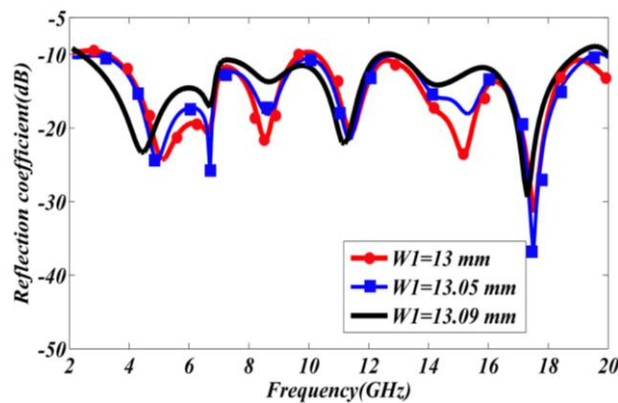


Fig. 4. Simulated reflection-coefficient plot for different values of W_1 .

It was also observed, small changes in the ground-plane length L_1 can affect the antenna's reflection-coefficient response, as shown in Fig. 5. Although L_1 can improve the reflection-coefficient, this is to the detriment of the

impedance bandwidth. Here, L_1 is optimized to realize a very large bandwidth extending between 2-20 GHz for reflection-coefficient ≤ -10 dB.

Figure 5 also shows the simulated reflection-coefficient characteristics for different values of L_2 . It shows small change in L_2 has a significant effect on the reflection-coefficient response as well as on the antenna's impedance matching. The value of L_2 of 0.22 mm provided the optimum response.

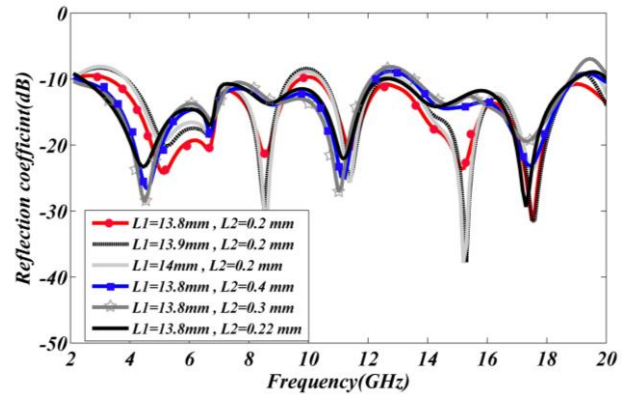


Fig. 5. Simulated reflection-coefficient plot for different values of L_1 and L_2 .

Another parameter that has an influence on the bandwidth of the antenna is the ground-plane truncation angle α , depicted in Fig. 6. The simulation results show increase in α cause the reflection-coefficient to change significantly, especially over the lower frequencies. Also, an increase in α can enhance the antenna's reflection-coefficient. It was found α of 7° to provide an optimum impedance bandwidth.

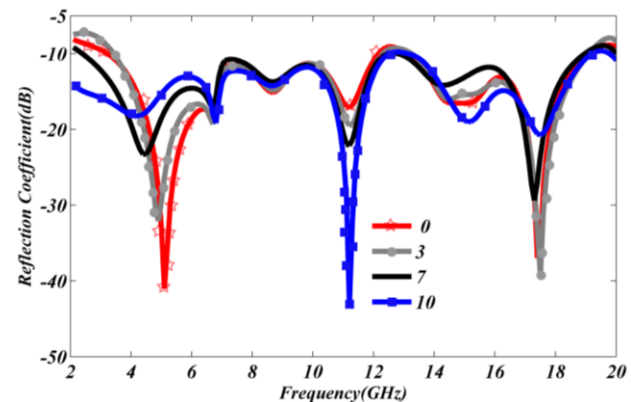


Fig. 6. Simulated reflection-coefficient plot for different values of α .

Comparison of reflection-coefficient characteristic for a typical circular monopole antenna and the proposed monopole fractal antenna is shown in Fig. 7. The circular monopole has the same diameter of 25 mm and feed-line dimensions as in Fig. 1 (a), and was constructed on the same dielectric substrate. The spectrum of the antenna shows numerous reflection-coefficient resonances corresponding to the various modes generated within the fractal structure. Shown in Fig. 7, is also the measured performance of the proposed antenna. The antenna's performance was measured in an anechoic chamber and its connector was enveloped in an RF absorbing material to provide a non-reflecting environment. The disparity between the simulated and measured responses of the proposed antenna is attributed to inaccurate simulation modeling and manufacturing tolerance and imperfect soldering effect of the SMA connector. The antenna's measured impedance bandwidth extends from 2.1 to 19.04 GHz, for which its reflection-coefficient characteristic is better than 10 dB. This performance exceeds the UWB as defined by FCC. The proposed antenna clearly exhibits a superior performance in terms of impedance bandwidth compared to the conventional circular monopole.

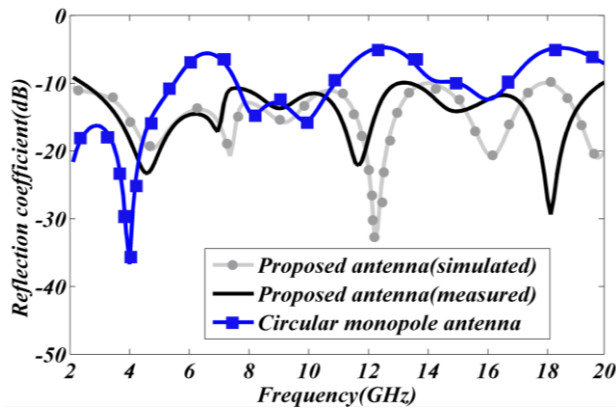


Fig. 7. Simulated and measured reflection-coefficient plot for a simple circular monopole and the proposed antenna.

Figure 8 shows the current distribution over the antenna at various spot frequencies. This indicates areas of the antenna that are critical at a given frequency. Knowledge of this can be used to modify the structure to optimize the characteristics

of the antenna. At 3 GHz, the intensity of the current is strongest across the entire feed-line and the area of the ground-plane immediately next to the feed-line. The current is also excited at the intersection of the feed-line and 1st iteration patch segments, as well as at the lower and upper ends of the 2nd and 3rd iteration segments. At 6 GHz, the current intensity is strongest at the middle and outer ends of the feed-line, intersection of the feed-line and 1st iteration patch segments, as well as middle and outer sections of the 1st iteration segments. Current is excited at the lower end of the 2nd iteration segments. At 8 GHz, the current distribution over the feed-line and fractals is similar to that at 6 GHz, but the intensity is moderately reduced. The current excited over the 2nd iteration segments has now moved to its upper end. At 10 GHz, current distribution over the fractal antenna is similar to that at 6 GHz; however, the distribution over the ground-plane close to the feed-line is much more intense and current is excited over the 1st iteration segments.

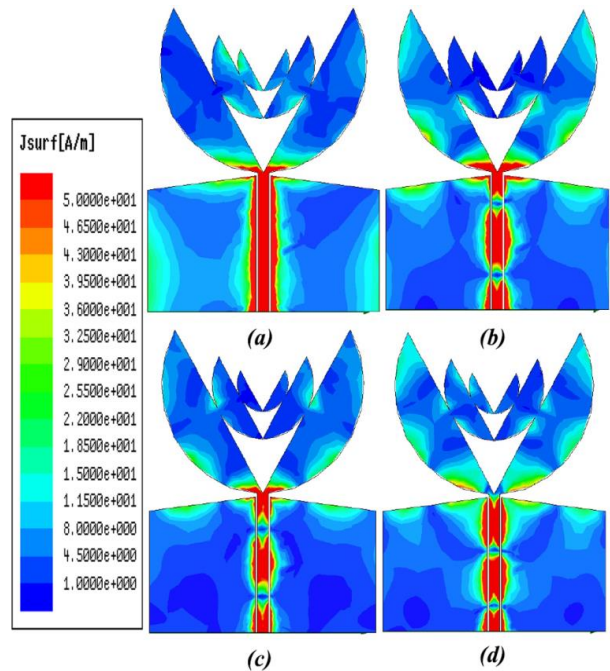


Fig. 8. Current distributions over the proposed antenna at: (a) 3 GHz, (b) 6 GHz, (c) 8 GHz, and (d) 10 GHz.

Figure 9 shows the measured radiation patterns of the fractal antenna, including the co-polarization and cross-polarization in the *H* and *E*-

planes. The radiation patterns were measured in an anechoic chamber. It can be seen that the radiation patterns plane are nearly omni-directional for the four frequencies; however, with varying field intensity.

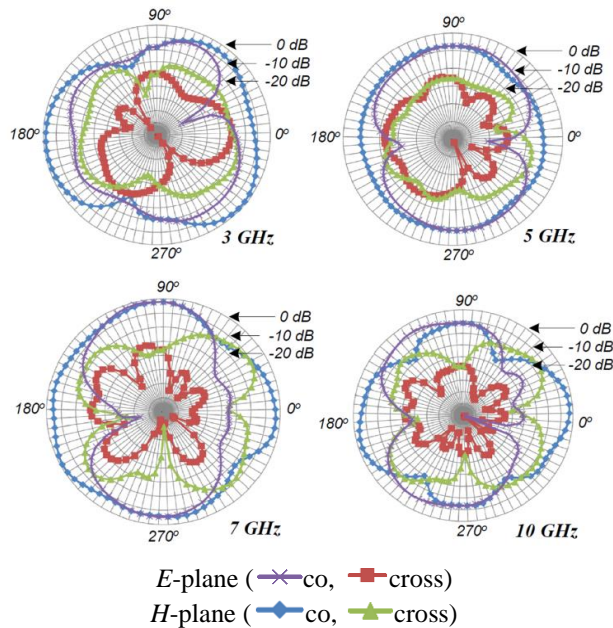


Fig. 9. Measured *E*-plane (*x*-*z*) and *H*-plane (*y*-*z*) radiation patterns of the proposed fractal antenna at various spot frequencies.

Gain versus frequency response for the three iterations of the antenna, as well as the efficiency of the optimized third order iteration, are shown in Fig. 10. The gain for the three iterations are approximately the same between 3-5 GHz; however, the gain of the fractal with a higher iteration order generally provides a higher gain between 6-8 GHz. Maximum gain of 4.9 dBi is obtained at around 9 GHz. The efficiency of the proposed antenna for iteration-3 increases with frequency and varies between approximately 74-92%. Reflection coefficient, gain, efficiency and radiation pattern are important parameters of UWB antennas. Other important parameters include system transfer function and group delay. Ideally, group delay in UWB applications should be constant over the entire bandwidth as well. To assess these parameters, two identical fractal antennas proposed here were mounted 60 cm from each other, which corresponds to approximately

six wavelengths at the lower frequency of the band of operation and in the antenna's far-field region. The group delay measurement is shown in Fig. 11. This varies between around ± 1 ns, but drops down to -2.8 ns at round 6.8 GHz as a result of the fractal structure.

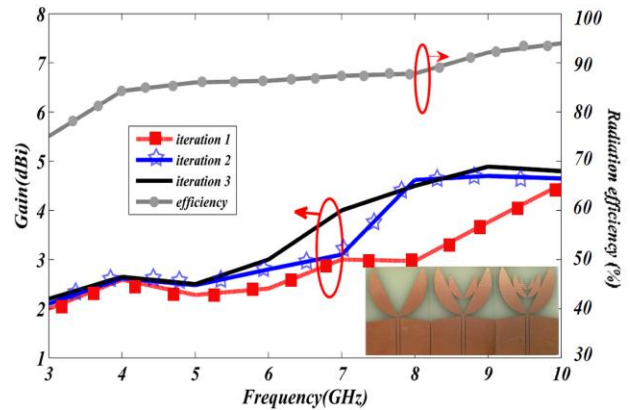


Fig. 10. Gain and efficiency plots for the three fractal iterations of the proposed antenna.

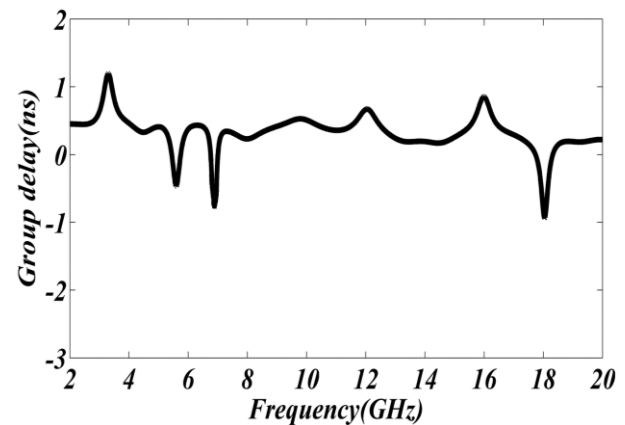


Fig. 11. Group delay plot of the antenna.

Various fractal configurations have been used for monopole antenna designs which include a combination of Giuseppe Peano and Sierpinski Carpet [11], and Pythagorean Tree [12] fractal geometries. Table 2 presents a summary comparing the proposed fractal antenna with fractal antennas in references [11] and [12]. It is observed that the proposed antenna has more resonances, a wider impedance bandwidth, higher gain performance and is less complex than antennas in [11] and [12].

Table 2: Isalient characteristics of the proposed antenna compared with references [7,8]

| | f_n (GHz) | S_{11} (dB) | f_c (GHz) | Peak Gain (dBi) | BW (for VSWR=2) | UWB Coverage | Structure Complexity | Size (mm ²) |
|--|----------------|--------------------|----------------|-----------------------|--------------------|-----------------|-------------------------|----------------------------|
| Proposed antenna, 1 st iteration ($\alpha=0^\circ$) | 5, 9, 11, 17 | -33, -12, -14, -33 | 11.60 | 4.7 | 4.2-19.0 GHz, 127% | No | Low | 28×35 |
| Proposed antenna 2 nd iteration ($\alpha=0^\circ$) | 5, 8, 11, 17 | -35, -13, -15, -33 | 11.55 | 4.8 | 4.1-19.0 GHz, 129% | No | Low | 28×35 |
| Proposed antenna 3 rd iteration ($\alpha=7^\circ$) | 4, 6, 11, 17 | -24, -15, -20, -30 | 10.57 | 4.9 | 2.1-19.0 GHz, 160% | Yes | Low | 28×35 |
| Combination of Giusepe Peano and Sierpinski Carpet Fractals [11] | 2, 11 | -16, -19 | 7.00 | 4.5 | 1-13 GHz, 171% | Yes | High | 20×25 |
| Pythagorean Tree Fractal [12] | 4.1, 7.2, 8.3 | -26, -22, -34 | 6.89 | 1.9 | 2.6-11.1 GHz, 123% | Yes | Very high | 25×25 |

VI. CONCLUSION

A miniature CPW-fed monopole antenna was presented, that was developed using a novel fractal geometry that is shown to exhibit ultra-wideband performance. It is shown that the bandwidth and gain of the antenna improves with increase in iteration order of the fractal geometry. The measured results show that the impedance bandwidth of the proposed antenna can be enhanced by truncating the ground-plane that is adjacent to the radiating patch. The measured results also confirm the antenna provides good radiation patterns that satisfy the requirements for UWB communication applications.

REFERENCES

- [1] D. H. Werner and S. Ganguly, "An overview of fractal antenna engineering research," *IEEE Trans. Antennas Propag.*, vol. 45, no. 1, pp. 38-57, 2003.
- [2] D. H. Werner and R. Mittra, "Frontier of electromagnetic," *Wiley-IEEE Press*, New York, 1999.
- [3] A. J. Crilly, R. A. Earnshaw, and H. Jones, "Fractals and chaos," *Eds. New York: Springer-Verlag*, 1990.
- [4] B. B. Mandelbort, "The fractal geometry of nature," *San Francisco, CA: Freeman*, 1983.
- [5] N. Ojaroudi, M. Ojaroudi, and S. Amiri, "Enhanced bandwidth of small square monopole antenna by using inverted u-shaped slot and conductor-backed plane," *Applied Computational Electromagnetics Society (ACES) Journal*, vol. 27, no. 8, pp. 685-690, August 2012.
- [6] N. Ojaroudi, M. Ojaroudi, N. Ghadimi, and M. Mehranpour, "UWB square monopole antenna with omni-directional radiation patterns for use in circular cylindrical microwave imaging systems," *Applied Computational Electromagnetics Society (ACES) Journal*, vol. 28, no. 2, pp. 123-129, February 2013.
- [7] A. Jafarholi and A. Jafarholi, "Compact broadband printed monopole antenna," *Applied Computational Electromagnetics Society (ACES) Journal*, vol. 28, no. 2, pp. 321-326, April 2013.
- [8] W. C. Weng, "Optimal design of an ultra-wideband antenna with the irregular shape on radiator using particle swarm optimization," *Applied Computational Electromagnetics Society (ACES) Journal*, vol. 27, no. 5, pp. 427-434, May 2012.
- [9] H. O. Peitgen, et al., "Chaos and fractals," *New York: Springer-Verlag*, 1990.
- [10] M. Ding, R. Jin, J. Geng, and Q. Wu, "Design of a CPW-fed ultra-wideband fractal antenna," *Micro. Opt. Technol. Lett.*, 49, pp. 173-178, 2007.
- [11] H. Oraizi and S. Hedayati, "Miniaturized UWB monopole microstrip antenna design by the combination of giusepe peano and sierpinski carpet fractals," *Antennas and Wireless Propagation Letters, IEEE*, vol. 10, pp. 67-70, 2011.
- [12] J. Pourahmadazar, C. Ghobadi, and J. Nourinia, "Novel modified pythagorean tree fractal

monopole antennas for UWB applications,” *Antennas and Wireless Propagation Letters, IEEE*, vol. 10, pp. 484-487, 2011.

- [13] A. Azari, “A new ultra-wideband fractal monopole antenna,” *Applied Computational Electromagnetics Society (ACES) Journal*, vol. 26, no. 4, pp. 348-352, April 2011.
- [14] D. H. Werner and R. Mittra, “Frontier in electromagnetic,” *Piscataway, NJ: IEEE Press*, pp. 48-81, 2000.



Y. Zehforoosh was born in Urmia, Iran in 1981. He received his Ph.D. degree from Urmia Islamic Azad University in 2012 in Telecommunication Engineering Fields and Waves. Also, he is a Faculty Member of the Electrical Engineering Department of Urmia Branch of Islamic Azad University, Urmia, Iran, since 2009, where he currently is Head of the Technical College and also member of Central Research Council. His research interests include broadband antennas, electromagnetic structures and UWB systems.



Mohammad Naser-Moghadasi was born in Saveh, Iran, in 1959. He received his B.Sc. degree in Communication Eng. in 1985 from the Leeds Metropolitan University (formerly Leeds Polytechnic), UK. Between 1985 and 1987 he worked as an RF Design Engineer for the Gigatech Company in Newcastle Upon Tyne, UK. From 1987 to 1989, he was awarded a full scholarship by the Leeds Educational Authority to pursue an M.Phil., studying in CAD of Microwave Circuits. He received his Ph.D. degree in 1993, from the University of Bradford, UK. He was offered then a two year Post Doc. to pursue research on Microwave Cooking of Materials at the University of Nottingham, UK. From 1995, Naser-Moghadasi joined Islamic Azad University, Science and Research Branch, Iran, where he currently is Head of Postgraduate Studies. His main areas of interest in research are microstrip antenna, microwave passive and active circuits and RF MEMS. Naser-Moghadasi is a member of the Institution of Engineering and Technology, MIET and the Institute of Electronics, Information and Communication Engineers (IEICE). He has so far published over 150 papers in different journals and conferences.